Adsorption and imbibition of binary liquids in nanoporous solids

Sujeet Dutta

ANNÉE 2016

UNIVERSITÉ DE RENNES 1

UNIVERSITE BRETAGNE LOIRE

THÈSE / UNIVERSITÉ DE RENNES 1
sous le sceau de l'Université Bretagne Loire

pour le grade de

DOCTEUR DE L'UNIVERSITÉ DE RENNES 1

Mention : Physique

Ecole doctorale (Sciences de la Matière)

Sujeet DUTTA

Préparée à l'unité de recherche UMR 6251, IPR
Institut de Physique de Rennes
UFR Sciences et Propriété de la Matière

Adsorption and imbibition of binary liquids in nanoporous solids

Thèse rapportée par : Sujeet Dutta

Benoit COASNE
Chercheur, CNRS, Laboratoire Interdisciplinaire de Physique / *rapporteur*

Jean LE BIDEAU
Professeur, Université de Nantes / *rapporteur*

et soutenue à Rennes le 2 Decembre 2016

devant le jury composé de :

Benoit COASNE
Chercheur, CNRS, Laboratoire Interdisciplinaire de Physique / *rapporteur*

Jean LE BIDEAU
Professeur, Université de Nantes / *rapporteur*

Patrick HUBER
Principal investigator, Technische Universität Hamburg-Harburg / *examinateur*

Denis MORINEAU
Directeur de recherche, CNRS, Université de Rennes 1 / *examinateur*

Ronan LEFORT
Maîtres des conférences, Université de Rennes 1 / *directeur de thèse*

Table of contents

1

Introduction

Heterogeneous systems consisting of liquid-gas, solid-gas, solid-liquid interfaces have been long studied and applied to vast array of technological use in areas such as petroleum refining[68], catalysis[71], water desalination[56], pharmaceuticals[6] and so on. Gradually the complexity of such systems kept increasing with the advent of materials engineered to provide greater surface area of activity and functionality. In the class of heterogeneous systems one of the best known are porous materials. Zeolites and metal-organic frameworks, which are often functionalized for achieving specific goals are widely used in chemical industry, and nowadays with a growing focus on environmental issues finding application in CO_2 storage and filtration[17,22,43] of industrial gases are good examples of the growth in scope of porous materials with ultra-high specific surface areas.

Nanoporous materials with pore diameters ranging from $2 - 50$nm, comparable to a few molecular layers are quite well known and studied widely. It has been demonstrated previously that confining liquid or gas molecules in such nanopores with specific geometries at the nanoscale could lead to great modification in physical properties of the confined molecules compared to their free bulk state. The pore architecture and competition between liquid-wall and liquid-liquid molecular interactions (Van der Waals, hydrogen-bonding, $\pi - \pi$ stacking etc) might induce ordering and phase separation or complete disorder. Confinement induced structuration have been shown to cause modification in crystallization and glass transition temperatures of the confined species[57]. Thus the notion of average physical properties such as density, viscosity or surface tension of bulk liquids needs to be applied with caution while dealing with nanoconfined systems.

Confinement induced structuration have been shown to cause modification in dynamic properties from the sub-nanometre length scale (conformational changes in molecular groups) to micrometre scale (translation self-diffusion)[38]. With the availability of ever advancing methods for characterization of soft-matter, confinement induced phenomena have been investigated quite thoroughly for single-component systems. The current scientific interest tends towards the study of multi-component systems with ever increasing complexity. While a lot of questions have been addressed well for systems showing a miscibility gap, much remains desired to understand the role played by competing liquid-liquid and liquid-wall interactions in the structure and dynamics of multi-component systems showing a negligible miscibility gap.

These questions extend to two kind of systems, one which are at thermodynamic equilibrium, dynamics of which characterized by molecular vibrations, rotations and translational self-diffusion and other which are out of equilibrium characterized by flow properties of confined materials through nanochannels, where the pore architecture and chemical environment might play a role in modifying the flow characteristics in confinement compared to bulk state. In the current chapter we discuss the various confinement induced phenomena occurring at nanoscale discovered so far and the scientific case of this thesis which attempts to answer some of the unanswered questions in this field.

I Confinement effects at equilibrium

A Structure and thermodynamics

A.1 Effect on melting point of pure liquids

The best known formalism describing the change in melting of a confined liquid from its bulk phase is given by the Gibbs-Thomson equation[61].

$$\Delta T_m = \frac{4\sigma_{SL} T_m}{d\Delta H_f \rho_s}$$

Where $\Delta T_m = T_{confined} - T_{bulk}$, the melting temperatures in confined and bulk phases respectively, σ_{SL} is the energy of interaction between confined liquid and pore-wall. T_m is the melting temperature of the bulk liquid, ΔH_f is the liquid's enthalpy of fusion and ρ_s is the solid density. d is the diameter of pore with which ΔT_m has an inverse proportionality dependence.

The above formalism have been demonstrated well for confined organic liquids in controlled pore glasses (CPG)[40] as shown in the figure 1.1 of ΔT_m versus $1/d$ values. This formalism has been quite successful in confined systems where the pore-diameter is greater than 20 times the Van der Waals diameter of the confined molecule[69] where the liquid-liquid intermolecular interactions reminiscent of bulk-like conditions dominate. However as we proceed to smaller pores deviation from Gibbs-Thompson formalism begins as the liquid-wall interactions begin to dominate modifying the crystallization characteristics significantly and leading to formation of amorphous glassy phases which shall be discussed in subsequent sections.

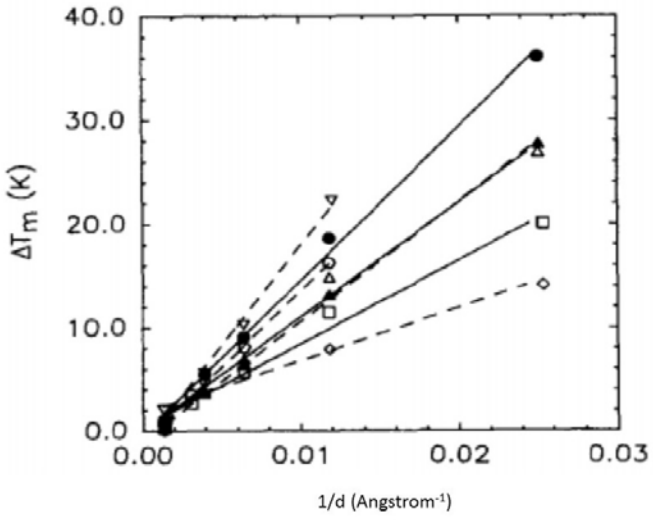

Figure 1.1: Variation of ΔT_m versus pore diameter for various organic liquids confined in controlled pore gasses.[40]

A.2 Effects on density

As we approach to pore sizes for confinement close to a few nano-metres, we are reaching a spatial dimension equivalent to a few molecular layers. The notion of average properties such as density or viscosity becomes less obvious at such scales unlike their free bulk state as it strongly depends on the structural characteristics of confined liquids which are controlled by the pore architecture and surface properties.

By a combination of vapour sorption and neutron scattering, the density of toluene confined in various porous silica matrices and its influence on the glass transition temperature obtained by complementary calorimetry experiments has been reported as shown in figure 1.2 and the result summarized in a table below the figure[9].

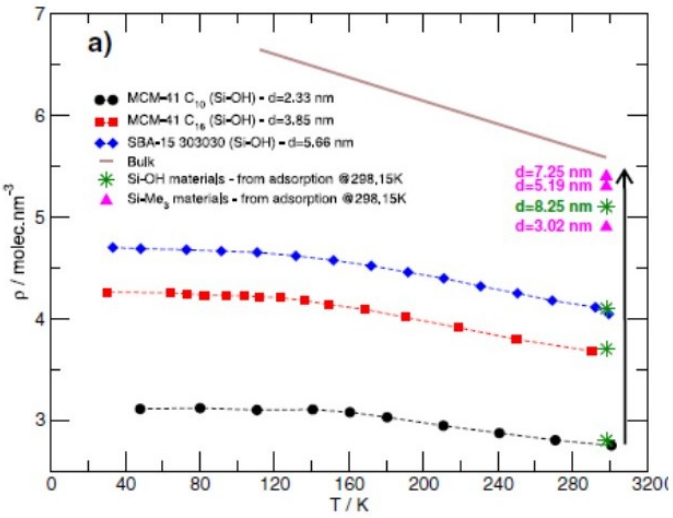

Glass transition temperature (T_g^*) and density at T_g^* (ρ_g^*) of toluene in bulk and in different confined materials.

Material	Surface	d_{IKS}/nm	A_{BET}/ $m^2 \cdot g^{-1}$	q_{10}/ nm^{-1}	T_g^*/K	ρ_g^*/ molec · nm^{-3}
Bulk	/	/	/	/	117	6.62
MCM-41 C_{10}	Si–OH	2.33	1017	2.02	145	3.09
MCM-41 C_{16}	Si–OH	3.85	1062	1.37	128	4.19
SBA-15 30-30-30	Si–OH	5.66	482	0.74	132	4.61

Figure 1.2: Relative density change of toluene in confinement with respect to bulk plotted against temperature, the point of deviation from monotonic density decrease indicates glass transition temperature. The values of density and glass transition temperature of toluene in different nanoporous silica matrices are listed in the table below[9]

We observe here a general trend of decrease in density with decreasing pore diameter, the results are most pronounced as we approach a pore size of $\approx 2\,\text{nm}$ which is basically equivalent to about two molecular layers of toluene. An increase in free volume due to greater steric hindrance might be attributed to the difficulty in packing molecules closer to each other and thus decrease in density. We find that with decreasing pore size goes hand-in-hand an increase in glass transition temperature which the authors have reported to be due to reduction in mean-square displacement of molecules with decreasing pore diameter.

B Effects on molecular dynamics

B.1 Glass-transition temperature

Depending on the rate of cooling and structural characteristics of a molecule, liquids may undergo crystallization or form a disordered system with exceptionally slow dynamics. This state known as a supercooled liquid is in a metastable state which finally reaches to an equilibrium state called glassy state. The relaxation time of glassy state far exceeds typical experimental observation times.

Unlike crystallization or melting which are first-order and represent a thermodynamic change, glass transition is a kinetic process and second-order changee. Figure 1.3 shows the difference between glass transition temperature or T_g and the crystallization temperature T_m and the effect of cooling rate on T_g[18].

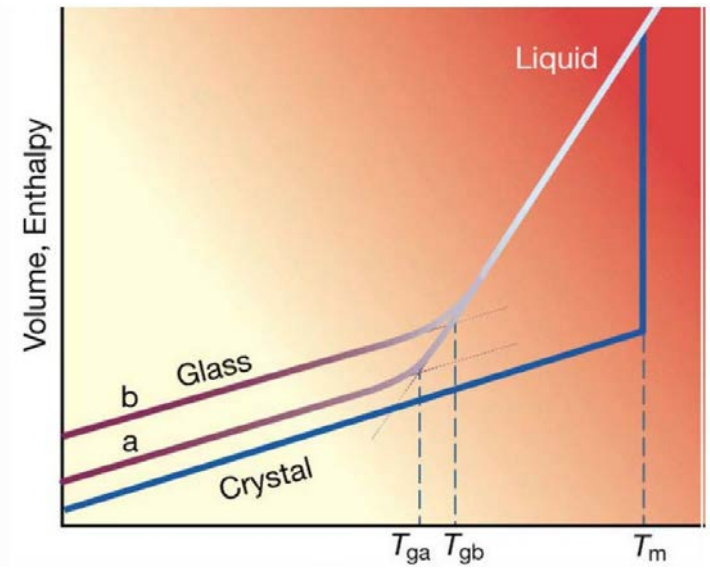

Figure 1.3: Comparison of crystallization and glass transition phenomena shown as change of volume enthalpy as a function of temperature. The effect of two different cooling rates (a and b) respectively and its influence on T_g.[18]

Based on their relaxation times, glass-forming liquids are characterized as "strong" liquids, exhibiting Arrhenius behaviour or "fragile" liquids which have an increased activation energy of α-relaxation time in the vicinity of glass transition showing deviations from Arrhenius behaviour. This degree of deviation from Arrhenius behaviour is known as "Angell's fragility" (f)[18], given by the following equation.

$$f = \frac{d(log\tau)}{d(T_g/T)}|_{T=T_g}$$

Where τ is the relaxation time. Figure 1.4 shows the fragility of different liquids based on Angell's model and classifies them into strong and fragile. We notice that organic liquids tend to be much more fragile, the category of interest in the nanoconfined systems to be discussed in this thesis.

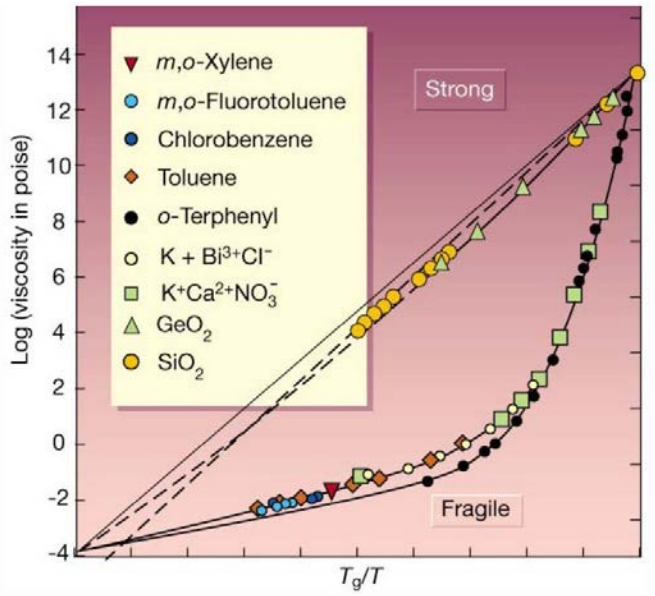

Figure 1.4: Fragility of various liquids expressed as log (viscosity) as a function of T_g/T[18]

One of the best known models to describe behaviour of liquids around T_g was given by the Adam-Gibbs model[5], according to which a liquid's relaxation time depends on its entropy of configuration such that the activation energy of transition (ΔE_A) is inversely proportional to the entropy of configuration (S_{config})[23].

$$\Delta E_A \propto \frac{1}{S_{config}}$$

According to the model, any molecular re-configuration which is typical in a transition, involves rearrangement of molecules belonging to a subsystem called "cooperatively rearranging region" (CRR), the dynamics of which are characterised by a distance known as cooperativity distance. Thus the glassy dynamics of a liquid can be influenced strongly by the finite sample size if it coincides with the cooperativity length, an occurrence not uncommon for liquids in nanoconfinement.

B.2 Finite size and surface effects

As we keep decreasing the volume of a glass-forming liquid such that its length scale becomes smaller than a typical cooperatively rearranging region, the activation energy of cooperative relaxation is supposed to decrease compared to the bulk state because the number of particles involved are lesser. The α-relaxation time τ_α is related to activation energy of cooperative relaxation as[23]

$$\frac{E_A(T)}{T} \propto \log\left[\frac{\tau_\alpha}{\tau_0}\right]$$

Thus τ_α relaxation time decreases with activation energy, indicating faster molecular dynamics as a consequence of finite size. The effects on glass-transition temperature have

been quite inconclusive so far and depending on the system, it might either increase, decrease or stay the same. Figure 1.5 (a) shows the trend of monotonic decrease in T_g[41] with decreasing pore-size in controlled pore glasses for two organic liquids while figure 1.5 (b) shows a non-monotonic change from decreasing to increasing for T_g of toluene confined in ordered silica nanopores MCM-41 and SBA-15[58].

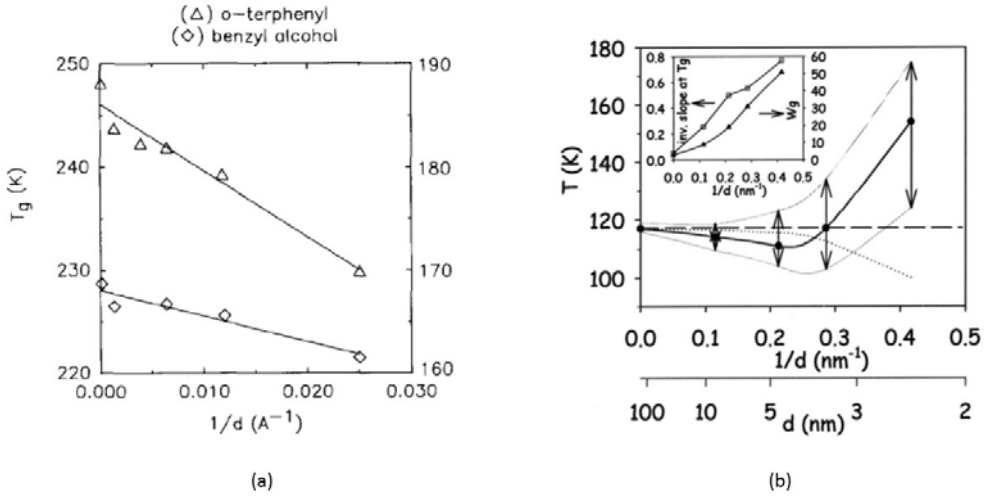

Figure 1.5: (a) Monotonic decrease in T_g of o-terphenyl and benzyl alcohol in controlled-pore glasses[41] (b) Non-monotonic change in T_g of toluene in MCM-41 and SBA-15 pores shown by the points. The arrows represent region of glass transition.[58]

The role played by surface topology on the glassy dynamics has been previously investigated with molecular dynamics simulations[65]. Surface roughness of confinement walls was found to induce greater relaxation than bulk state, while a smaller relaxation time was reported for smooth walls. In either case, relaxation dynamics approached closer to bulk-like behaviour as we go farther from confining walls and towards the centre.

The interplay of finite size and surface effects could thus play a strong role in governing the glass transition temperatures, the smaller are the pores, greater is the expected deviation from bulk glassy dynamics. However the positive or negative deviation shall depend on the surface roughness. Figure 1.5(a) and (b) are two opposite cases in this regard. The increase in T_g upon decreasing pore size in (b) indicates the existence of smooth pore walls for the mesoporous silica used to confine toluene, which in this case is known to be true for the material MCM-41, which has cylindrical, long and quite smooth pore walls. On the other hand, in the case of CPGs (a), we notice the opposite occurence, i.e. decrease in the T_g, which had been proposed to be as a result of the molecular structure of the confining liquids, which in this case due to their bulky nature might be harder to pack together, resulting into an increase in free volume of the confined liquid and eventually a depression in T_g.

B.3 Self-diffusion dynamics

Its not only the glassy dynamics of molecules which is affected by finite size effects but also the self-diffusion dynamics i.e. molecular motion concerning displacement of molecules from their positions. In figure 1.6 we see the decrease of diffusivity (translational diffusion coefficient) of cyclopentane under confinement in MCM-41 silica nanopores found by nuclear magnetic resonance measurements, compared to its bulk state, a gap which only broadens as the temperature approaches the melting point[7].

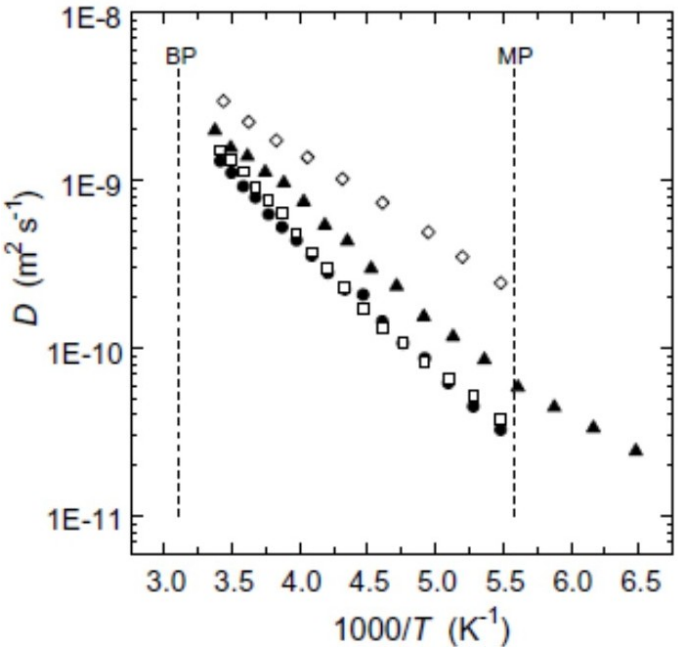

Figure 1.6: Comparison of diffusivity of bulk cyclopentane (hollow diamonds) and under confinement in MCM-41. Solid black circles represent complete filling, while triangles and squares represent partial filling[7].

The effect of nanoconfinement does not always necessarily lead to a slowing down of dynamics. Stray Field Gradient ^{15}N NMR diffusometry of pyridine confined in MCM-41 silica pores reveals that a fast exchange between pyridine molecules in the monolayer and in the core exceeds the diffusion coefficient of bulk pyridine[24]. Figure 1.7 shows the schematic representation of diffusion process.

C Confinement effect on binary liquids

We now move closer to the subject of this thesis, i.e. addressing the fundamental issues regarding effects of nanoconfinement on binary liquid mixtures. Two types of systems come into picture here, one where a partial miscibility gap between the mixture components exists and the other where no miscibility gap exists. Of the two, the former one has been better explored in previous works.

From a structural point of view triethylamine(TEA)/water binary liquid mixtures, which show a miscibility gap, were confined in 60 nm anodized aluminium oxide were

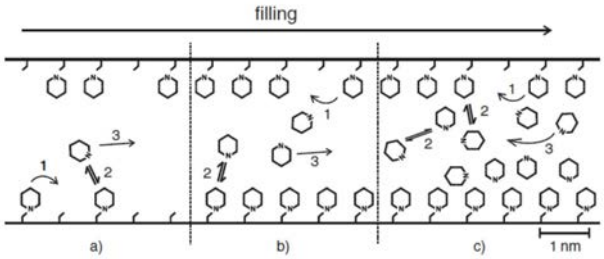

Figure 1.7: Pyridine confined in an MCM-41 pore. (a)-(c) showing increasing pore filling. (1) Surface diffusion (2) Adsorption and desorption (3) Isotropic diffusion, exchange between monolayer and core[24].

investigated using small angle neutron scattering[46]. The analysis of neutron scattering form factor showed presence of inhomogenities in the medium filling up the pores which was best explained by a model of phase separation of water and TEA into a core-shell structure, such that a few nanometres thick water layer or shell adsorbs on the pore-wall while TEA makes up the core. Figure 1.8 shows the best fits of neutron scattering form factor of TEA/water mixtures confined in AAO nanopores by the model of core-shell assembly as shown in the accompanying diagram.

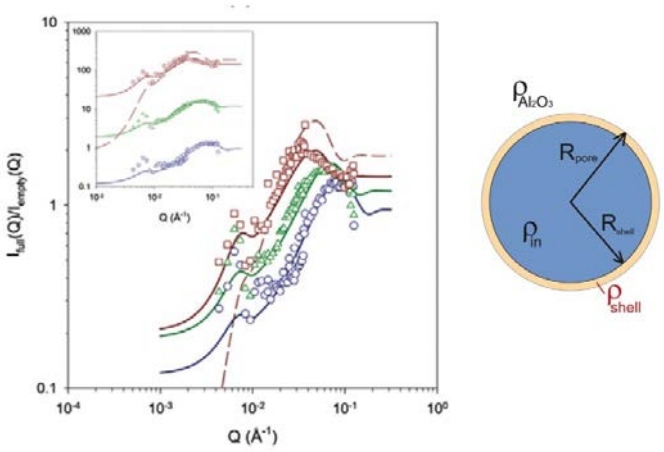

Figure 1.8: Neutron scattering form factor of TEA/D_2O mixture in AAO at three different temperatures shown by open circles. The solid lines show best fits based on a TEA-water core-shell structure while the dashed line shows fit based on model of water-TEA core-shell. On the right is a diagrammatic representation of core-shell assembly inside AAO nanopores.[46]

A system of water-isobutyric acid (iBA) has been shown to have different extent of miscibility based on the temperature and mixture composition[67]. ^{1}H pulsed field gradient NMR measurments on water-iBA mixtures confined in MCM-41 pores revealed a bi-exponential decay of magnetization as the system approached closer to 39 °C as shown in figure 1.9 (a), indicating the existence of two populations with different dynamics. The experimental observations were interpreted as evolution of the mixture from a completely

miscible system at low temperatures to a phase-separated one at higher temperature as shown in figure 1.9(b).

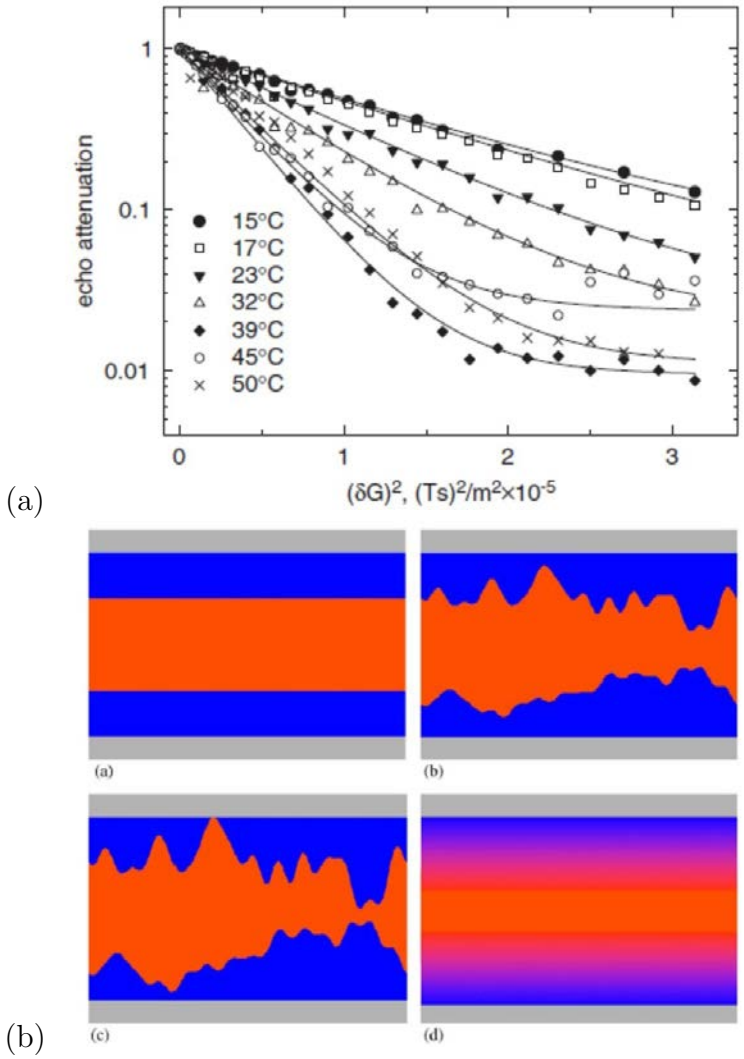

Figure 1.9: **(a)**Stimulated spin-echo attentuation from PFG NMR. From 39 °C and above the sigle component echo-attenuation is replaced by a two-component one.**(b)**Various phases of isobutyric acid-water mixture confined in controlled pore glass while transitioning from (a) liquid mixture of isobutyric acid and water at temperatures below 39 °C to (d) separation of components to a two-phase structure. Water along the pore wall, while isobutyric acid is in the centre.[67]

The available literature on confinement induced effects on binary liquids showing a low miscibility gap is relatively scarce when compared to the cases discussed above. Water-glycerol mixtures confined in MCM-41 pores of 2.1 nm diameter, i.e. roughly equivalent to width of two molecular layers have been investigated by differential scanning calorimetry (DSC) measurements[66]. DSC scans reveal that the glass transition temperature changed with changing water composition until roughly 20% by wt. of water in the solution, beyond which it barely changes with increasing water concentration as shown in figure

1.10, unlike the bulk mixtures where water has a plasticization effect that causes T_g to decrease with increasing concentration. The authors report the likelihood of a phase separation between water and glycerol, such that water owing to its greater ability of forming hydrogen-bonding interactions with the silica pore surface, preferentially adsorbs on the pore wall and the glass-transition of system under confinement is governed by glycerol in the core. At the same time, the broadening of T_g was explained by breaking down of glycerol-clusters.

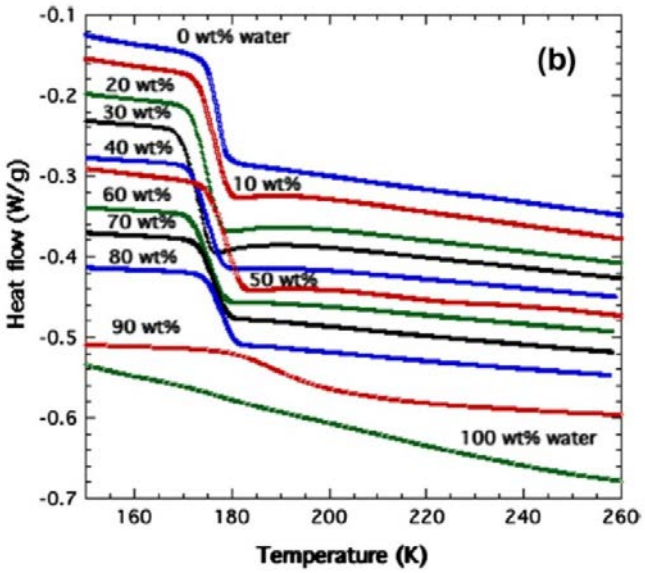

Figure 1.10: DSC scans of water-glycerol systems confined in MCM-41 nanopores of diameter 2.1 nm.[66]

We shall now discuss systems different that ones discussed so far in one aspect that, instead of being in a static thermodynamic equilibrium they are out of equilibrium.

II Confinement systems out of equilibrium

A Adsorption phenomena

Besides systems in static equilibrium which relate very well to nanoconfined liquids, equally interesting are the issues revolving around systems in dynamic equilibrium, by which in this section we particularly refer to adsorption phenomena. Gas molecules from an infinite reservoir occupy a given surface simply through physical interactions, such that at any give time there is an exchange of molecules between the gas phase and the adsorbed phase giving rise to a dynamic equilibrium as shown in figure 1.11[34].

As the relative pressure of the adsorbing gas or its chemical potential increases, greater number of molecules are adsorbed on the surface.

One of the most widely studied adsorption models is the Langmuir model developed by Irvin Langmuir in 1916 applied to adsorption of single monolayer[45]. This model was made for adsorption on a flat surface, assuming a certain fixed number of sites available for

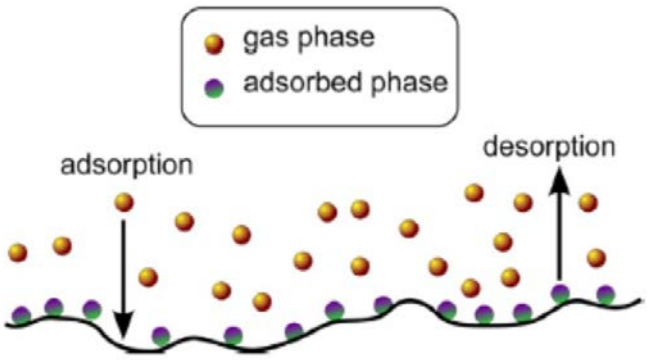

Figure 1.11: Schematic representation of the dynamic equilibrium process of adsorption.[34]

adsorption, each site capable of holding only one adsorbing particle/molecule and with no interactions between individual sites. From a statistical physics approach[21], the average number of particles adsorbed on the surface of a substrate by Langmuir model gives us

$$\langle N \rangle = \frac{N_0 \times x \times C}{1 + Cx}$$

Where N_0 is the number of sites available for adsorption $C = \exp \frac{\varepsilon}{K_B T}$ also known as the Langmuir constant, $x = P/P_0$ is the partial pressure of the adsorbing gas and ε is the energy per adsorbed particle. Useful theoretical contributions have been made in the understanding of single component as well as multi-component monolayer adsorption[48]. The use of an extended Langmuir isotherm has been reported to interpret binary gas mixture adsorption in graphitized carbon black STH-2. The extended Langmuir isotherm model assumes an ideal mixture with no interaction between adsorbed components[12]. The equation is written as:

$$\langle N_i \rangle = \frac{N_{0i} \times C_i \times y_i \times P}{1 + C_i y_i P + C_j (1 - y_i) P}$$

Where $\langle N_i \rangle$ is the number of particles adsorbed of the i^{th} component, N_{0i} is the total number of available sites for adsorption for component i, C_i and C_j are the Langmuir constants for the two components respectively, while P is the pressure of adsorbing gas mixture. In figure 1.12 (a) we see the fit of adsorption of simple gases in STH-2 by Langmuir adsortion isotherm, while in figure 1.12 (b) is presented the amount of CH_4 adsorbed in STH-2 in a $CH_4 - C_2H_6$ mixture[48].

The authors observe a deviation of the fit from experimental points and attribute it to be a consequence of nonideality of the adsorbed phase mixture, a deviation from one of the assumptions. Another important reason could possibly be the difference in value of N_{0i}, such that $N_{0i} \neq N_{0j}$ which leads to differing total adsorption capacities for the two components because of their unequal molecular diameters.

Most adsorption processes however are better described by the Brunauer, Emmett

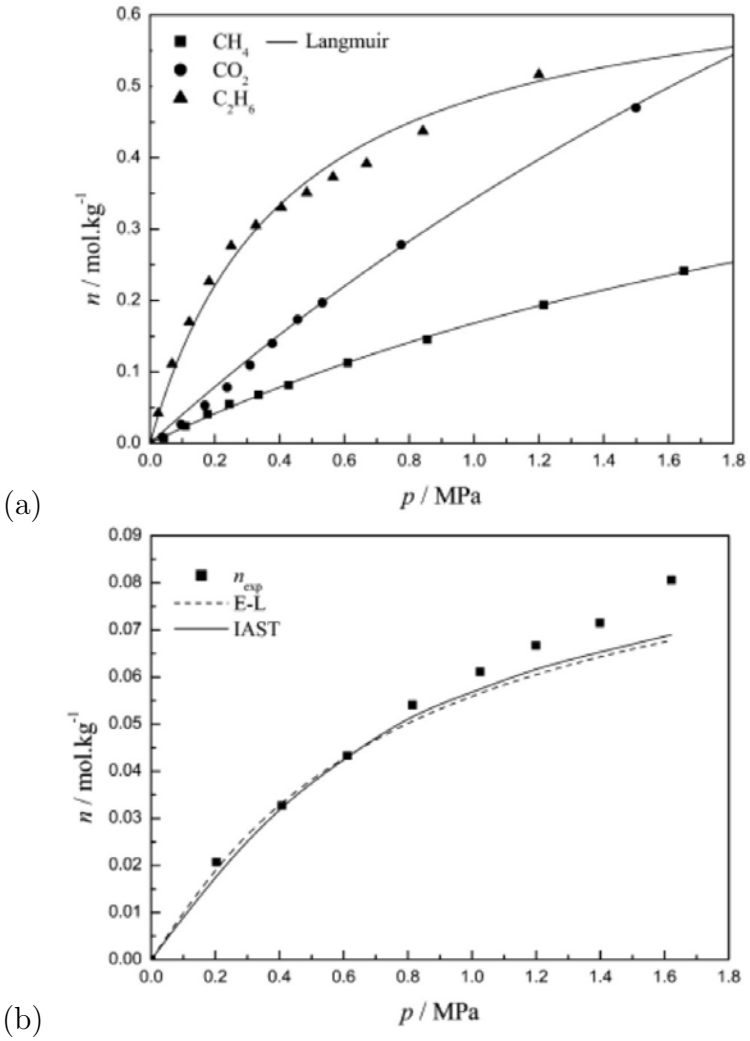

Figure 1.12: **(a)**Adsorption isotherms of methane, carbon-dioxide and ethane shown in symbols. Fit of isotherms by the Langmuir model of monolayer adsorption shown by solid line. **(b)** Amount of methane adsorbed (square points) in STH-2 in a binary gas adsorption of methane and ethane. Dashed line is the fit of experimental points using extended Langmuir model, while solid line is the fit of Ideal Adsorbed Solution Theory model.[48]

and Teller adsorption isotherm model, popularly known as the BET theory[14]. The BET theory has the same basic assumptions as the Langmuir model, except that adsorption is not confined anymore to the first monolayer and in fact consists of the presence of an adsorbed monolayer above which exists a liquid film of multiple molecular layers in equilibrium with the gas reservoir. The BET model is discussed more in detail in chapter 3. The average number of adsorbed particles on a substrate consisting of N_0 equivalent sites is given by:

$$\langle N \rangle = \frac{N_0 x C}{(1 + (C-1)x)(1-x)}$$

Where $C = \exp\left(\frac{\varepsilon_0 - \varepsilon_l}{KT}\right)$ is the BET constant and $x = P/P_0$ is the partial pressure of the adsorbing gas with respect to a reference pressure. ε_0 and ε_l are the energy particle of the one adsorbed directly on the surface and one constituting the liquid-film above it respectively.

Applicable only to low partial pressures where formation of first monolayers would take place for adsorption in porous materials, the BET theory is used widely to characterise porous materials, basically to obtain specific surface areas of such materials. Hill (1946) made one of the earliest approaches in understanding multimolecular adsorption by extending the BET theory to a multicomponent system, assuming adsorbed phase mixture to be ideal and the number of molecular layers which could form on a substrate to be finite instead of infinite as assumed in BET theory for single component system.

S. Amali et al.[8] utilized Hill's multimolecular adsorption model[35] in order to interpret the adsorption of toluene-water mixtures on a certain soil known as Yolo silt loam. Silt being porous in nature has the ability to adsorb gases such as toluene and increase soil toxicity.

Figure 1.13 shows the fit of multimolecular BET (MBET) adsorption model with experimental points showing the amount of volatile organic compound adsorbed in a VOC-water binary gas mixture[8]. The fraction of water is represented in terms of relative humidity (RH). Fits of the curves help obtain heat of adsorption of each component, weight of the monolayer adsorbed and the number of adsorbed layers, denoted here by n. We note here that the MBET model either underestimates or overestimates the quantity of VOC adsorbed with significant deviation at high relative vapour pressure of the VOCs. Thus the need for a better model to understand adsorption of multicomponent gas mixtures remains highly desirable to interpret such complex systems.

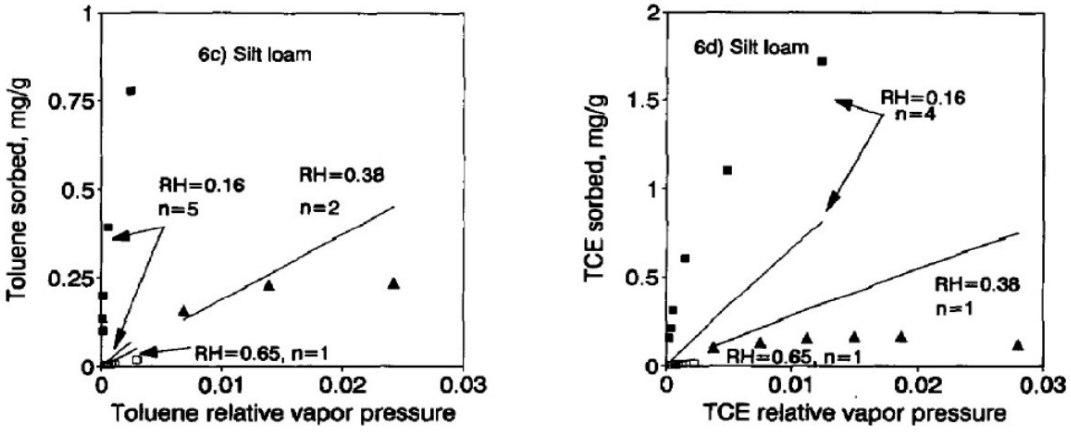

Figure 1.13: Amount of toluene and trichloro ethylene (TCE) adsorbed on silt loam in binary systems of toluene-water and TCE-water. Squares and triangles represent experimental points at different values of RH, solid lines are multimolecular BET (MBET) fits of experimental points. The value of n, number of adsorbed monolayers, is achieved from best fit of the experimental points.[8]

The competition between local (Van der Waals, hydrogen bonds) and long range (elec-

trostatic) interactions between adsorbed liquid phase molecules and host matrix could be tuned to achieve self organization and structuration at the nanoscale as shown in previous examples of binary liquids in confinement. This has raised considerable interest in the thermodynamics of phase separation under nanoconfinement.

M.W. Maddox et al. developed Grand Canonical Monte Carlo simulations to predict binary mixture adsorption of equimolar methane/nitrogen and methane/propane mixtures in bucky-tubes which are carbon nanotubes with pore width $\approx 5\,\mathrm{nm}$[53]. It was found that the component with stronger specific interaction with pore wall was preferentially adsorbed over the other which was qualitatively in agreement with the Ideal Adsorbed Solution Theory (IAST). Figure 1.14 is a plot of selectivity of propane in the adsorption of methane/propane adsorption in bucky tubes.

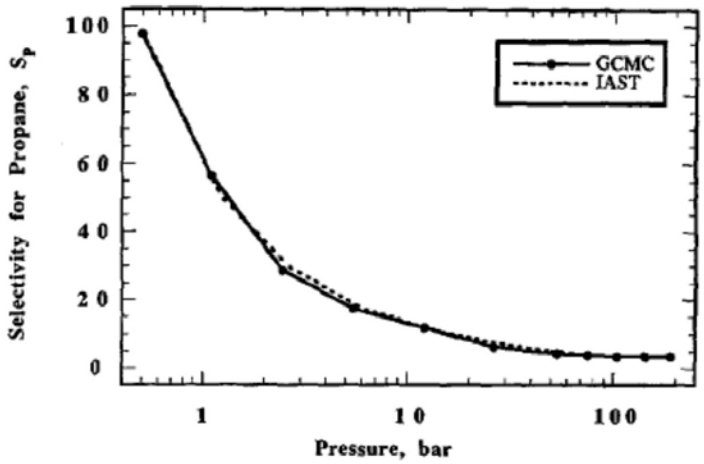

Figure 1.14: Selectivity of propane in propane/methane binary gas adsorption in double buckytube with pore size 4.8 nm. Propane adsorption is more selective at lower pressure.[53]

Jeong-Ho Yun et al. report a combination of experimental and theoretical approach to predict binary gas adsorption of alkane mixtures of methane and ethane in MCM-41 at different binary gas compositions[74]. IAST and GCMC could very well predict the adsorption isotherms. Figure 1.15 shows the adsorption isotherms of pure components and of mixture at various compositions.

We now proceed to discuss some of the developments made in the area of systems in confinement but completely out of thermodynamic equilibrium.

B Imbibition phenomena

The study of flow and transport phenomena through macroscopic channels has been well explained since decades. A transport of gas molecules through porous matrices is well explained by Knudsen diffusion. The capillary rise action of liquids in macroscopic capillaries is governed by a balance between capillary pressure (given by Young-Laplace equation? and hydrostatic pressure acting upon it given by[31].

$$\Delta p = \frac{2\sigma\cos\theta}{r} = \rho g h \tag{1.1}$$

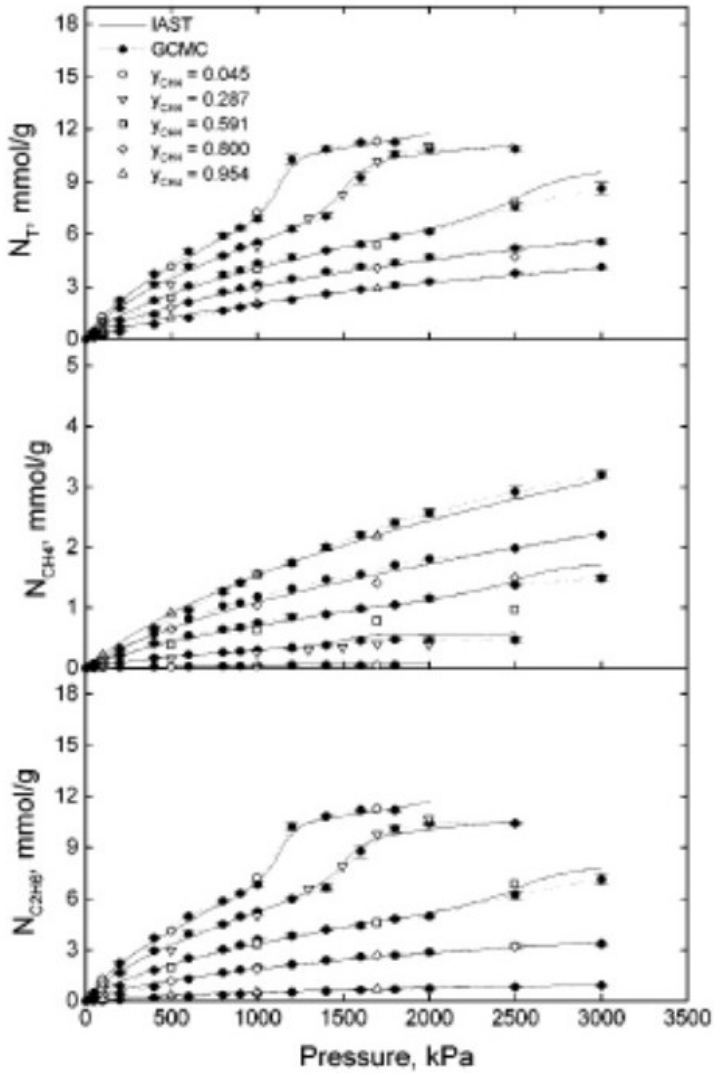

Figure 1.15: Adsorption of methane (CH_4) and ethane (C_2H_6) binary gas mixtures in MCM-41. The adsorption of pure components are denoted by N_{CH_4} and $N_{C_2H_6}$, while the mixture adsorption is denoted by N_T. Open symbols represent different mixture compositions while black dots and solid line represent calculated isotherm from GCMC and IAST theories respectively.[74]

Where Δp is the capillary pressure, σ is the surface tension of the liquid, r is the pore radius, ρ is the density of the liquid, $g = 9.8\,\mathrm{m/s^2}$ is the acceleration due to gravity and$h$ is the rise in liquid level inside the capillary.

The volumetric flow rate of a liquid through a porous material of thickness d and pressure difference Δp across its two ends is given by the Darcy equation[16] as follows:

$$\dot{V} = \frac{-\kappa A \Delta p}{\eta d} \tag{1.2}$$

Where $\kappa = \frac{\phi_0}{8\tau} r^2$ is a proportionality constant known as the hydraulic permeability of

the material[31]. ϕ_0 is the volume porosity of the matrix and τ is known as tortuosity of the pores.

Porous materials such as Vycor, a monolithic nanoporous silica, do not have straight cylindrical channel, instead there exists a network of meandering pores distributed isotropically. Tortuosity is a structural parameter of the matrix and is crudely defined as the ratio of total length of a curved path (l_C) to the distance between its two ends (l_E).

$$\tau = \frac{l_C}{l_E}$$

Obviously $\tau > 1$ and thus the volumetric flow rate is reduced to $\frac{\dot{V}}{\tau}$. Considering that a porous block filled up to a height h is equivalent to a fully filled block of thickness h, we can replace the thickness of porous block in equation 1.2 with the rise level of liquid given by the Young-Laplace equation (1.1) and inserting the result in equation 1.2 by the expression we have

$$\dot{V} = \Big(\frac{\phi_0}{8\tau} r^2\Big)\Big(\frac{2A\sigma\cos\theta}{\eta r h}\Big)$$

The volumetric flow rate can also be written in terms of the time dependent rise of liquid level as[?]

$$h(t) = \sqrt{\frac{\sigma\cos\theta}{2\phi_a\eta}}\, I\sqrt{t} \tag{1.3}$$

Such dependence of rise level on the square root of time is well understood for a century already[11,52,70]. However the most common reference to it is by the name of Lucas-Washburn law[20,72] and shall be called as such to keep in line with the usage in majority of available literature. Here we notice two new terms, ϕ_a or the apparent porosity accounting for the reduction in porosity caused by rapid adsorption of at least a monolayer of water adsorbed from atmospheric moisture in the form of humidity. Considering the highly hydrophilic nature of silica, this is a well-known occurring and has to be taken into account while interpreting experimental observations[37].

The term I is known as imbibition strength[31]. It depends only on the structural characteristics of the porous matrix and is given by:

$$I = \frac{r_h^2}{r}\sqrt{\frac{\phi_0}{r_L\tau}} \tag{1.4}$$

Where r_h and r_L are known as the hydrodynamic pore radius and Laplace radius respectively. r_h is associated to the stick and slip flow of liquids through pores[19] and is the radial distance from centre of pore to the point where velocity of liquid layers is equal to zero. r_L is the reduced radius of the pore due to formation of pre-adsorbed water layer(s) due to ambient humidity.

Given the cross-sectional area A of a porous block is constant, equation 4.2 could be re-written in terms of mass gain as a function of time.

$$m(t) = \rho A \sqrt{\frac{\phi_a \sigma \cos\theta}{2\eta}} I \sqrt{t} \tag{1.5}$$

Thus we find that both rise level and mass gain due to spontaneous imbibition of liquid into a porous block increases as a square root of time multiplied by a pre-factor.

$$h(t) = C_H \sqrt{t} \text{ and } m(t) = C_M \sqrt{t}$$

$$\text{Where } C_H = \sqrt{\frac{\sigma \cos\theta}{2\phi_a \eta}} I \text{ and } C_M = \rho A \sqrt{\frac{\phi_a \sigma \cos\theta}{2\eta}} I$$

Thus C_H and C_M give a measure of flow dynamics of liquids, their values being dependent on the physical properties of the liquids at a given temperature as well as the structural properties of the porous block.

As we approach the nanoscale $(2-50\text{nm})$, the size of capillaries are already just some molecular layers wide. Thus one may expect pore architecture and chemical environment to cause a modification in the flow properties from the above discussed Lucas-Wasburn flow dynamics applicable for macroscopic scale. However it has been well investigated in a number of different studies on imbibition of single-component liquids that the LC-dynamics hold true equally well even for flow through nanopores.

Simon Gruener et al. have thoroughly investigated the spontaneous imbibition of water and certain rod-like liquid crystal(namely 80CB) in Vycor with pore diameter of 7-8 nm[28]. Dynamics of capillary invasion were found to exhibit square root of time dependence given by the Lucas-Washburn law. Figure 1.16 shows the imbibition of water and two straight-chain alkanes into Vycor monitored by mass uptake of the liquids as a function of $\sqrt{t}$. The mass gain for all experiments increased proportionally to $\sqrt{t}$ and the proportionality constant, also known as imbibition coefficient could be simply calculated from m versus $\sqrt{t}$ curves. Although we would expect bulk liquid properties such as density, surface tension and viscosity to be subjected to finite size and surface effects under nanoconfinement, the flow properties could be easily predicted based on laws applied at the macroscopic scale.

However, very interesting phenomena have been reported for imbibition through nanopores which is unlikely to occur at the macroscopic scale. The rise level of water imbibition into a Vycor block was observed using visible light and neutron radiography and it was found that the imbibition front was broadened instead of being one sharp interface and that this broadening width itself was found to increase as a $\sqrt{t}$[29]. The explanation of such observation was provided using molecular dynamics simulations using a pore-network model[29,64]. At a junction of nano-capillaries of unequal diameters, the menisci rise further ahead in capillaries of smaller diameters due to greater Young-Laplace pressure. However the motion of advancing menisci is momentarily arrested when the hydrostatic pressure in the junction becomes greater than Young-Laplace pressure on those menisci. The motion of these arrested menisci resume when the liquid has moved by a certain distance in those capillaries which were still filling up. This distance moved follows the Lucas-Washburn dynamics and varies as a square root of time. Figure 1.17(a) shows the visible light images of front broadening for imbibition of water in Vycor. Figure 1.17[29] (b) shows a typical capillary junction where menisci arrest takes place[38].

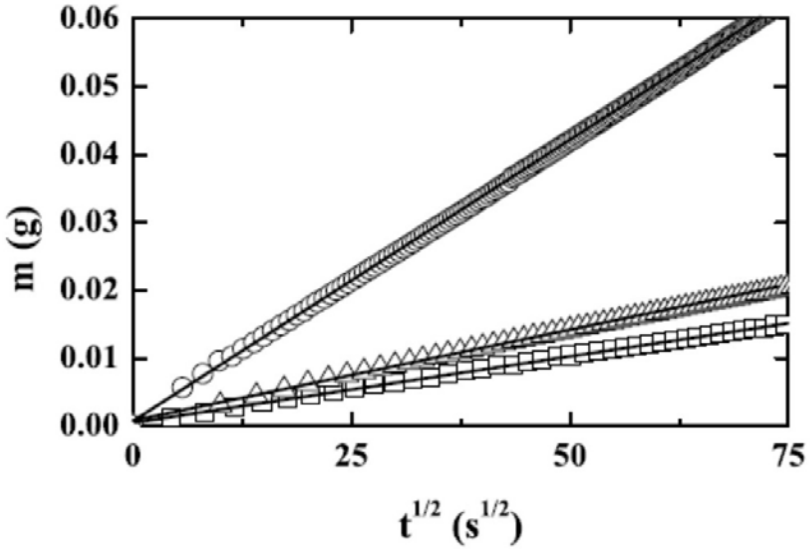

Figure 1.16: Mass uptake as a function of $\sqrt{t}$ for imbibition of water (circles), n-hexadecane (triangles) and n-tetracosane (squares)- Solid lines represent the Lucas-Washburn fits.[28]

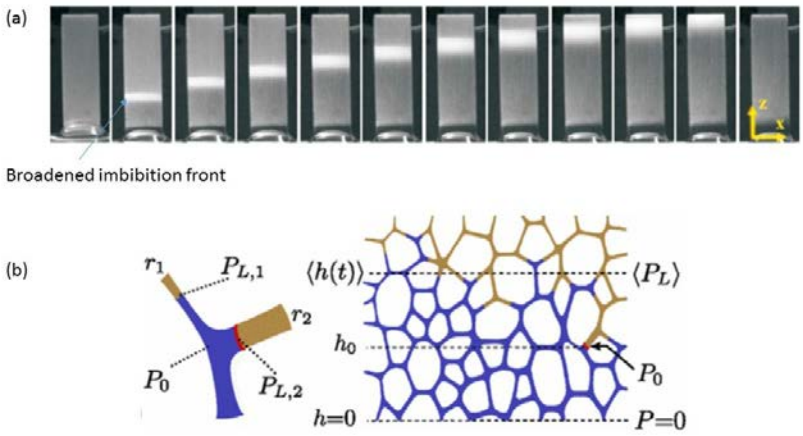

Figure 1.17: **(a)** Broadening of the imbibition front of water rising in Vycor block.[29] **(b)** Diagrammatic representation of a capillary junction showing the different distances moved by the different menisci.[38]

Although single-component imbibition systems have been investigated through various experimental and numerical simulation approaches, the available literature on imbibition of multi-component systems, especially ones showing a low gap of miscibility is still scarce and will one of the important aspects taken up in this thesis. We now proceed to describe more specifically the model system of nanoconfined binary liquids chosen in the work presented in this thesis to enrich our knowledge and understanding on confinement induced effects at the nanoscale.

III Thesis case

The experimental activities and their interpretation carried out in the framework of this thesis was with the objective to deepen our understanding of the confinement induced effects on structural and dynamic behaviour of a binary liquid mixture which shows no gap of miscibility at the macroscopic scale. The spatial area of confinement, its surface-topology of pores, the overall pore-architecture and chemical environment of pore walls (hydrophilic/hydrophobic) are essential criteria to which these binary liquids will be put through to understand their influence on the molecular organization and dynamics. This makes choice of an appropriate model system essential for both the binary liquids and host matrices.

A Choice of model system

A.1 Binary liquids without miscibility gap

Hydrocarbons make good examples of complex molecules, which depending on their chemical nature might be able to might be able to display capability of having more than one kind of molecular interaction (Van der Waals, hydrogen-bonding, $\pi - \pi$ interactions...). It is the interplay of these specific interactions between confined molecules and the host matrix which eventually should govern the structural and dynamic aspects of confined mixtures and therefore the choice of liquids for confinement are based on the multiplicity of intermolecular interactions displayed by the chosen components. Most importantly the binary liquid mixture must be completely miscible at macroscopic scale.

Keeping the above considerations in mind we choose our model system to be a binary liquid mixture of two hydrocarbons to be confined inside suitable nanoporous matrices. The first liquid is *tert*-butyl alcohol (C_4H_9OH), which by the virtue of its chemical structure consists of a polar hydroxyl group and nonpolar branched aliphatic chain giving it a hybrid character. The second liquid is toluene (C_7H_8), an aromatic compound, which is aprotic in nature. All throughout this Ph.D thesis *tert*-butyl alcohol will be referred by its acronym TBA while toluene will be referred by the acronym TOL.

B Porous materials

The second important aspect in choice of a model system is finding the appropriate host matrix. Fulfillment of the following criteria are quite essential for this purpose, a material which has thermal and chemical stability over the temperature range in which the liquids are aimed to be studied, the pore walls must be infinitely hard compared to the filled liquid or at least mechanically stable enough to withstand pore-filling without any deformation, be chemically nonreactive to the confined molecules, have a well-defined topology and finally the dimensions of confinement should provide a highly reduced spatial volume while at the same time not completely diminish the possibility of phenomena such as phase transitions, order-disorder, cooperative dynamics etc, characteristic of bulk-phase.

In the last century a diverse range of porous materials offering confinement in diameters less than 50 nm have been developed. Broadly we classify them as microporous materials,

having pore diameters less than 2 nm and mesoporous materials, those with pore diameters between 2-50 nm.

Amongst the most widely used microporous materials are zeolites, which are inorganic crystalline compounds, with a three-dimensional framework made up of silicon, aluminium, oxygen and metal ions, along with small molecules such as water in the structure, their general formula given as $M_{x/y}[(AlO_2)_x(SiO_2)_y].zH_2O$[51]. Where x and y are integers such that $y/x \geq 1$, M stands for the metal ion and n its valence while z are the number of water molecules. Zeolites have a very ordered structure and high specific surface area, combined high thermal and chemical stability, all of which could be tuned as per specific needs by modifying the basic composition. This makes them extremely useful today in the industry for catalysis, production of petrochemicals, energy storage and harvesting, detergents, agriculture and a foreseeable future in medical applications.

The second most important and more recent class of microporous materials are metal-organic frameworks (MOF). Unlike the purely inorganic nature of zeolites, MOFs are hybrid crystalline compounds made up of metal ions or their clusters linked via organic molecules (linkers) producing highly ordered crystalline structure in one, two or three dimensions[73]. MOFs lead zeolites in both, ability of tuning the structure and achieving tailor-made functional properties because of the wide range of metal ions and organic linkers available[15]. This can render MOFs with high surface selective properties, which in addition to large specific surface areas have lot of potential applications in future, ranging from catalysis, energy conversion to capture and separation of green-house gases and volatile organic compounds. However this flexibility comes as a price as the organic component of MOFs makes it prone to chemical instability and lacks the thermal and mechanical robustness of zeolites[36,59]. Nevertheless, improvements in the prevention of structural breakdown and increased thermal stability have gradually taking place.

We now move ahead to mesoporous materials, which have made their way into the chemical industry as well since couple of decades already and now find applications in ion exchange, water desalination, gas sensing and catalysis, with potential applications in fuel cells, photovoltaics and drug delivery. A major share of mesoporous materials are based on silicon and aluminium oxides. Beside them, porous silicon membranes, porous carbon and recently introduced polymer based mesoporous-materials are widely studied as well. The possibility to achieve high porous volume and specific surface area along with the diverse range of topologies that can be achieved makes these materials very interesting from the standpoint of understanding effect of pore architecture on local and long-range structural properties of confined liquids. Being inorganic in nature, silica and alumina are chemically very stable towards organic compounds

A great advantage of mesoporous materials when it comes to the study of structure and dynamics of molecules under confinement is the possibility to develop pore-architectures with highly-ordered geometry, uniform pore size, tunable chemical nature of pore walls, while at the same time achieve spatial dimensions conducive for examining the role played by the balanced of molecular interactions between host matrix and confined liquid on its physical properties, which makes them the preferred materials for confining TBA:TOL mixtures to study the effects of nanoconfinement.

Mesorporous materials,which shall be referred to as nanoporous materials in this thesis henceforth, for confinement of TBA and TOL were chosen on two grounds, firstly, for

structural and dynamic studies of TBA:TOL mixtures at thermodynamic equilibrium, for which the most suitable choices were MCM-41 nanoporous silica from the Mobil Composition of Matter series[44], Santa Barbara Amorphous-15 (SBA-15)[75] nanoporous silica and its carbon analogue CMK-3 from the Carbon Molecular Sieves series[63]. All three consist of highly ordered parallel cylindrical pores exhibiting strong two-dimensional periodic arrangement. Secondly, for studying dynamics of TBA:TOL mixtures at out-of-equilibrium conditions, i.e. under flow through nanochannels. The most suitable material for this purpose was Vycor® monolithic nanoporous silica because of its highly wettable surface and possibility of rendering it into specific geometric shapes and sizes[47].

In the subsequent sections we will discuss physical properties of TBA, TOL, their mixtures and morphological characteristics of MCM-41, SBA-15, CMK-3 and Vycor.

C Properties of bulk TBA:TOL mixtures

C.1 *tert*-butyl alcohol (TBA)

Tert-butyl alcohol or 2-methyl-propan-2-ol is one of the simplest alcohols that can undergo self-association in bulk liquid state to form micellar clusters. This clustering is possible by a combination of steric-hindrance provided by bulky *tert*-butyl and hydrogen-bonding interactions form the hydroxyl group such that the clusters are centred at the hydrophilic -OH groups while the hydrophobic *tert*-butyl groups are on the exterior. A number of studies have reported that these clusters can correlate with each other, giving rise to long range structural order, a signature of which is found in the pair correlation in the form of a prepeak of the static structure factor observed by neutron diffraction and simulations[1,25,32]. Figure 1.18 shows a diagrammatic representation of hydrogen-bonded cluster in TBA in the inset and its effect on the neutron diffraction patten of bulk TBA, seen as the appearance of a prepeak[1].

The Van der Waal's molecular diameter of TBA is $\approx 4.2\,\text{Å}$[26]. Its small size combined with the ability of molecular self-association has made TBA an interesting molecule to study confinement induced phenomena.However while using TBA one must exercise caution with temperature of working as it crystallizes into plastic phases below its melting point (25 °C) which necessitates it to be kept at temperature sufficiently high during experiment to prevent losing its liquid character.

C.2 Toluene (TOL)

Our second liquid of choice, toluene is an aromatic, aprotic and hydrophobic compound with a Van der Waals molecular diameter of $\approx 4.7\,\text{Å}$[26], which is equivalent to TBA. Unlike TBA, TOL is a glass forming liquid, which shows a strong non-Arhennian dependence of its viscosity with temperature. Its glass transition temperature is at $-160\,°\text{C}$ found by differential scanning calorimetry and neutron scattering measurements. Figure 1.19 shows the molecular structure of TOL along with that of TBA for comparison.

The intermolecular interactions amongst TOL molecules are largely dominated by Van

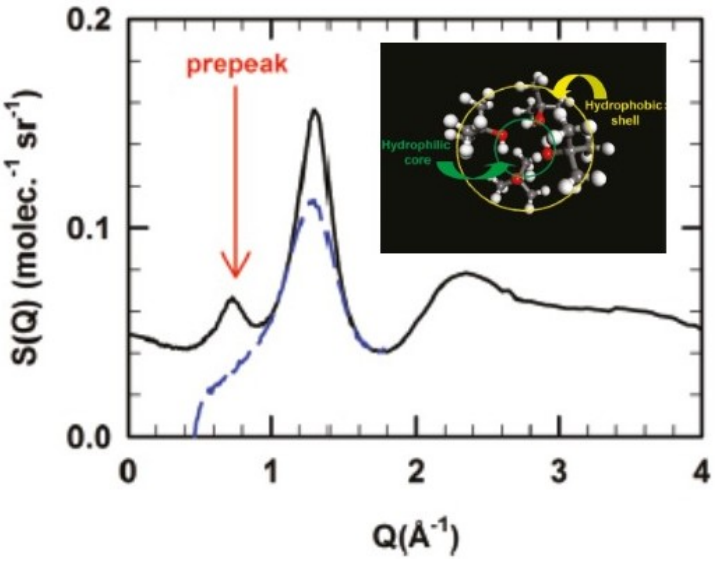

Figure 1.18: Static neutron diffraction spectrum of bulk TBA (solid black line) with the indication of prepeak. Inset: a diagrammatic view of TBA cluster[1]

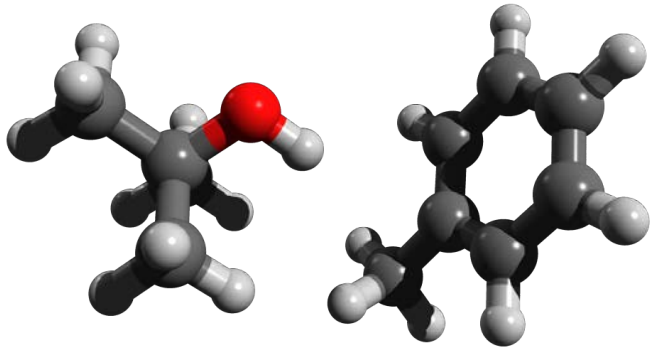

Figure 1.19: Molecular structures of TBA (left) and TOL (right). Grey balls indicate carbon atoms, white are for hydrogen while red is for oxygen.

der Waals interaction and $\pi - \pi$ stacking facilitated by the electron-rich aromatic ring. In a mixture, TOL and TBA interact mostly by Van der Waals interactions and to a minor extent by interaction of hydroxyl group with the quadrapole moment created by $\pi-$electron cloud of TOL's aromatic ring. The choice of TOL as a mixture component with TBA is based on the following reasons, (i) its ability to dilute the hydrogen-bonded network of clusters due to the non-polar nature of interactions between TBA and TOL (ii) TBA and TOL mixtures are completely miscible with each other at all compositions at the macroscopic scale, making a homogeneous and clear liquid. Additionally their

equivalent molecular diameters reduce the effect of their relative size difference on confinement induced phenomena and depends strongly on the nature of interactions between the confined molecules and the host matrix.

A remarkable effect of the role played by TOL in diluting TBA hydrogen-bonded netwowk of clusters is observed by the inability of TBA to crystallize below 25 °C by having as little as 10% by volume of TOL in the mixture. The following section discusses some of the physical properties of bulk TBA:TOL mixtures relevant for understanding the scientific results presented in subsequent chapters of this thesis.

C.3 Hydrogen-bonding network in TBA

TBA TOL bulk liquid mixtures have been studied in the past by Abdel Hamid et al. by a combination of neutron scattering and Raman spectroscopy[1,4,32]. As discussed in the brief description of TBA, the pre-peak seen in the static structure factor is a result of correlation between TBA molecules at different scales, firstly between individual TBA molecules forming associated n-mers (dimer,hexamer etc), secondly the correlation of TBA and its n-mers into nanoclusters and thirdly the existence of correlation between such nano-clusters. It was observed that by adding TOL to TBA, the intensity of this pre-peak decreases and continues to decrease with increasing amount of TOL up to near complete suppression at high TOL composition as shown in figure 1.20[1]. This is one first indication of the influence of a hydrophobic molecule on the hydrogen-bonded network of TBA, which appears to diminish.

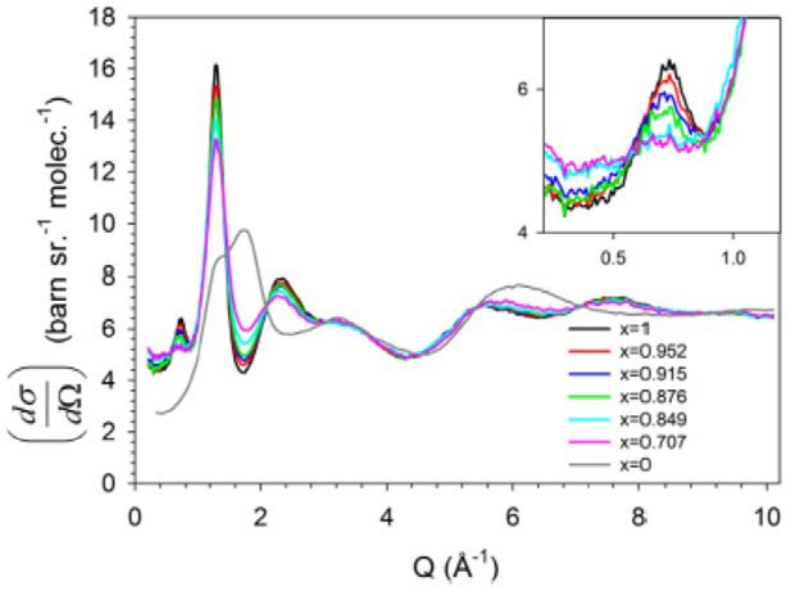

Figure 1.20: Suppression of pre-peak (inset) in the static structure factor of TBA:TOL mixtures obtained from neutron diffraction experiments. x denotes the volume fraction of TBA. Notice the significant lowering of pre-peak intensity even at $x \approx 0.7$.[1]

The authors examine this possibility by using Raman spectroscopy, which reveals

the existence of various populations of associated TBA molecules as shown in figure 1.21 (a). We observe an increase in the population of tetramers and hexamers with increasing volume fraction of TBA, which are capable of forming larger TBA clusters. An obvious consequence of increase in the hydrogen-bonded network is change in the electronic environment of a TBA hydroxyl group, which undergoes increasingly stronger electron shielding in large associated TBA clusters. The evidence of this is observed in the proportional decrease of ^{1}H NMR chemical shift ($\delta(-OH)$) of TBA hydroxyl group with its decreasing composition in the mixture up to $x_{TBA} \approx 0.2$ as shown in figure 1.21 (b), beyond which a more rapid decrease in its value is observed as the hydrophobic interactions of TBA-TOL dominates over hydrogen-bonding interactions amongst TBA such that its clusters break down and mostly TBA monomers exist, which are not electronically shielded as much strongly.

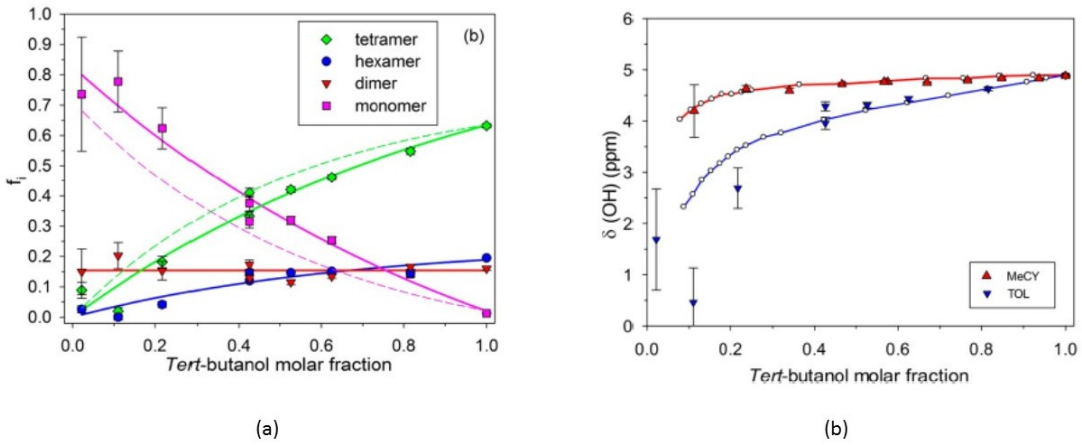

Figure 1.21: **(a)** The population fraction of hydrogen-bonded TBA clusters as a function of its molar fraction in TBA:TOL mixtures shown by symbols. The solid lines are guide for eye. **(b)** Chemical shift of -OH group of TBA as a function of its molar fraction for TBA:TOL mixtures shown by white circles and blue line. The blue triangles are predicted values from Raman spectroscopy. The red line, open circles on it and red triangles belong to TBA-methyl cyclohexane mixture which is not relevant for the current discussion.[1]

The effect of mixture composition on the extent of hydrogen-bonded cluster network can be expected to have consequences on the dynamics of TBA and TOL molecules when compared to their free state as discussed in the following section.

C.4 Dynamics of bulk TBA:TOL mixtures

Translational self-diffusion coefficients of TBA and TOL molecules in TBA:TOL bulk mixtures were studied previously using pulsed-field gradient stimulated echo NMR (PFG-STE NMR), a nuclear magnetic resonance technique highly suited for self-diffusion dynamics studies, details of which will be given in the next chapter.

Figure 1.22 shows the diffusion coefficients of TBA (full circles) and TOL (open circles) in TBA:TOL mixtures as a function of TBA volume fraction. We notice that the diffusion

coefficients of TOL are greater by a factor of about 1.5 for most concentrations in spite of the two molecules having comparable Van der Waals diameter. The hydrogen-bonded clusters of TBA have a much larger hydrodynamic radii, thus diffusing much slower at high TBA compositions. Obviously the steric restriction experienced by TOL at high TBA concentration reduces its diffusion coefficient as well.

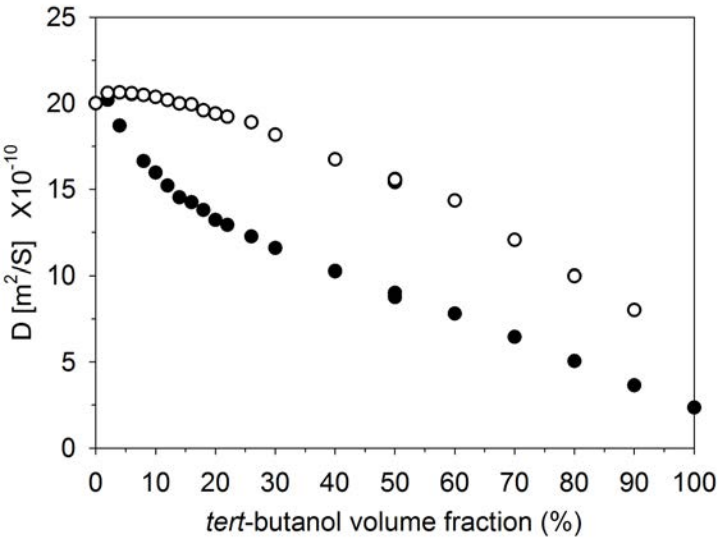

Figure 1.22: Translational diffusion coefficients of toluene (open circles) and tert-butanol (solid circles) in their bulk binary solutions.[32]

As the concentration of TBA decreases, the size of hydrogen-bonded clusters continue to break down allowing faster dynamics to both molecules such that they nearly converge at high TBA dilution.

Within the context of phenomena at thermodynamic equilibrium its not only interesting to understand the nature of binary liquids but also phenomena corresponding to the interaction of their binary gas mixture with a nanoporous substrate.

C.5 Binary liquid-gas equilibria

In understanding phenomena involving gas-solid interaction such as adsorption, it is imperative to have accurate information of gas mixture composition in order to correctly characterise multi-component adsorption. In this section we report the TBA:TOL binary gas composition at any given temperature from its corresponding known binary liquid composition utilizing well-established theoretical knowledge on thermodynamics of liquid-vapour equilibria.

The activity coefficients γ_{TBA} and γ_{TOL} of TBA and TOL respectively could be calculated through the *Margulès* model for binary liquids[54]as shown in equations 1.6 and

1.7.

$$\gamma_{TBA} = \exp\left(\frac{(A+3B)(1-x)^2 - 4B(1-x)^3}{RT}\right) \tag{1.6}$$

$$\gamma_{TOL} = \exp\left(\frac{(A+3B)x^2 + 4Bx^3}{RT}\right) \tag{1.7}$$

x is the volume fraction of TBA in the TBA:TOL liquid mixture. The coefficients A and B have been determined empirically by Martinez-Soria et al[60] where the thermodynamic data for liquid-vapour equilibrae of TBA:TOL are available. The saturation pressures of pure components were calculated from Antoine equation as shown in equation 1.8.

$$P_i^{sat} = a_{1i} \exp\left(-\frac{a_{2i}}{T + a_{3i}}\right) \tag{1.8}$$

The Antoine constants for TBA and TOL a_{ni} were obtained from the literature[62]. Utilizing the values of γ_i and P_i^{sat} obtained from equations 1.6, 1.7 and 1.8 respectively, we calculate the volume fraction of TBA y in the binary gas from Henry's law[62].

$$\frac{1}{y} = 1 + \frac{1-x}{x}\frac{P_{TOL}^{sat}}{P_{TBA}^{sat}}\frac{\gamma_{TBA}}{\gamma_{TOL}} \tag{1.9}$$

In figure 1.23 we see how y_{TBA} varies with x_{TBA} at room temperature.

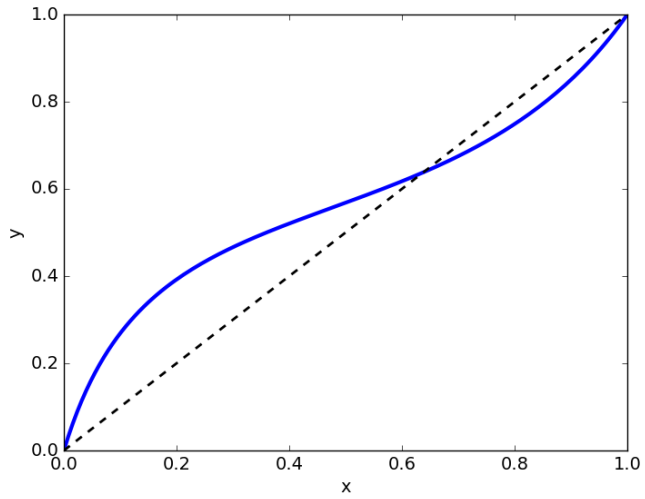

Figure 1.23: Volume(mole) fraction of TBA y in the binary gas at thermodynamic equilibrium with the liquid solution with volume fraction of TBA x at T=35 °C. The dashed line is a guide for the eye.

We now proceed to discuss briefly how the bulk properties of TBA:TOL mixtures vary with change of mixture composition. The viscosities and densities of TBA:TOL mixtures have been reported previously in the literature for different temperatures. In the following section we report the bulk surface tensions of TBA:TOL mixtures determined experimentally at two different temperatures.

C.6 Surface tension measurements of binary liquid mixtures

The Pendant Drop Technique was used to determine bulk surface tensions of TBA, TOL and their mixtures for the liquid-air interface at 25 °C and 35 °C respectively[33]. This technique analysis the drop profile, which is a balance between Laplace pressure, which tries to give the drop a spherical shape and hydrostatic pressure due to gravitation which pulls it down. The setup consisted of a light source, an optical camera and a drop suspended between them with the aid of a micro-syringe (figure 1.24). The drop profile is described by a series of equations (Hansen and Rodsrud 1990)shown below obtained from Young-Laplace equation, the numerical fit of which to the drop shape captured by the camera gives us the surface tension[33].

$$\frac{d\theta}{ds} = 2 - \beta y - \frac{\sin\theta}{x}$$

$$\frac{dx}{ds} = \cos\theta$$

$$\frac{dy}{ds} = sin\theta$$

Where β is related to the surface tension σ as

$$\sigma = \rho \times g \times r_0^2/\beta$$

Where ρ is the mass density of the liquid/liquid mixture, g is acceleration due to gravity and r_0 is the radius of curvature at lowest point of the pendant drop.

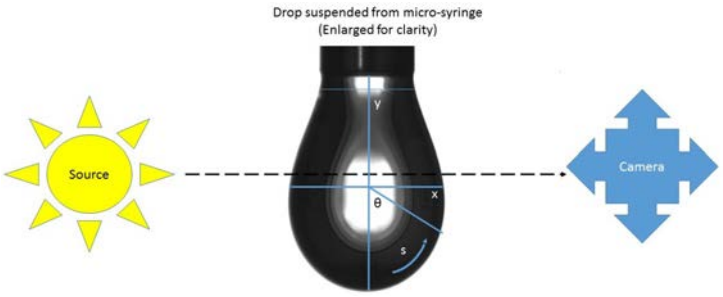

Figure 1.24: Experimental setup of pendant drop method for determination of surface tension.

The experimental values of surface tensions obtained for the bulk mixtures will be used in subsequent chapters. Having discussed the information on physical properties of TBA and TOL mixtures relevant to the scientific discussions of this thesis, we now proceed to the description of host matrices used for studying confinement induced effects on these binary mixtures.

D Properties of host matrices

D.1 MCM-41

Mobil Composition of Matter-41 or popularly known as MCM-41 is a nanoporous silica developed by Mobil research group in 1992[44]. With a pore size ranging between 2-4nm, it provides a spatial dimension of confinement highly suitable for understanding the role played by a balance of interactions between adsorbate-adsorbate and adsorbate-adsorbent on the structure and dynamics of confined matter. Its a highly crystalline material, with great two-dimensional periodicity of its pores. MCM-41 materials have cylindrical parallel pores and are known to have quite narrow pore-size distribution with very little inter-connections between pores[49]. This makes it a preferred material for studying nanoconfinement phenomena. Additionally it is chemically quite inert and has been in use already for a long time in chemical industry, especially for catalysis, gas separation and adsorption. Its presence in the powder form makes its manipulation easier for structural and dynamic studies in the filled state using a variety of techniques such as diffraction, NMR, vapour sorption etc.

D.2 SBA-15

Santa Barbara Amorphous-15 type material or SBA-15 is a nanoporous silica which like MCM-41 has highly ordered parallel pores present in a hexagonal arrangement. The synthesis technique of SBA-15, a sol-gel process[75], details of which shall be given later in this section, facilitates the formation of larger pores having pore diameters between 8-9nm and greater wall thickness than MCM-41. This additional wall-thickness gives improved thermo-mechanical properties[13] highly desirable for functions like catalysis and gas separation. The larger pore size allows for confining great amount of adsorbate which provides a greater gradient in the nature of interactions occurring at the pore-wall and core of the adsorbed material. SBA-15 pores have been to exhibit a unique feature of having corrugated pores walls and tortuous pores along their length instead of straight cylindrical, giving rise to regions of microporosity[39]. Such tortuous profile of pore increases the overall pore-length from end to end which makes it an interesting material to study self-diffusion phenomena of molecules confined in its pores over longer time scales.

D.3 CMK-3

CMK-3, a Carbon Molecular Sieves type of material is a carbon-replica of SBA-15, using it as a template for its structure[42]. CMK-3 materials naturally have a reduced pore diameter (3.5-6nm) compared to SBA-15, as the carbon walls formation takes place at the interior of SBA-15 pores. CMK-3 pores are reported to have inter-connection between its pores though narrow channels, which gives rise to a significant microporosity. Its pore walls are completely made of carbon resembling carbon-nanotubes, larger in diameter though. This changes the chemical nature of pore walls when compared to SBA-15 from hydrophilic to hydrophobic which makes it more interesting to investigate the role played by specific interactions between the confined molecules and pore-wall in being able to switch the structural and dynamic characteristics of confined molecules.

D.4 Vycor®

Vycor is a monolithic silica glass provided by Corning Inc. While it is mostly silica (96%), Vycor does constitute certain amount of boron trioxide (4%). The pores of Vycor which instead of being cylindrical or long enough to give a nano-rod like appearance are a complex network of highly disordered meandering pores[31]. The pore diameter varies between 7-10nm) generally, but larger variations are not unlikely. Vycor is a material with high thermo-mechanical stability. Vycor is a fairly well machinable materials, making it possible to create specific geometries desirable for rheological studies via radiography, optical methods and as membranes or blocks for fluid dynamics studies under pressurized liquids or simply capillary rise action. Being made of silica, Vycor pore walls are highly wetting, i.e. the contact angle made by a confined liquid with the pore wall is almost zero. Vycor usually has a sizeable pore distribution in the form of several capillary bridges and branching of larger pores into narrower ones, which produces some interesting rheological effects which shall be discussed in chapter 4.

D.5 Brief description of synthesis techniques

D.5.1 MCM-41: The synthesis technique of MCM-41 powder has been long established[50] and was used to synthesize in our laboratory at the *Institut de Physique de Rennes*, with morphological specifications found most suitable in the context of this work.

MCM-41 is synthesized using a hydrothermal synthesis method where cationic surfactants present in a basic medium self-assemble into rod-like micelles arranged in a hexagonal lattice to form a template in which silica molecules assisted by water condense in subsequent stages, such that we have highly ordered rod-like structures made of silica molecules[30].

The pore morphology depends strongly on the length of carbon chain of the surfactant used. For the synthesis of MCM-41 C-16 type nanoporous matrix we use hexadecyltrimethylammonium bromide ($CH_3(CH_2)_{15}N(Br)(CH_3)_3$, (Alrich $C_{16}TABr$ 98%), a water-soluble cationic surfactant as the template material, 4.8 g of which was dissolved in 240 ml of distilled water. The mixture was stirred at 700rpm at 40 °C until a clear solution was obtained. The importance of stirring above temperature was to accelerate the chemical kinetics. In the following step aqueous ammonia solution to change the pH of solution from acidic ($\approx$ 5.4) to basic ($\approx$ 11). 20 ml of the silica source tetraethylsiloxane ($Si(OC_2H_5)_4$ TEOS Aldrich 98%) was added thereafter. The temperature was maintained at 40 °C for next two hours for the reaction to complete.

A white precipitate is formed at the end of reaction process which was filtered by Buchner filtration using 300 ml of distilled water to remove any remaining reactants. The filtered powder was dried in an oven for 17 hours at 90 °C to remove adsorbed water. In the final step remaining surfactant molecules were eliminated by calcining the powder gradually from room temperature to 550 °C over a period of 5 hours and then maintaining at this temperature for 5 more hours. The final result was 5 g of MCM-41 white, uniform powder.

D.5.2 SBA-15: SBA-15 was synthesized in our laboratory following one of the most cited synthesis routes available[13]. Preparation of SBA-15 is followed by a sol-gel process where an amphiphilic non-ionic triblock copolymer is used as a template around which the silica precursor is polymerized.

4 g of the the polymeric template material called Pluronic (P_{123}) was dissolved in a solution of 125 g distilled water and 25 g of hydrochloric acid (38%) in order to provide an acidic medium. The solution was prepared by stirring at 40 °C for 3 hours following which 8.6 g of the silica precursor (TEOS) was added. This was followed by ten more minutes of vigorous stirring after which the stirring was stopped and the solution was aged for the next 24 hours with temperature maintained at 40 °C.

Thereafter the solution was aged without stirring for 24 hours again at 100 °C under reflux conditions which resulted into formation of a white precipitate. A Buchner filtration process similar to that in MCM-41 was carried out with 300 ml of distilled water at room temperature to remove residual reactants. The filtrate was pre-dried at room temperature for 24 hours and subsequently oven dried at 550 °C for 18 hours to obtain SBA-15 powder.

D.5.3 CMK-3: CMK-3 materials were synthesized in the laboratory using SBA-15 as the starting material[42]. A solution of 1.25 g sucrose and 0.14 g sulphuric acid was made in 5 g water. Sucrose is the source of carbon forming material, while SBA-15 is the template. 1 g of SBA-15 was added to the sucrose solution and heated in an oven at 100 °C for six hours, followed by six more hours of heating at 160 °C. Under these conditions sucrose undergoes polymerization in the pores of SBA-15 which serve as a template. 0.8 g and 0.09 g of additional sucrose and sulphuric acid were added to ensure complete coverage of silica surface with hydrocarbon material.

The resulting material was subjected to pyrolysis treatment at 900 °C for six hours under a nitrogen flux to prevent oxidization and effectively remove all hydrogen from the polymer covering pore-walls and converting it into purely carbon walls. Unlike usual synthesis routes, the silica template was not removed in order to retain the ordered structure. However the aim of synthesis, which was to produce carbon pore-walls was met. The resulting CMK-3 powder as a consequence retains certain amount of silica mostly present in external surfaces such exterior of pore walls.

Figure 1.25 (a) shows the diagrammatic representation of synthesis of ordered nanoporous silica (MCM-41 or SBA-15) depending on the template material used. Figure 1.25 (b) shows the use of SBA-15 template for synthesizing CMK-3 matrix.

D.6 Microstruture

In this section we discuss briefly the microstructure studies conducted on MCM-41 and SBA-15 using Scanning Electron Microscopy (SEM) and Transmission Electron Microscopy (TEM). SEM images are obtained a beam of electrons which are scattered from a given surface, thus giving important information on the particle morphology with a resolution of ≈ 10 nm. On the other hand, TEM is a technique in which a focused beam of electrons is transmitted through a very thin membrane of sample revealing important information at a length scale of ≈ 1 nm The measurements were conducted in the framework of Dr.

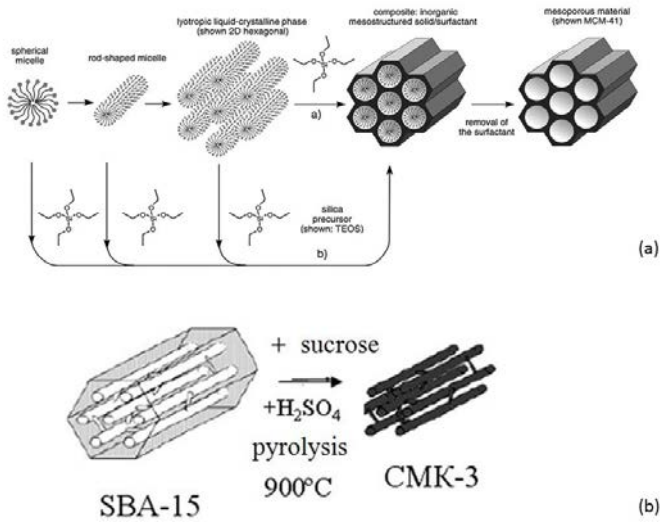

Figure 1.25: **(a)**Synthesis route of ordered nanoporous silica. The micellar template forming material is either CTAB ($C_{16}TABr$) or Pluronic (123) ($HO-(CH_2CH_2O)_{20}-(CH_2CHO)_{70}-(CH_2CH_2O)_{20}-H$) for synthesizing MCM-41 or SBA-15 respectively[27]. **(b)** Use of SBA-15 as a template for polymerizing sucrose in acidic medium provided by sulphuric acid, following by subsequent pyrolysis to obtain CMK-3. It is important to note here that the CMK-3 synthesized in the laboratory retains its silica template unlike shown in figure.

Ramona Mhanna's doctoral thesis at the *Institut de Physique de Rennes*[55].

Figure 1.26 (a) shows the SEM images of MCM-41 agglomerates which are roughly hexagonal in shape. The particle size was found to be roughly 1 µm. Figure 1.26 (b) shows the TEM images of MCM-41 in two orientations, one with axis of viewing parallel to cylindrical pore channels (A) and second perpendicular to pore channels (B). The hexagonal two-dimensional lattice arrangement of pores are highlighted by the red spots in (A), while their parallel arrangement is highlighted by red lines in (B).[55]

Figure 1.27 (a) shows SBA-15 particle-agglomerates which in contrast to MCM-41 appear slender and longer indicating a greater pore-length to pore diameter ratio. Figure 1.27 (b) (D) (on right) shows arrangement of SBA-15 pores parallel to each other (red lines) similar to MCM-41.[55]

D.7 Crystalline structure

In the following section we discuss the structural information on the lattice arrangement of the ordered porous matrices synthesized in our laboratory, i.e. MCM-41, SBA-15 and CMK-3 derived from powder x-ray diffraction measurements. The small wavelength and high intensity of x-rays combined with its ability to elastically scatter with electron clouds make them an indispensable tool for accurate determination of crystalline structures at the molecular level down to few angstroms.

The experiments were carried out at 25 °C using an x-ray wavelength of $\lambda = 1.54$ Å[55].

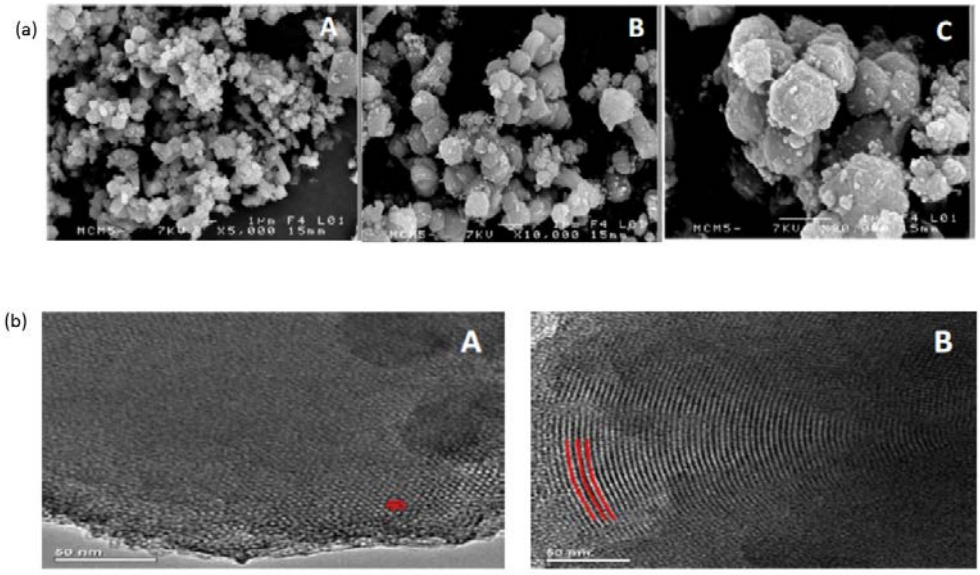

Figure 1.26: **(a)** SEM images of MCM-41 featuring particles of hexagonal geometry. **(b)** TEM images of MCM-41 particles in axis of viewing parallel (A) and perpendicular (B) to the pore-axis.[55]

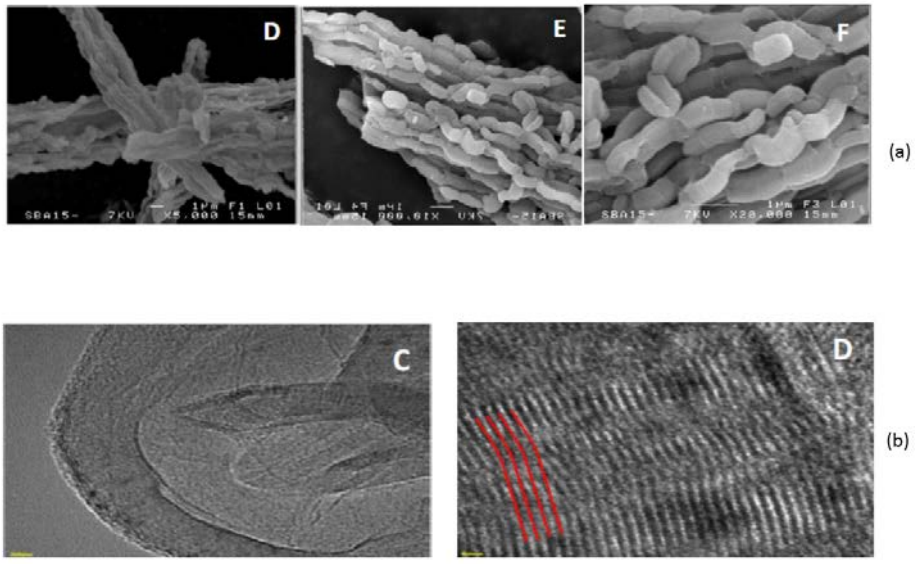

Figure 1.27: **(a)** SEM images of SBA-15 featuring long particle size, an indication of larger pore-length to diameter ratio. **(b)** TEM images of SBA-15 particles in axis of viewing parallel (C) and perpendicular (D) to the pore-axis.[55]

The scattering angle θ, i.e. the angle with respect to the sample at which a detector detects scattered x-ray is related to the scattering vector q by the equation $q = \frac{4\pi \sin\theta}{\lambda}$,

which is in turn related to the inter-planar distance d between lattice planes by the Bragg equation as $d = \frac{2n\pi}{q}$.

Figure 1.28[55] shows the x-ray diffraction patterns of MCM-41, SBA-15 and CMK-3. The Bragg reflections (1 0), (1 1), (2 0) and (2 1), which characteristics of hexagonal lattice arrangement were observed for MCM-41, which is commensurate with its TEM images discussed in previous section. The most intense peak at (1 0) reflection primarily represents the arrangement of pores. The inter-planar distance for this reflection $d_{(10)}$ was reported to be 3.8 nm for MCM-41. The lattice parameter $a_{(10)}$ is related to inter-planar distance by the relation $a = \frac{2d_{(10)}}{\sqrt{3}}$.

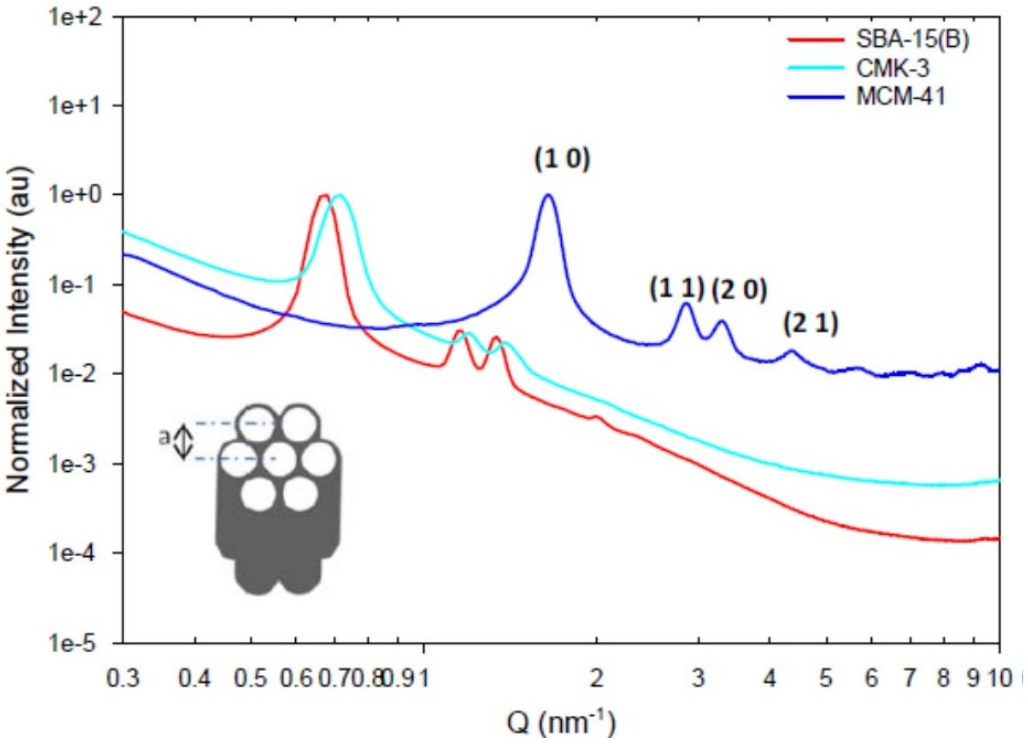

Figure 1.28: Powder X-ray diffraction patterns of MCM-41 (blue), SBA-15 (red) and CMK-3 (cyan). The Bragg reflections are indicated for MCM-41. In the inset is given a diagrammatic representation of hexagonal arrangement of pores and the lattice parameter.[55]

The Bragg reflections of SBA-15 show a P6mm type of ordering, which natrually persists in CMK-3. The shifting of Bragg peaks to lower Q values in comparison to MCM-41 indicate a larger pore structure. The absolute scattered intensity of CMK-3 peaks were reportedly lower than SBA-15 by five orders of magnitude and the author has presented a magnified view of the diffraction pattern for clarity. Such lowering of intensity can be attributed to two things, firstly, CMK-3 is mostly carbon, an element of low-atomic number and consequently very low form factor. As x-ray diffraction is sensitive to the electron density of an atom, low atomic number elements like carbon equally sensitive

to x-rays as silicon. Secondly, a loss of pore ordering observed by the disappearance of fourth Bragg peak for CMK-3 might as well be an additional reason for overall diminished intensity of Bragg peaks.

D.8 Pore size, volume and specific surface area

One of the most efficient tools for pore morphology characterisation is vapour sorption. Adsorption of molecules is a highly gradual process in thermodynamic equilibrium. While adsorption of first molecular layer on the surface of a substrate at low pressures of the adsorbing gas can help determine the specific surface area of the pores, adsorption up to complete filling of pores by condensation of vapours into liquid helps obtain the porous volume of the substrate. In this section is reported the use of nitrogen adsorption isotherms at 77 K carried out on MCM-41, SBA-15 and CMK-3 using an ASAP Micromeretics instrument and on Vycor using a Quantachrome®ASiQwin™instrument in order to determine essential information on its pore characteristics.

Figure 1.29[55] shows the nitrogen vapour sorption isotherms of MCM-41 and two variants of SBA-15 ((A) and (C). A Brunauer, Emett and Teller (BET) analysis[14] of the isotherms at low relative pressures (0.15 $\geq$) where the volume of nitrogen gas adsorbed V at a relative pressure P/P_0 is related to the volume of nitrogen necessary to make a monolayer V_m by the following expression.

$$\frac{1}{V \times \left[\frac{P_0}{P} - 1\right]} = \frac{1}{CV_m} + \frac{C-1}{V_m C}\frac{P}{P_0}$$

Where C is known as the BET constant which gives the extent of thermodynamic affinity of a surface for the adsorbing molecules. Fitting the above linear equation of $\frac{1}{V \times \left[\frac{P_0}{P} - 1\right]}$ versus P/P_0 gives the slope $dfracC - 1V_mC$ and intercept $\frac{1}{CV_m}$ needed to obtained volume occupied by a monolayer, from which the specific surface area occupied by the adsorbed species can be determined.

On the other hand, volume uptake per gram of sample in figure 1.29 directly gives a measure of the sample porosity.

Figure 1.30 (a) and (b) show the nitrogen vapour sorption isotherms for CMK-3 and Vycor respectively. It must be noted that the y-axis here does not represent volume uptake by the sample and is instead the volume of nitrogen using in the bath of experimental setup for vapour sorption.

Observing the shapes of isotherms we notice that MCM-41 and SBA-15 have a similarity in their shapes. Such isotherms are characteristic of type IV sorption-isotherms, in which a gradual linear mass rise corresponding to formation of first monolayers takes place, which is followed by an immediate step rise at a certain pressure known as capillary condensation pressure, beyoond which the adsorbing vapour molecules condense into liquid state and occupy the porous volume completely.

The adsorption isotherm for Vycor on the other hand resembles more a type II isotherm where the monolayer build up continues till quite high relative pressures which is followed by a smoother capillary condensation.

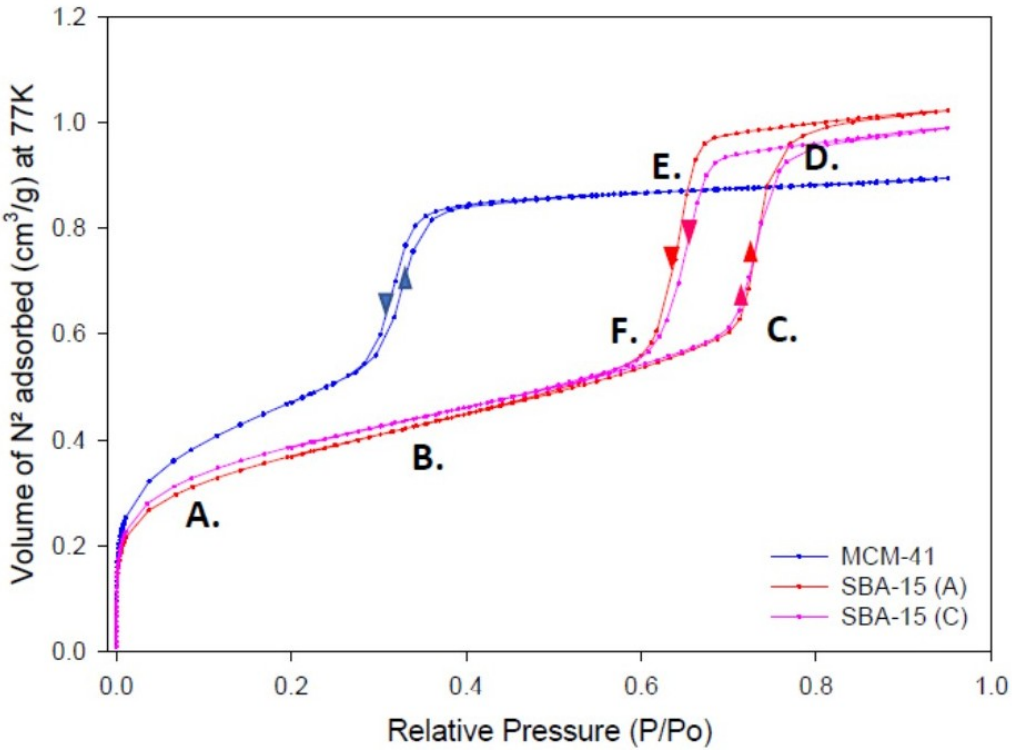

Figure 1.29: Nitrogen vapour sorption isotherms of MCM-41 (blue) and two variants of SBA-15 (A)(red) and (C) (red) at 77 K up to a relative pressure 0.95 to the saturation pressure.[55]

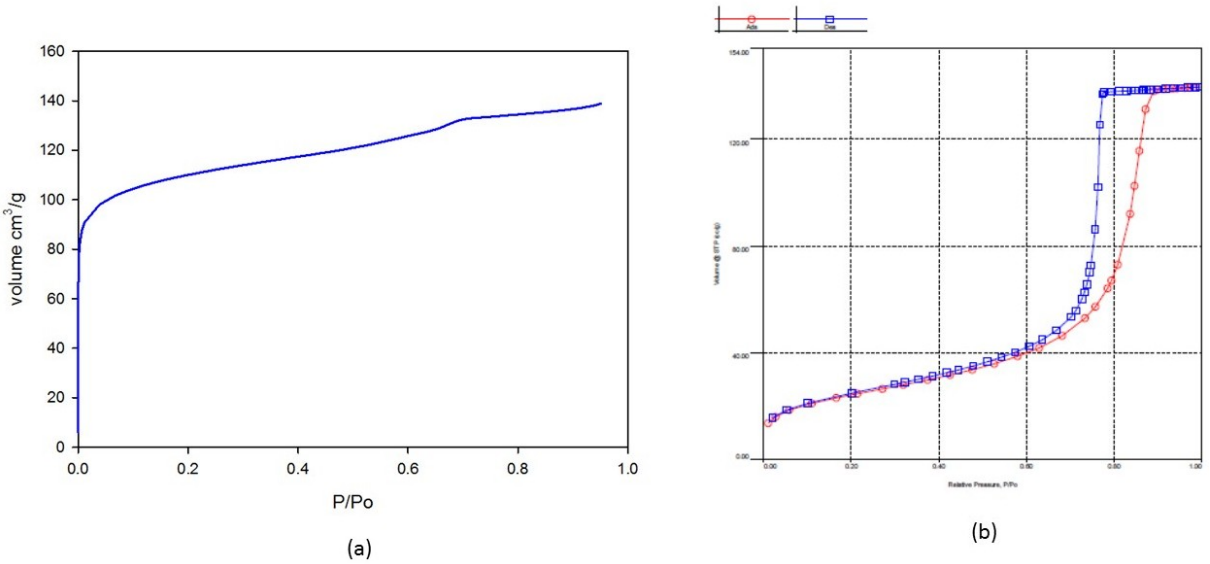

Figure 1.30: Nitrogen vapour sorption isotherms of CMK-3(a) and Vycor(b). The y-axis does not represent absolute volume uptake of the samples, instead are a measure of nitrogen used in the bath for experiment.

We notice that the adsorption isotherm for CMK-3 has elements of type IV isotherm, seen by its gradual linear volume uptake, which is followed by a step increase in volume uptake. However unlike MCM-41 and SBA-15, this step rise does not occur at a single relative pressure but over a certain relative pressure range. We shall discuss this issue more in detail in chapter 3. At present, we focus more specifically on use of the nitrogen-adsorption isotherm for determination of specific surface area and volume porosity of the porous matrix.

Additionally another important use of nitrogen vapour sorption isotherms is the determination of pore-size and its distribution for our porous matrices. One of the most preferred analysis technique for determining the same was given by Barret, Joyner and Halenda, the analysis technique known popularly as the BJH treatment[10] which assumes pores to be cylindrical and is based on the Kelvin equation which relates pore size to capillary condensation pressure. In figures 1.29[55] and 1.30 we clearly observe that the capillary condensation step does not occur sharply on one pressure, but smeared over a pressure range, which is very little for MCM-41 and SBA-15, but significant for CMK-3. The pore size distributions of SBA-15(A)[55], CMK-3 (laboratory synthesized) and Vycor sample (commercial) are shown in figure 1.31 (a), (b) and (c) respectively. We observe that SBA-15 has quite a uniform pore size even though the pore size distribution is not very narrow. Vycor on the other hand has quite narrow pore size distribution (blue curve and open squares), while CMK-3 has the largest pore size distribution ranging from microporosity to macroporosity, thus the most probable pore diameter (5.6 Å) was found to be different than the average pore diameter (3.9 Å)

D.9 Summary of properties

In the table below are listed the pore morphological properties of the chosen host matrices for confinement which are most relevant to the scientific discussions presented in this thesis.

Host matrix	BET specific surface area ($m^2\,g^{-1}$)	Volume porosity ($cm^3\,g^{-1}$)	Pore diameter (nm)
MCM-41[55]	960	0.67	3.4
SBA-15[55]	822	1.07	7.8
CMK-3	368	0.22	3.9(average),5.6 (most probable)
Vycor	104	0.22 0.32(vol/vol)	9.08

E State of the art

The structural and dynamic studies of TBA:TOL mixtures in MCM-41 and SBA-15 pores have already been reported using a combination of neutron scattering techniques and differential scanning calorimetry in the works of Ramona Mhanna et al. and Abdel Hamid et al.[2–4,55]

Ramona Mhanna et al. prepared isotopic mixtures of TOL (TOL-H and TOL-D), TBA (TBA-H and TBA-D) and TBA:TOL (TBA-H/D and TOL-H/D) mixtures in order

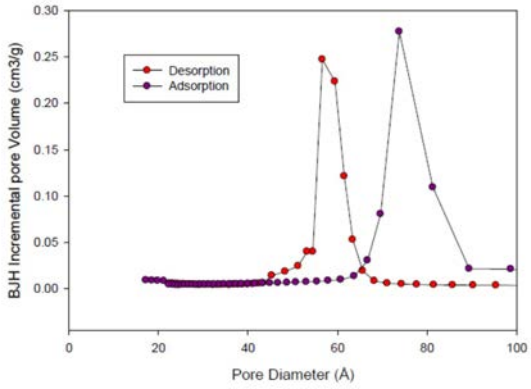

(a)

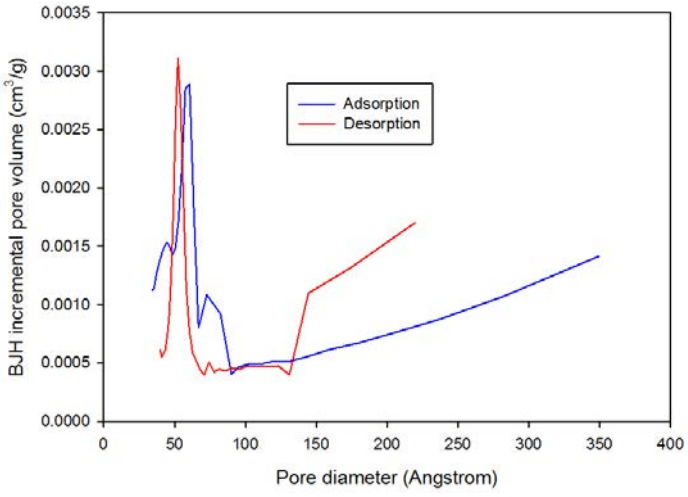

(b)

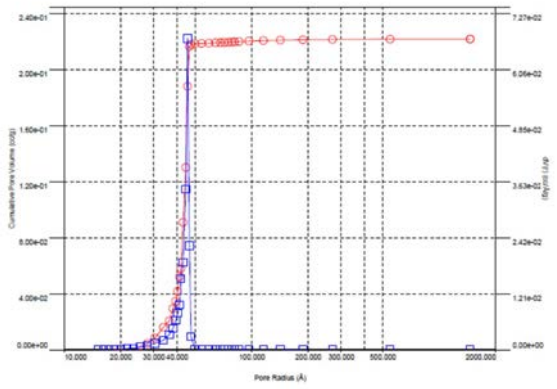

(c)

Figure 1.31: Pore size distribution of SBA-15(a)[55], CMK-3(b) and Vycor(c) obtained from BJH-treatment of the nitrogen vapour sorption isotherms.

to have the same neutron scattering length density as silica, a method known as contrast matching[55]. Thus upon filling SBA-15 pores completely with this mixture, the system must appear as a homogeneous bulk silica without any pores as a consequence of which one expects extinction of the neutron diffraction Bragg peaks of SBA-15. While this was

true for contrast matched TOL or TBA pure liquids (1.32(a)), in the case of TBA:TOL mixtures the persistence of (1 0) Bragg reflection characteristic of hexagonal arrangement of pores indicated presence of an inhomogeneity inside the pores (1.32(b)). The experimental neutron diffraction pattern could be well explained by a core-shell model of phase separation (1.32(c)), made up of a one-monolayer thick TBA-shell and a core made up of TOL. Interestingly the opposite case, i.e. a TOL shell and a core of TBA could not fit with the experimental observations which was rationalized by TBA's ability to form hydrogen-bonded network which might extend to forming such H-bonds with the hydrophilic silica. Existence of this TOL-TBA core-shell model was demonstrated earlier for confinement in MCM-41 pores as well[3].

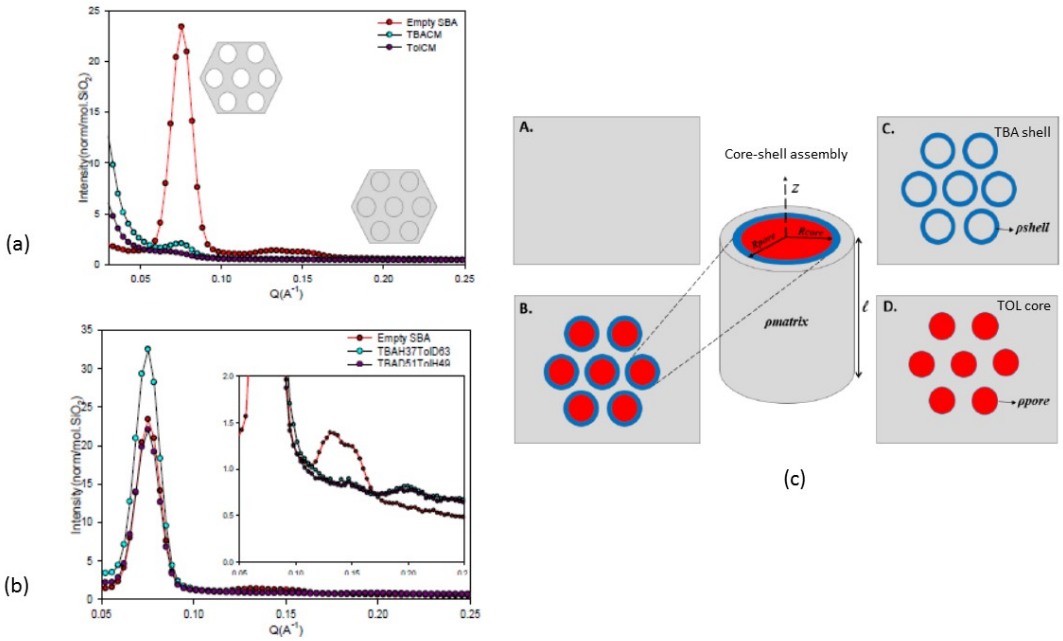

Figure 1.32: **(a)** Contrast matched TBA and TOL leading to near extinction of SBA-15 Bragg peaks.
(b) Persistence of Bragg-peak upon filling pores with TBA:TOL contrast matched mixture. Evidence of inhomogeneity.
(c) Core-shell model showing TBA forming the shell and TOL constituting the core.[32,55]

Abdel Hamid et al. combine neutron scattering and DSC to reveal the existence of two different glass transitions for TBA:TOL mixtures confined in silica nanopores (MCM-41,SBA-15) indicating the presence of two region with different relaxation dynamics[2]. Additionally a slowdown in the TBA liquid relaxation dynamics and suppression of glassy modes was observed. The above mentioned TOL-TBA core-shell model gives a possible explanation of the existence of two regions with different glassy dynamics, even though their thicknesses vary from one (monolayer shell) to few molecular layers. The phase-separation of TBA and its possible interaction with the silica surface provides an explanation for the slowing down of its dynamics. Figure 1.33 shows the differential of

DSC thermograms of TBA:TOL mixtures of variations compositions denoted by the volume fraction x of TBA, confined in MCM-41 pores. We notice clearly the emergence of two separation glass transition temperatures, indicated by the peaks, as for mixture compositions as low as $x = 0.065$.

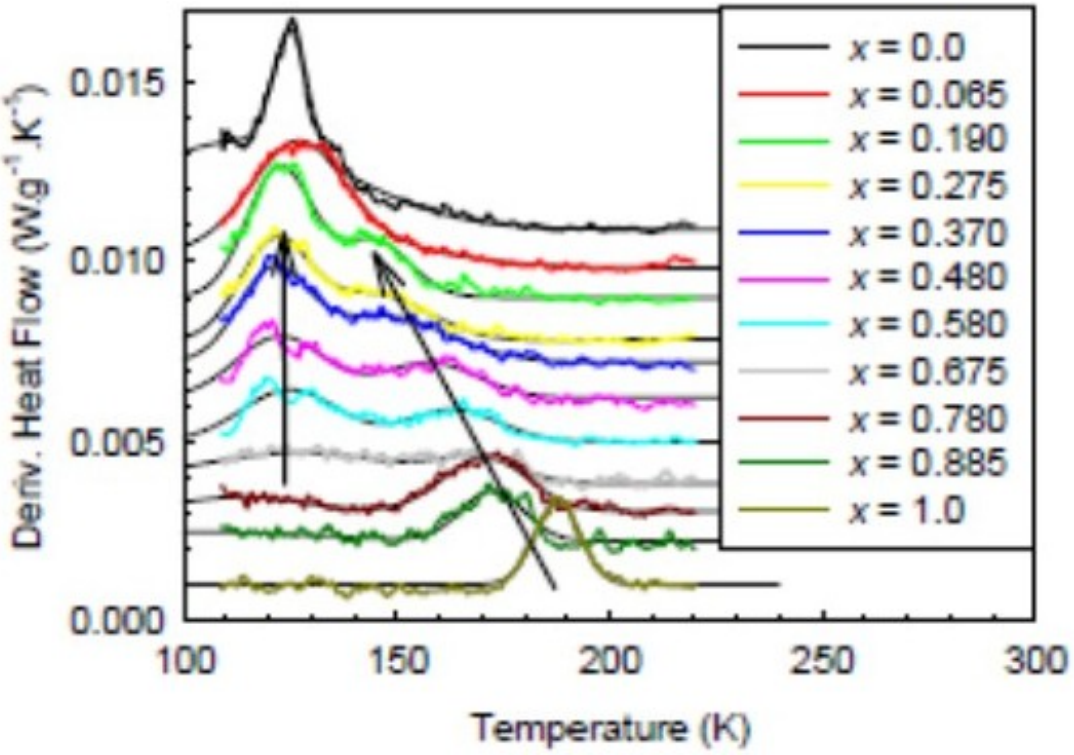

Figure 1.33: Derivative of heat flow versus temperature for TBA:TOL mixtures as well as pure liquids confined in MCM-41. The arrows point to the existence of two different peaks indicating two separate $T_g s$.[2]

IV Organization of thesis

The application of neutron diffraction as mentioned in the previous section has brought essential structural information on the nature of molecular ordering and phase separation of TBA:TOL mixtures confined in ordered silica nanopores, which have been equally well supported from the investigations made on the dynamics of these nanoconfined binary liquids. In the current thesis, we approach TBA:TOL binary systems from a different perspective than has been adopted so far to find whether we converge with what has been already established while simultaneously deepening our understanding of these systems by answering some completely new questions.

Chapter 2 deals with systems in static equilibrium conditions. It presents a nuclear magnetic resonance study of TBA:TOL binary liquids confined in MCM-41 and SBA-15 pores. ^{1}H Magic Angle Spectroscopy NMR has been used to seek information from a structural point of view by investigating the nature of molecular interactions present in

the nanoconfined TBA:TOL mixtures. Pulsed Field Gradient NMR technique has been utilized to investigate the influence of nanoconfinement on the self-diffusion dynamics of our binary liquids when compared to the bulk state.

Chapter 3 extends the approach to dynamic equilibrium studies by analyzing the adsorption characteristics of TBA:TOL binary gas mixture adsorbing in MCM-41 and CMK-3 pores. A thermodynamic model is developed in order to explain the role played by competing intermolecular interactions between adsorbing species of a multi-component gas and the pore surface which leads to structural organization under nanoconfinement.

Chapter 4 tests whether the established effects on structure and dynamics of nanoconfined binary liquids under equilibrium (static and dynamic) hold equally true under out of equilibrium conditions by investigating the spontaneous imbibition of TBA:TOL binary liquids through a network of silica nanopores by using gravimetric and neutron radiography methods.

Bibliography

[1] A R Abdel Hamid, Ronan Lefort, Y Lechaux, Alain Moréac, Aziz Ghoufi, Christiane Alba-Simionesco, and Denis Morineau. Solvation effects on self-association and segregation processes in tert-butanol-aprotic solvent binary mixtures. *The journal of physical chemistry. B*, 117(35):10221–30, sep 2013.

[2] Abdel Razzak Abdel Hamid, Ramona Mhanna, Pierre Catrou, Yann Bulteau, Ronan Lefort, and Denis Morineau. Multiple Glass Transitions of Microphase Separed Binary Liquids Confined in MCM-41. *The Journal of Physical Chemistry C*, 120(20):11049–11053, may 2016.

[3] Abdel Razzak Abdel Hamid, Ramona Mhanna, Ronan Lefort, Aziz Ghoufi, Christiane Alba Simionesco, Bernhard Frick, and Denis Morineau. Micro-Phase Separation of Binary Liquids Confined in Cylindrical Pores. *The Journal of Physical Chemistry C*, page acs.jpcc.6b01446, apr 2016.

[4] Razzak Abdelhamid Abdel, C Alba-Simionesco, B Frick, Aziz Ghoufi, Ronan Lefort, Ramona Mhanna, Alain Moréac, and Denis Morineau. Mesoscopic order of bulk and nanoconfined H-bonded binary liquid mixtures. In *"Structure of disordered systems" opening celebration of the new 7C2 spectrometer*, Saclay, France, 2013.

[5] Gerold Adam and Julian H Gibbs. On the temperature dependence of cooperative relaxation properties in glass-forming liquids. *The journal of chemical physics*, 43(1):139–146, 1965.

[6] Shashishekar P Adiga, Chunmin Jin, Larry A Curtiss, Nancy A Monteiro-Riviere, and Roger J Narayan. Nanoporous membranes for medical and biological applications. *Wiley interdisciplinary reviews. Nanomedicine and nanobiotechnology*, 1(5):568–81, jan.

[7] Dagfinn W Aksnes, Kjersti Førland, and Michael Stöcker. 1 h nmr relaxation and diffusion studies of cyclohexane and cyclopentane confined in mcm-41. *Microporous and mesoporous materials*, 77(1):79–87, 2005.

[8] S Amali, Lis Wollesen Petersen, and DE Rolston. Modeling multicomponent volatile organic and water vapor adsorption on soils. *Journal of hazardous materials*, 36(1):89–108, 1994.

[9] Fabrice Audonnet, Nancy Brodie-Linder, Denis Morineau, Bernhard Frick, and Christiane Alba-Simionesco. From the capillary condensation to the glass transition of a confined molecular liquid: Case of toluene. *Journal of Non-Crystalline Solids*, 407:262–269, sep 2015.

[10] Elliott P Barrett, Leslie G Joyner, and Paul P Halenda. The determination of pore volume and area distributions in porous substances. i. computations from nitrogen isotherms. *Journal of the American Chemical society*, 73(1):373–380, 1951.

[11] James Munsie Bell and FK Cameron. The flow of liquids through capillary spaces. *The Journal of Physical Chemistry*, 10(8):658–674, 1906.

[12] Pilar Brocos, Alfredo Amigo, and M Guadalupe Lemus. Extended Langmuir Isotherm for Binary Liquid Mixtures. (14):4261–4266, 2001.

[13] Nancy Brodie-Linder, Gilberte Dosseh, Christiane Alba-Simonesco, Fabrice Audonnet, and Marianne Impéror-Clerc. Sba-15 synthesis: Are there lasting effects of temperature change within the first 10min of teos polymerization? *Materials chemistry and physics*, 108(1):73–81, 2008.

[14] Stephen Brunauer, P. H. Emmett, and Edward Teller. Adsorption of Gases in Multimolecular Layers. *Journal of the American Chemical Society*, 60(2):309–319, feb 1938.

[15] Sachin Chavan, Jenny G Vitillo, Diego Gianolio, Olena Zavorotynska, Bartolomeo Civalleri, Søren Jakobsen, Merete H Nilsen, Loredana Valenzano, Carlo Lamberti, Karl Petter Lillerud, et al. H 2 storage in isostructural uio-67 and uio-66 mofs. *Physical chemistry chemical physics*, 14(5):1614–1626, 2012.

[16] Henry Darcy. *Les fontaines publiques de la ville de Dijon: exposition et application...* Victor Dalmont, 1856.

[17] Filip de Clippel, Asim L. Khan, Angels Cano-Odena, Michiel Dusselier, Katrien Vanherck, Li Peng, Steffen Oswald, Lars Giebeler, Steven Corthals, Bart Kenens, Joeri F. M. Denayer, Pierre A. Jacobs, Ivo F. J. Vankelecom, and Bert F. Sels. CO 2 reverse selective mixed matrix membranes for H 2 purification by incorporation of carbonÃ??silica fillers. *J. Mater. Chem. A*, 1(3):945–953, 2013.

[18] Pablo G Debenedetti and Frank H Stillinger. Supercooled liquids and the glass transition. *Nature*, 410(6825):259–267, 2001.

[19] Peter Debye and Jerome Daen. Stability considerations on nonviscous jets exhibiting surface or body tension. *Physics of Fluids (1958-1988)*, 2(4):416–421, 1959.

[20] DI Dimitrov, A Milchev, and K Binder. Capillary rise in nanopores: molecular dynamics evidence for the lucas-washburn equation. *Physical review letters*, 99(5):054501, 2007.

[21] B. Diu. *Éléments de physique statistique*. Collection Enseignement des sciences. Hermann, 1989.

[22] Baojuan Dou, Qin Hu, Jinjun Li, Shizhang Qiao, and Zhengping Hao. Adsorption performance of VOCs in ordered mesoporous silicas with different pore structures and surface chemistry. *Journal of hazardous materials*, 186(2-3):1615–24, feb 2011.

[23] Jeppe C Dyre, Tina Hechsher, and Kristine Niss. A brief critique of the adam–gibbs entropy model. *Journal of Non-Crystalline Solids*, 355(10):624–627, 2009.

[24] E. Gedat, A. Schreiber, G. H. Findenegg, I. Shenderovich, H.-H. Limbach, and G. Buntkowsky. Stray field gradient NMR reveals effects of hydrogen bonding on diffusion coefficients of pyridine in mesoporous silica. *Magnetic Resonance in Chemistry*, 39(S1):S149–S157, dec 2001.

[25] Aziz Ghoufi, Ivanne Hureau, Denis Morineau, Richard Renou, and Anthony Szymczyk. Confinement of tert -Butanol Nanoclusters in Hydrophilic and Hydrophobic Silica Nanopores. *The Journal of Physical Chemistry C*, 117(29):15203–15212, jul 2013.

[26] Aziz Ghoufi, Ivanne Hureau, Denis Morineau, Richard Renou, and Anthony Szymczyk. Confinement of tert-butanol nanoclusters in hydrophilic and hydrophobic silica nanopores. *The Journal of Physical Chemistry C*, 117(29):15203–15212, 2013.

[27] LT Gibson. Mesosilica materials and organic pollutant adsorption: part a removal from air. *Chemical Society Reviews*, 43(15):5163–5172, 2014.

[28] Simon Gruener and Patrick Huber. Imbibition in mesoporous silica: rheological concepts and experiments on water and a liquid crystal. *Journal of Physics: Condensed Matter*, 23(18):184109, 2011.

[29] Simon Gruener, Zeinab Sadjadi, Helen E Hermes, Andriy V Kityk, Klaus Knorr, Stefan U Egelhaaf, Heiko Rieger, and Patrick Huber. Anomalous front broadening during spontaneous imbibition in a matrix with elongated pores. *Proceedings of the National Academy of Sciences of the United States of America*, 109(26):10245–50, jun 2012.

[30] Michael Grün, Iris Lauer, and Klaus K Unger. The synthesis of micrometer-and submicrometer-size spheres of ordered mesoporous oxide mcm-41. *Advanced Materials*, 9(3):254–257, 1997.

[31] Simon Alexander Grüner. Rheology and Dynamics of Simple and Complex Liquids in Mesoporous Matrices. 2010.

[32] Abdel Razzak Abdel Hamid. *Nanoségrégation d'un liquide binaire confiné dans des matériaux mésoporeux*. PhD thesis, Université Rennes 1, 2012.

[33] FK Hansen and G Rødsrud. Surface tension by pendant drop: I. a fast standard instrument using computer image analysis. *Journal of colloid and interface science*, 141(1):1–9, 1991.

[34] HZ Hassan, AA Mohamad, Y Alyousef, and HA Al-Ansary. A review on the equations of state for the working pairs used in adsorption cooling systems. *Renewable and Sustainable Energy Reviews*, 45:600–609, 2015.

[35] Terrell L Hill. Statistical mechanics of multimolecular adsorption. i. *The Journal of Chemical Physics*, 14(4):263–267, 1946.

[36] Patricia Horcajada, Christian Serre, María Vallet-Regí, Muriel Sebban, Francis Taulelle, and Gérard Férey. Metal–organic frameworks as efficient materials for drug delivery. *Angewandte chemie*, 118(36):6120–6124, 2006.

[37] P. Huber, S. Grüner, C. Schäfer, K. Knorr, and a. V. Kityk. Rheology of liquids in nanopores: A study on the capillary rise of water, n-Hexadecane and n-Tetracosane in mesoporous silica. *The European Physical Journal Special Topics*, 141(1):101–105, feb 2007.

[38] Patrick Huber. Soft matter in hard confinement: phase transition thermodynamics, structure, texture, diffusion and flow in nanoporous media. *Journal of Physics: Condensed Matter*, 27(10):103102, 2015.

[39] M Imperor-Clerc, P Davidson, and A Davidson. Existence of a microporous corona around the mesopores of silica-based sba-15 materials templated by triblock copolymers. *Journal of the American Chemical Society*, 122(48):11925–11933, 2000.

[40] Catheryn L Jackson and Gregory B McKenna. The melting behavior of organic materials confined in porous solids. *The Journal of Chemical Physics*, 93(12):9002–9011, 1990.

[41] Catheryn L Jackson and Gregory B McKenna. The glass transition of organic liquids confined to small pores. *Journal of Non-Crystalline Solids*, 131:221–224, 1991.

[42] Shinae Jun, Sang Hoon Joo, Ryong Ryoo, Michal Kruk, Mietek Jaroniec, Zheng Liu, Tetsu Ohsuna, and Osamu Terasaki. Synthesis of new, nanoporous carbon with hexagonally ordered mesostructure. *Journal of the American Chemical Society*, 122(43):10712–10713, 2000.

[43] Santanu Karan, Zhiwei Jiang, and Andrew G Livingston. MEMBRANE FILTRATION. Sub-10 nm polyamide nanofilms with ultrafast solvent transport for molecular separation. *Science (New York, N.Y.)*, 348(6241):1347–51, jun 2015.

[44] CT Kresge, ME Leonowicz, WJ Roth, JC Vartuli, JS Beck, et al. Ordered mesoporous molecular sieves synthesized by a liquid-crystal template mechanism. *nature*, 359(6397):710–712, 1992.

[45] Irving Langmuir. The adsorption of gases on plane surfaces of glass, mica and platinum. *Journal of the American Chemical society*, 40(9):1361–1403, 1918.

[46] Ronan Lefort, J-L Duvail, T Corre, Y Zhao, and Denis Morineau. Phase separation of a binary liquid in anodic aluminium oxide templates: a structural study by small angle neutron scattering. *The European physical journal. E, Soft matter*, 34(7):71, jul 2011.

[47] P Levitz, G Ehret, SK Sinha, and JM Drake. Porous vycor glass: The microstructure as probed by electron microscopy, direct energy transfer, small-angle scattering, and molecular adsorption. *The Journal of chemical physics*, 95(8):6151–6161, 1991.

[48] Ming Li, Erling Xu, Tingliang Wang, and Juan Liu. Adsorption equilibria of binary gas mixtures on graphitized carbon black. *Langmuir*, 28(5):2582–2588, 2012.

[49] Hong-Ping Lin and Chung-Yuan Mou. " tubules-within-a-tubule" hierarchical order of mesoporous molecular sieves in mcm-41. *Science*, 273(5276):765, 1996.

[50] Benedikt Lindlar, Andreas Kogelbauer, Patricia J Kooyman, and Roel Prins. Synthesis of large pore silica with a narrow pore size distribution. *Microporous and mesoporous materials*, 44:89–94, 2001.

[51] GQ Lu and Xiu Song Zhao. *Nanoporous materials: science and engineering*, volume 4. World Scientific, 2004.

[52] Richard Lucas. Ueber das zeitgesetz des kapillaren aufstiegs von flüssigkeiten. *Colloid & Polymer Science*, 23(1):15–22, 1918.

[53] M W Maddox, S L Sowers, K E Gubbins, and Olin Hall. Molecular Simulation of Binary Mixture Adsorption in Buckytubes and MCM-41. 32:23–32, 1996.

[54] Vicente Martínez-Soria, M. Pilar Peña, and Juan B. Montón. Vapor-Liquid Equilibria for the Binary Systems tert -Butyl Alcohol + Toluene, + Isooctane, and + Methylcyclohexane at 101.3 kPa. *Journal of Chemical & Engineering Data*, 44(1):148–151, 1999.

[55] Ramona Mhanna. *Confinement-induced of binary liquids with interactions.* PhD thesis, Université de Rennes 1, 2015.

[56] A.W. Mohammad, Y.H. Teow, W.L. Ang, Y.T. Chung, D.L. Oatley-Radcliffe, and N. Hilal. Nanofiltration membranes review: Recent advances and future prospects. *Desalination*, 356:226–254, nov 2014.

[57] Denis Morineau, Gilberte Dosseh, Christiane Alba-Simionesco, and Philip Llewellyn. Glass transition, freezing and melting of liquids confined in the mesoporous silicate MCM-41. *Philosophical Magazine Part B*, 79(11-12):1847–1855, aug 2009.

[58] Denis Morineau, Yongde Xia, and Christiane Alba-Simionesco. Finite-size and surface effects on the glass transition of liquid toluene confined in cylindrical mesopores. *The Journal of chemical physics*, 117(19):8966–8972, 2002.

[59] U Mueller, M Schubert, F Teich, H Puetter, K Schierle-Arndt, and J Pastre. Metal–organic frameworksâprospective industrial applications. *Journal of Materials Chemistry*, 16(7):626–636, 2006.

[60] M Pilar Pen, Juan B Monto, Departamento De Ingenieria Quimica, Facultad De Quimica, and Universitat De Valencia. Vapor - Liquid Equilibria for the Binary Systems tert -Butyl Alcohol + Toluene , + Isooctane , and + Methylcyclohexane at 101 . 3 kPa Vicente MartÃ? pages 148–151, 1999.

[61] Michel Perez. Gibbs–thomson effects in phase transformations. *Scripta materialia*, 52(8):709–712, 2005.

[62] B E Poling, J. M. Prausnitz, and J P O'Connell. Constants for the Antoine Equation for Vapour Pressures of Pure Species, 2001.

[63] Ryong Ryoo, Sang Hoon Joo, and Shinae Jun. Synthesis of highly ordered carbon molecular sieves via template-mediated structural transformation. *The Journal of Physical Chemistry B*, 103(37):7743–7746, 1999.

[64] Zeinab Sadjadi and Heiko Rieger. Scaling theory for spontaneous imbibition in random networks of elongated pores. *Physical review letters*, 110(14):144502, 2013.

[65] Peter Scheidler, Walter Kob, and Kurt Binder. The relaxation dynamics of a simple glass former confined in a pore. *EPL (Europhysics Letters)*, 52(3):277, 2000.

[66] Jan Swenson, Khalid Elamin, Helén Jansson, and Shigeharu Kittaka. Why is there no clear glass transition of confined water? *Chemical Physics*, 424:20–25, 2013.

[67] a Vyalikh, Th Emmler, E Gedat, I Shenderovich, G H Findenegg, H-H Limbach, and G Buntkowsky. Evidence of microphase separation in controlled pore glasses. *Solid state nuclear magnetic resonance*, 28(2-4):117–24, sep 2005.

[68] Yu Wang, Theodore T. Tsotsis, and Kristian Jessen. Competitive Sorption of Methane/Ethane Mixtures on Shale: Measurements and Modeling. *Industrial & Engineering Chemistry Research*, 54(48):12187–12195, dec 2015.

[69] J Warnock, DD Awschalom, and MW Shafer. Geometrical supercooling of liquids in porous glass. *Physical review letters*, 57(14):1753, 1986.

[70] Edward W Washburn. The dynamics of capillary flow. *Physical review*, 17(3):273, 1921.

[71] A Wittstock, V Zielasek, J Biener, C M Friend, and M Bäumer. Nanoporous gold catalysts for selective gas-phase oxidative coupling of methanol at low temperature. *Science (New York, N.Y.)*, 327(5963):319–22, jan 2010.

[72] Yahui Xue, Jürgen Markmann, Huiling Duan, Jörg Weissmüller, and Patrick Huber. Switchable imbibition in nanoporous gold. *Nature communications*, 5(May):4237, jan 2014.

[73] Omar M Yaghi, Michael O'Keeffe, Nathan W Ockwig, Hee K Chae, Mohamed Eddaoudi, and Jaheon Kim. Reticular synthesis and the design of new materials. *Nature*, 423(6941):705–714, 2003.

[74] Jeong-Ho Yun, Tina Düren, Frerich J Keil, and Nigel A Seaton. Adsorption of methane, ethane, and their binary mixtures on mcm-41: experimental evaluation of methods for the prediction of adsorption equilibrium. *Langmuir*, 18(7):2693–2701, 2002.

[75] Dongyuan Zhao, Jianglin Feng, Qisheng Huo, Nicholas Melosh, Glenn H Fredrickson, Bradley F Chmelka, and Galen D Stucky. Triblock copolymer syntheses of mesoporous silica with periodic 50 to 300 angstrom pores. *science*, 279(5350):548–552, 1998.

2

Nuclear Magnetic Resonance study of binary liquids in nanoconfinement

I Scientific background and motivation

In the introduction, the physical properties of TBA, TOL and their mixtures have been presented. Although completely miscible at the macroscopic scale, availability of the -OH group in TBA molecules is found to promote clustering of TBA molecules at the nanoscale via hydrogen-bonding interactions leading to structural changes by molecular association observed by neutron scattering and Raman spectroscopy as well as composition dependent changes in dynamics, as observed by nuclear magnetic resonance. Confining molecules in a spatial dimension in the nano-metre scale has been shown to influence structural and dynamic properties of molecules when compared to bulk[6,7,30]. We expect that in a nanoscale confinement, such hydrogen-bonding interactions in TBA molecules can lead to a modification of these mixture properties, which would also depend on the pore architecture and chemical nature of the nanoporous substrates. Nuclear Magnetic Resonance (NMR) being a local technique and highly versatile in being useful for both structural and dynamical characterisation of molecules[10,11,20,24] is the preferred choice of technique to analyze confinement induced effects.

Structural studies of confined molecules have been done previously by interpreting the position of ^{1}H NMR chemical shift of functional group(s) that belong to the molecule(s) being probed. The position of chemical shift and line shape of spectrum associated to it provides useful information of the electronic environment of the functional group, which in turn is directly associated to the local structure of the molecules and the specific interactions (H-bonding, Van der Waals...) it undergoes with the surrounding molecules[5,7]. ^{1}H Magic Angle Spinning NMR (MAS NMR) technique is of great utility in characterising molecules under nanoconfinement whose mobility is greatly reduced as it artificially induces a motion-averaging analogous to isotropic motion-averaging of molecules in liquid state, that enables obtaining precisely the chemical shifts of confined molecules.

One of the most popularly used technique for determining self-diffusion dynamics in nanoconfined systems is the Pulsed Field Gradient NMR (PFG NMR)[20,22,26]. The effects on self-diffusion dynamics under nanoconfinement have been shown to be influenced by the pore architecture and chemical environment of the host matrix[9,10,16,30]. Beyond single-component systems, NMR techniques have been used to investigate nanoconfined mixtures undergoing phase separation under particular conditions[29]. Using a combination of MAS NMR and PFG NMR can provide a wholesome knowledge and correlation of the structure and dynamics of nanoconfined systems[24].

As shown in the introduction, self-diffusion dynamics of TBA:TOL mixtures in bulk state were found to undergo a slowdown with increasing concentration of TBA. Confinement of these molecules in cylindrical pores a few molecular diameters wide is expected to curb the isotropic nature of diffusive motion and give more directional character to it. In the current chapter we use ^{1}H MAS NMR and PFG NMR techniques on TBA:TOL mixtures confined in silica nanoporous matrices, MCM-41 and SBA-15, to investigate the influence of H-bonding interactions amongst confined molecules and their possible inter-

action with the porous matrix driving nanostructuration and modification of dynamics of molecules compared to their bulk state.

II Fundamentals of NMR

Nuclear Magnetic Resonance (NMR) has proven to be an indispensable tool in spectroscopic characterization of materials, especially for organic molecules of hydrocarbon origin. Only magnetically active nuclei with non-zero nuclear spins could be utilized for nuclear magnetic resonance experiments, for example ^{1}H,^{13}C, ^{15}N, ^{19}F and ^{31}P. Every spinning nucleus is equivalent to a bar magnet possessing a magnetic moment oriented along the axis of spin. These magnetic moments generated by individual spins are randomly oriented in the absence of any external field. Upon application of an external magnetic field, the individual nuclear spins get aligned parallel or anti-parallel to the external field B_0 [8], which leads to a split of the nuclear spins into lower and higher energy states respectively, amongst which transitions can take place from lower to higher state and vice-versa. This energy difference between the two states depends on B_0 and is given by equation 2.1.

$$\Delta E = \frac{\gamma h B_0}{2\pi} = h\nu_0 \tag{2.1}$$

Where γ is called the gyromagnetic ratio, which is constant for each nucleus, h is the Planck's constant (6.626×10^{-34} J s) and ν_0 is called the Larmor frequency. For typical values of B_0 =2 to 9 T, ν_0 is in the radio-frequency (rf) range 50-1000MHz [19].

In a typical NMR experiment, a suitable sample, for example, a hydrocarbon compound is put inside a glass or quartz tube and is placed at the center of a superconducting magnet. As a consequence of the applied magnetic field, a splitting of nuclear spins occurs. The relative population distribution of spins between the two consecutive energy states is given by the Boltzmann distribution as follows [19].

$$\frac{N_{Higher}}{N_{Lower}} = \exp\frac{-\Delta E}{k_B T} \tag{2.2}$$

This difference results into a net magnetization $\vec{M}$ along $\vec{B_0}$. An alternating current passing through a coil of wire surrounding the sample is used to generate an rf pulse, whose magnetic field component B_{rf} lies in the plane perpendicular to the applied external field $\vec{B_0}$. $\vec{B_{rf}}$ thus oscillates with a frequency ν, same as that of the corresponding rf pulse. When the value of ν is same as ν_0, a resonance condition is met, some of the nuclear spins are flipped to a higher energy state $I = -\frac{1}{2}$, which causes the net magnetization $\vec{M}$ to flip from the direction $\vec{B_0}$. The component of $\vec{M}$ in the plane perpendicular to $\vec{B_0}$ generates an alternating current which is processed by a receiver to obtain an NMR signal which is Fourier transformed to get the NMR spectrum [23].

Two of the three most important nuclear spin interactions are, dipolar coupling between individual nuclear spins due to their individual magnetic fields and quadrupolar

interactions between nuclei of spin ≥ 1. The third and one which concerns us most in the context of current chapter is due to magnetic field induced by electron clouds surrounding a nucleus[25].The strength of NMR lies in its ability to distinguish the same nucleus which is being probed when present in different electronic environments. Indeed nuclei are surrounded by electrons, which generate an induced current, leading further to another magnetic field B_σ either opposing or augmenting B_0[19]. The net magnetic field thus acting on the nucleus changes to $B_{net} = B_0 + B_\sigma$ and since the strength of B_σ is proportional to B_0, we can rewrite B_{net} as $B_{net} = B_0(1 + \sigma)$, where σ is called the shielding or screening Constant. Thus the difference in chemical environment around each functional group leads to different values of σ, and consequently different resonance frequencies given by $\nu_0 = \frac{|\gamma|B_0(1-\sigma)}{2\pi}$, each unique and characteristic of a particular functional group giving rise to its respective peak in the NMR spectrum. In practice we express the NMR spectrum in a relative frequency scale, denoted by *Chemical shift* given by $\delta = \frac{\nu_0 - \nu_{ref}}{\nu_0} * 10^6$, where ν_{ref} is the NMR response a reference.

An important aspect to electronic shielding is the anistropy of electronic shielding caused due to presence of different functional groups. Orientation of such asymmetric electron cloud with respect to the B_0 could be different for individual molecules, leading to a range of chemical shifts. In liquids, the strong isotropic movement of molecules averages out this effect as well as dipolar-coupling interactions and there is one unique chemical shift for a certain functional group. In case of solids, due to the restricted mobility of molecules, we obtain a distribution of chemical shifts instead. This effect is known as chemical shift anisotropy. The combination of dipolar coupling and chemical shift anistropy leads to broadening of an NMR spectrum in solids as the molecules are strongly held in their positions. By confining liquids inside nanoscale geometries, a strongly restricted molecular mobility is induced similar to a solids. Thus, we explore an NMR technique specially suited to tackle such difficulties.

III ^{1}H Magic Angle Spinning NMR (1H MAS NMR) of TBA and TOL mixtures in nanoconfinement

A Motivation for the application of MAS NMR

Dipolar coupling and chemical shift anisotropy are second rank tensors that depend on the second order Legendre polynomial $3\cos^2\theta - 1$, where θ is the angle between a given axis of interaction and external magnetic field. These interactions vanish when the Legendre polynomial is equal to zero, i.e. $\theta = 54.73°$. This is known as the "magic angle".[18]

Orienting a solid state sample at magic angle with respect to external magnetic field and spinning at high frequencies (figure 2.1) averages out the dipolar coupling interactions and chemical shift anistropy to produce an effect analogous to isotropic averaging of nuclear spin interactions seen in liquids. This technique known as "Magic Angle Spinning"

(MAS) results in narrowing of the spectrum and increased resolution compared to static-state spectrum as shown in figure 2.2.

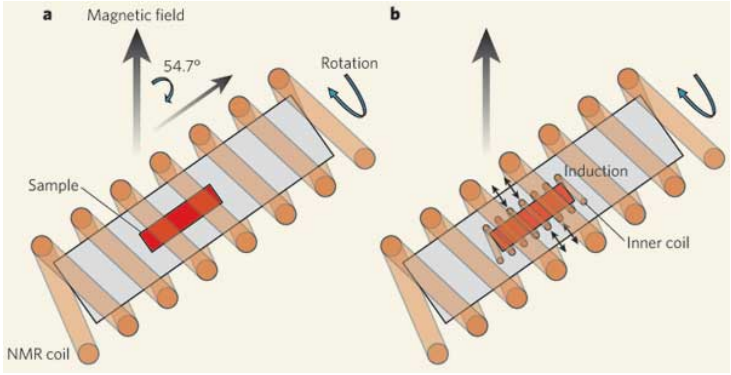

Figure 2.1: Orientation of the sample at "$MagicAngle$" = 54.7356^o[13]

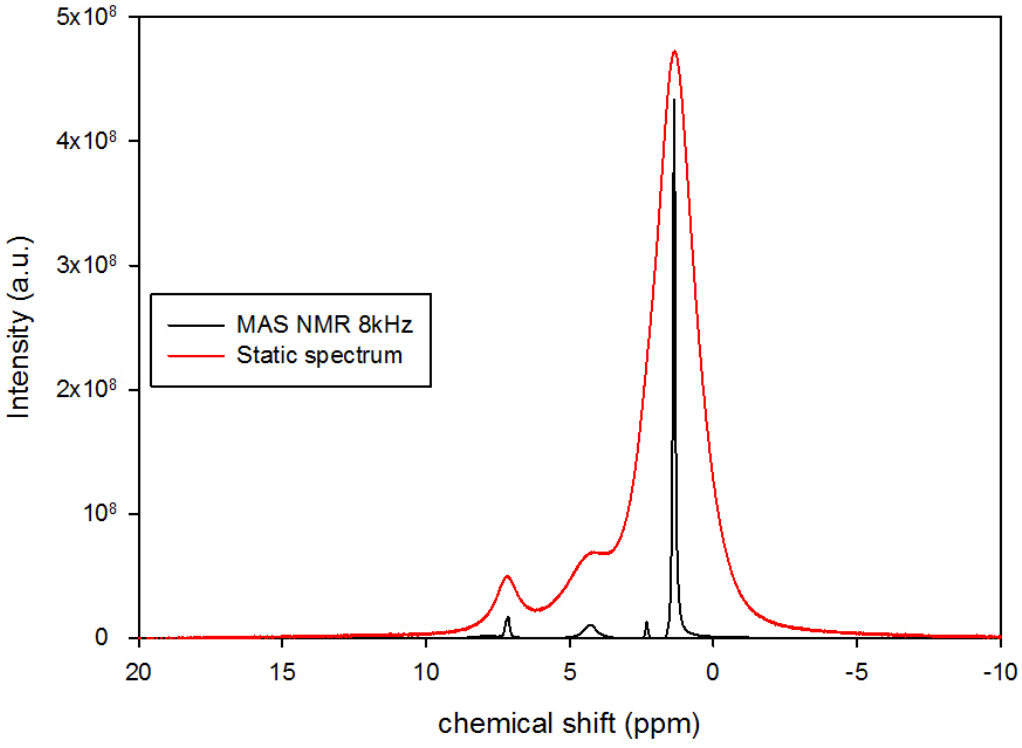

Figure 2.2: Comparison of NMR spectra of TBA:TOL mixture confined in MCM-41 under static condition (red line) and at Magic Angle Spinning (black line) ($\nu = 8\,\mathrm{kHz}$)

B Experiment

TOL and TBA were mixed in various volume ratios between $\%TBA = 0 - 100$. A cylindrical zirconium oxide sample holder with an internal diameter of 4 mm, fitted at the top with a cap made of high-strength polymer was used. This assembly of the cylindrical container and cap is called rotor. The rotor cap is designed with flaps which enable the entire rotor to be rotated at high frequencies using a combination of pressurized air streams in the solid-state probe of Bruker Avance I WB 300 MHz(7 T) NMR spectrometer. The rotor is maintained at "Magic Angle" inside the cavity of a device in the solid-state probe called stator as shown in figure 2.1.

MCM-41 powder was filled at 100% filling of its pores with TBA:TOL mixtures for any given concentration and packed inside the rotor tightly to be homogeneous along its length in order to have uniform rotation. ^{1}H NMR MAS experiments were carried out with a frequency of rotation of 8 kHz. Figure 2.3(a) shows the MAS NMR spectra of TBA:TOL mixtures of various compositions confined in MCM-41. In figure 2.3(b) the corresponding static spectra are shown. Clearly the high resolution obtained by MAS technique allows us to have a strong resolution of the four major peaks known from NMR measurements of bulk TBA:TOL mixtures.

In figure 2.3(a), recalling all the peaks once again, we have the methyl group from TBA at ≈1ppm, methyl group from TOL at ≈2ppm, phenyl ring of TOL at ≈7ppm, while the only peak to change its relative position is the -OH peak from TBA, which changes its position between 4.5-2.5ppm as the concentration of TBA decreases in the mixture.

In figure 2.4 we see the exact repetition of the MAS NMR spectrum, although vastly reduced in intensity, zoom of the region as shown in the inset shows exact same line shape. Position of each NMR line of this repeated spectrum is at same distance from its corresponding NMR line of the main MAS NMR spectrum. Such periodic repetition of the main spectrum is known as a spinning side-band which normally occur when the frequency of MAS is less than the frequency width of chemical shift anisotropy, which usually happens if the probed molecules have solid-like dynamics to some extent or due to inhomogeneity in the magnetic field experienced by the sample. MAS NMR experiments carried out by putting two teflon spacers in the sample holder (rotor), such that the filled MCM-41 powder was in centre of the rotors completely removed spinning sidebands and thus we can safely attribute the presence of spinning sidebands to inhomogeneities in magnetic field experienced by the sample.

Coming back to our main objective. In a series of experiments, the ^{1}H MAS NMR spectra(8 kHz) of TBA:TOL mixtures confined in MCM-41 were obtained and the change of $-OH$ chemical shift was noted for each mixture composition up to ≈ 2% TBA by volume. Solution-state NMR of the bulk mixtures were carried out as well over the same concentration range.

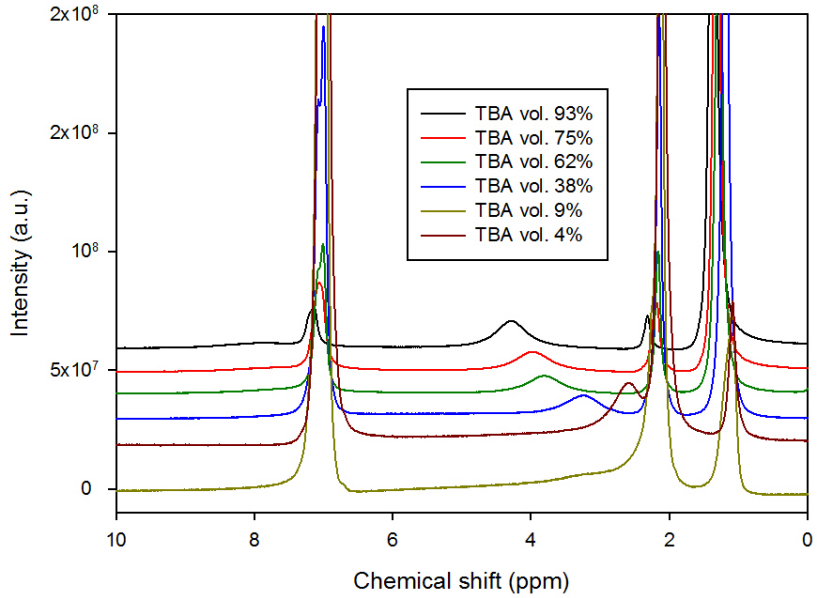

(a)

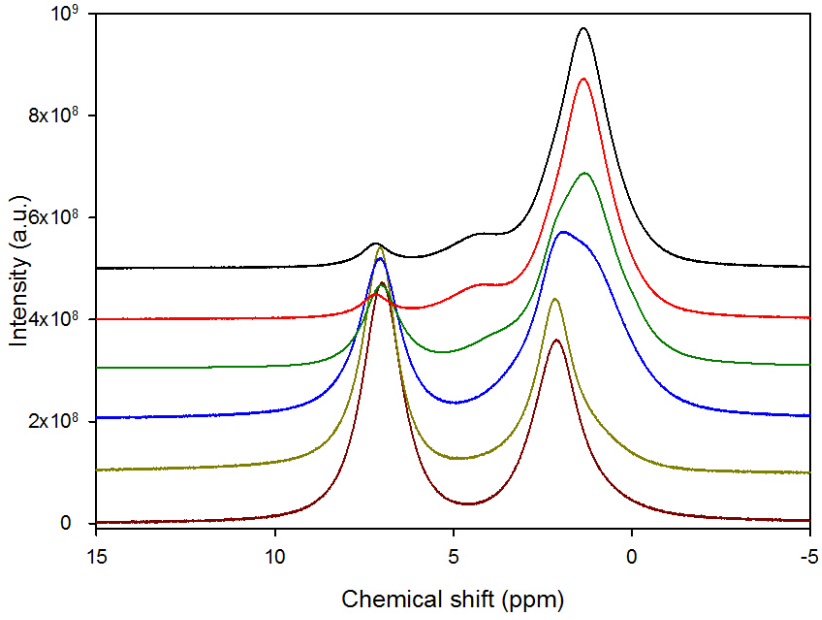

(b)

Figure 2.3: **(a)** ^{1}H MAS NMR spectra of TBA:TOL mixtures confined in MCM-41 at $\nu = 8\,\text{kHz}$. The lines TBA at ≈1ppm, ≈2ppm and ≈7ppm represent the methyl groups of TBA, TOL and phenyl group of TOL respectively, while the only peak to change its relative position is the -OH peak of TBA (4.5-2.5ppm)**(b)** Static solid state spectra for the corresponding mixture compositions.

C Results and discussion

Figure 2.5 shows the -OH chemical shift dependence on composition of TBA in MCM-41 filled with TBA:TOL solutions as well as bulk liquid mixtures. The $-OH$ chemical shift

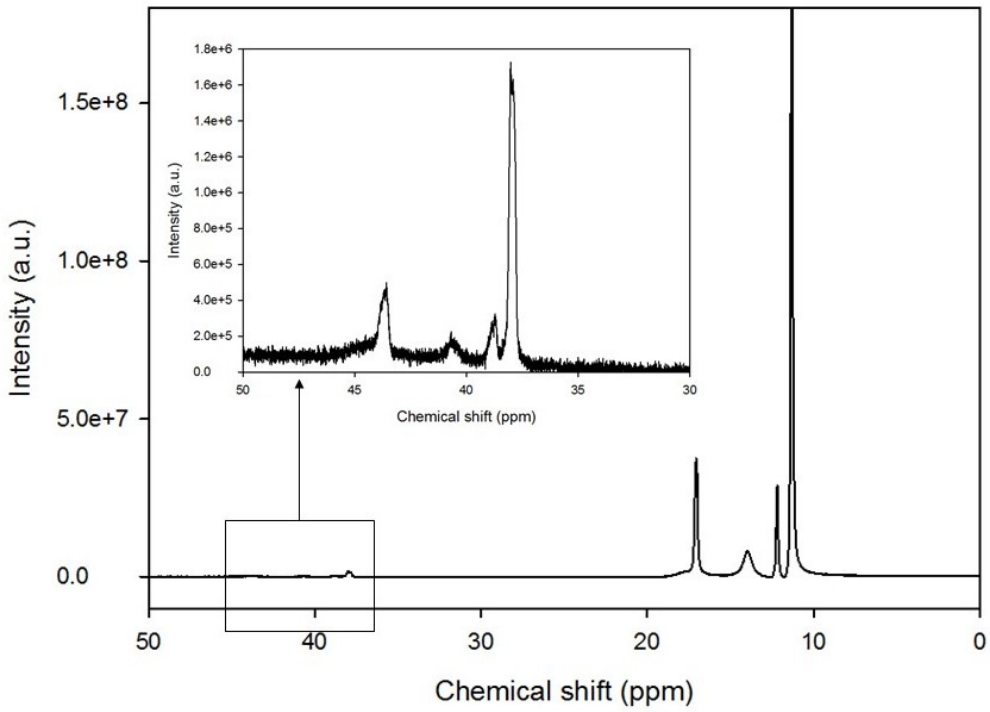

Figure 2.4: Presence of spinning sidebands observed in MAS NMR experiment of a TBA:TOL mixture confined in MCM-41. Inset zooms into the region. The exact line shape as main spectrum is observed.

decreases linearly with decreasing concentration of TBA in the solution as can be observed from the solid line in the figure. However this linear decrease is only up to 20% (TBA by vol.), beyond which there is a rapid decrease in the chemical shift to very small values as we go on diluting TBA further.

Comparing the chemical shift variation of bulk and confined TBA:TOL mixtures, a similar linear decrease of -OH chemical shift with respect to concentration of TBA is noticed up to $\approx 20\%$ TBA. Upon higher dilution of TBA we notice a much rapid decrease in the -OH chemical shift for bulk mixtures, which is associated to decrease in electronic shielding of the -OH with breakdown of TBA clusters as interpreted from Raman spectroscopy and ^{1}H NMR spectroscopy[1], as discussed previous in the introduction chapter. However the chemical shifts for confined mixtures are found to decrease linearly even at high dilution and a significant value of -OH chemical shift continues to persist even at negligible concentration of TBA ($\approx 2\%$).

Existence of such finite -OH chemical shift at high dilution indicates the persistence of electronic shielding on the -OH group due to presence of hydrogen-bonded structures, which could be either due to existed TBA clusters or specific interactions between TBA and MCM-41 pore wall due to their polar nature. The existence of TBA nanoclusters in TBA:TOL mixtures have been previously reported to exist even under nanoconfinement

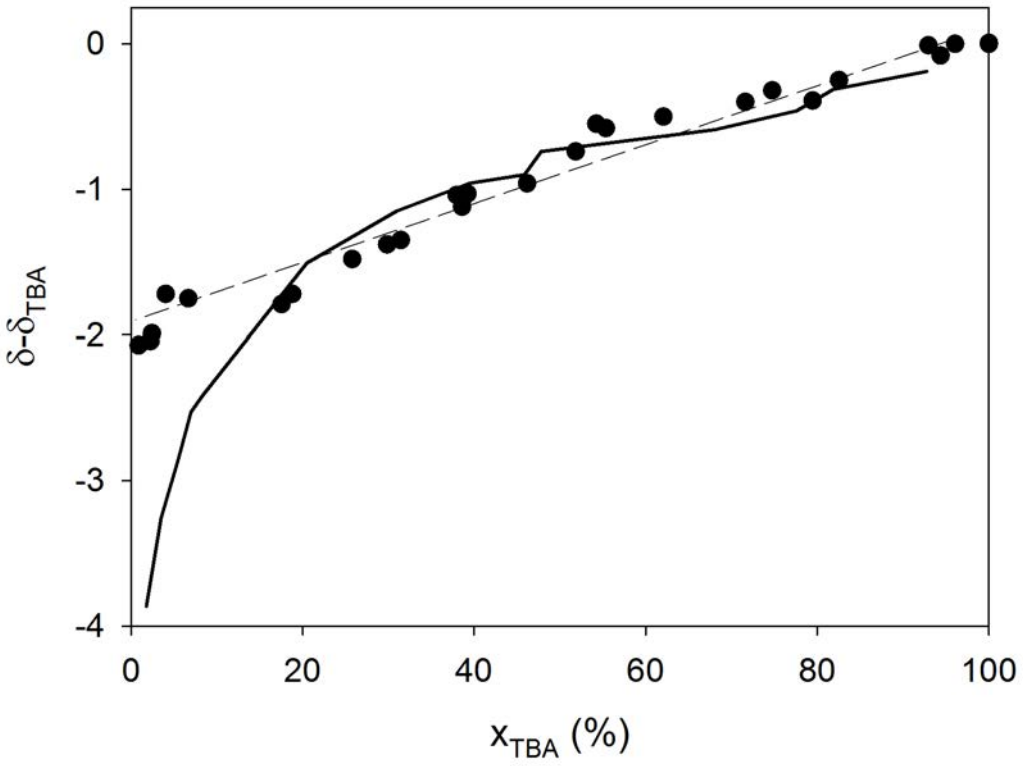

Figure 2.5: Change of -OH chemical shift as a function of % TBA for ^{1}H MAS NMR experiments (circles) for solutions confined in MCM-41 and solution-state NMR expeirments (solid line). The dashed line is a guide for the eye.

by a combination of neutron scattering and numerical simulations[15]. However, coming down to very high dilutions, the nanoclusters have been reported to break down in bulk state[1] and their existence under nanoconfinement as a result seems less likely. Then the remaining possibility is H-bonding interactions between TBA and the MCM-41 pore surface via -OH group in TBA and surface silanols in MCM-41. If this true, then we expect a confinement induced structuration as TBA molecules will show a tendency to separate out and attach to the pore walls. We expect such structuration of the confined mixture into difference phases to modify the dynamics when compared to bulk state. An issue which we attempt to understand in the following section.

IV Pulsed Field Gradient Stimulated Echo NMR (PFG-STE NMR)

A Brief description

The focus of this section is on the dynamic behaviour of our nanoconfined system, translational self-diffusion to be more precise, the fundamentals of which are well established. One of the most well known equations for self-diffusion of a molecule in a fluid is given by Stoke-Einstein relation (2.3)

$$D = \frac{k_B T}{6\pi\eta r_s} \tag{2.3}$$

Where D is the diffusion constant of the diffusing fluid molecule, k_B is the Botzmann Constant, T is temperature of the fluid, η is viscosity of the fluid and r_s is known as the Stoke's radius[22].

In an NMR experiment, upon application of a $\pi/2$ r.f pulse, the net magnetization is flipped in the plane perpendicular to external magnetic field B_0. As a consequence, individual nuclear spins spread out in this plane perpendicular to B_0, soon after which they attempt to realign. In this process, some spins travel faster than others and are leading, while the rest lag behind. Upon applying a π r.f pulse to the system, positions of individual spins are flipped by 180^o, such that the previously slower spins are now the leading ones and vice versa. Finally realignment of these spins give rise to a signal known as "spin echo".

However, applying a pulsed gradient of magnetic field parallel to B_0 shortly after application of the $\pi/2$ pulse modifies the net magnetic field acting on the nuclear spins. The effect of such spatial gradient of magnetic field is a loss of coherence between the spins. In a way each spin is coded according to the net magnetic field it experiences. After flipping the spins by 180^o using π r.f. pulse, the spin echo signal could only be obtained by reversing the effect of previously applied pulsed field gradient and gaining back phase coherence of the nuclear spins. Thus a gradient pulse of equal strength is applied, but in the opposite direction after the π pulse and with certain time delay Δ from the first pulse in order to restore the lost coherence. In this process however, owing to self-diffusion, some of the spins move away from their original positions and thus out of phase. Application of pulsed magnetic field gradients along z-axis change the effective field acting on the nuclear-spins, causing a phase-shift in the spins as give in equation 2.4.

$$\phi = \gamma g \delta z \tag{2.4}$$

Where ϕ, γ, and δ are the phase shift of the spins, gyromagnetic ratio of the probed nucleus and duration of the gradient pulse respectively and z is the distance travelled by a nuclear spin due to diffusion along the z-axis. The resulting echo signal thus undergoes a decay.Figure 2.6 shows the well known Stejskal and Tanner sequence[28] of PFG-NMR

experiment.

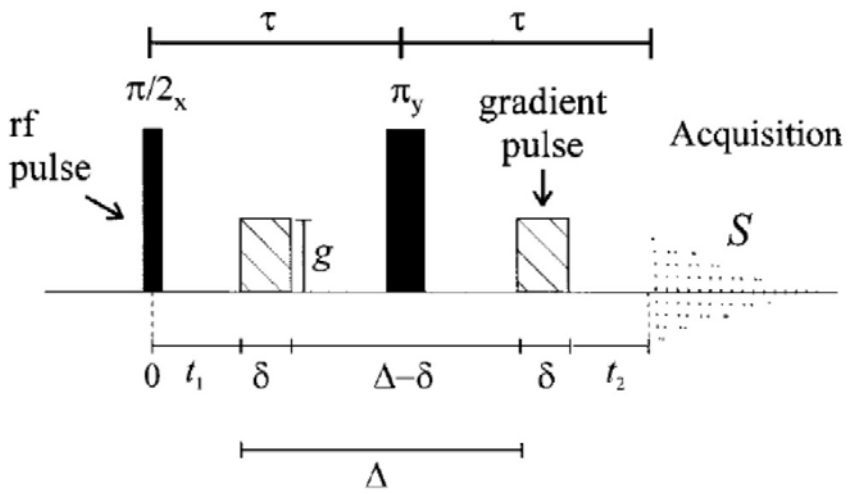

Figure 2.6: A typical Stejskal and Tanner sequence of PFG-STE NMR

In a typical PFG-STE NMR experiment, attentuation of the NMR echo signal is an exponential decay as given by the equation 2.5.

$$\Psi = \frac{I}{I_0} = \exp(-Dq^2\Delta) \tag{2.5}$$

Where D (m^2s^{-1}) is the translational diffusion coefficient of the diffusing species. However this equation is valid in its current form only in isotropic diffusion as in bulk liquids.

The translational self-diffusion coefficients of bulk TBA:TOL mixtures have been interpreted simply by equation 2.5 and reported by Abdel Razzak et al.[1] as discussed already in chapter 1. However the possibility of structural reorganization induced by extremely small geometries of confinement makes it interesting to investigate its consequence on the dynamics of confined TBA:TOL systems as we discuss in the following sections.

B Experiment

TBA:TOL mixtures of various concentrations were prepared and confined in two nanoporous silica powders, MCM-41 (ϕ=3.4 nm) and SBA-15 (ϕ=8 nm). The filled porous silica powder was put into 5 mm NMR tubes in a Diff60 diffusion probe, using a standard 3-pulses stimulated echo (STE) sequence as shown in figure 2.7. The pulsed field gradients were applied after the first and third $\pi/2$ r.f. pulse.[21]

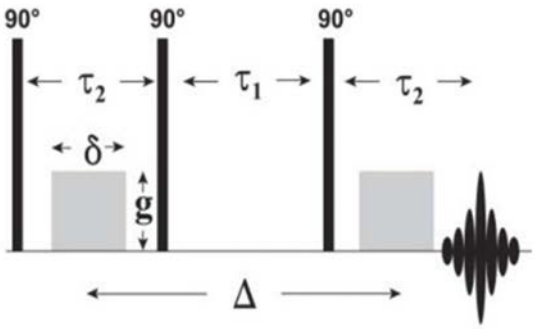

Figure 2.7: PFG-STE NMR sequence utilizing three $\frac{\pi}{2}$ pulses

MCM-41 powder was filled with TBA:TOL mixtures of various compositions inside NMR tubes and placed in the diffusion probe and probed by different Δ periods = 25, 50, 100, 150, 200ms respectively. For each Δ value, the value of the gradient field intensity was varied from 0-3000 ($\mathrm{Gcm^{-1}}$). The PFG-STE NMR sequence remains unchanged for SBA-15 filled with TBA:TOL mixtures in various concentrations. However the Δ values used were 5 and 20ms respectively. The strength of g used varied between 0-300 $\mathrm{Gcm^{-1}}$.

C Results and discussion

C.1 MCM-41

Figure 2.8 shows the attenuation of NMR signal of pure TOL as a function of q for different Δ mentioned in previous section, shown by various circles and triangles. Here $q = g\gamma\delta$ ($\mathrm{m^{-1}}$) is analogous to the scattering vector in diffraction experiments. g is the strength of pulsed field gradient, γ the gyromagnetic ratio of probed nucleus and δ the duration of gradient pulse respectively.

As we notice here, the attenuation of all the curves are roughly on top of each other irrespective of Δ. However from equation 2.5 we expect a strong Δ dependence in order to have an isotropic self-diffusion. From transmission electron microscopy we have a rough estimation of the pore-length for MCM-41 to be $\approx 1\,\mu\mathrm{m}$ which is about three orders of magnitude greater than its pore diameter which is known to be $\approx 3.4\,\mathrm{nm}$.Thus in the length-scale of a pore, molecular self-diffusion is chiefly anisotropic as has been previously reported for diffusion in silica nanopores.[27]. Equation gives the expression for attenuation of an anisotropic self-diffusion process.

$$\Psi(\delta g\gamma) = \frac{I}{I_0} = \frac{1}{2}\int_0^{\pi} \exp^{-(\gamma g\delta)^2\Delta(D_{para}\cos^2\theta + D_{perp}\sin^2\theta)} \sin\theta d\theta \tag{2.6}$$

The model of anisotropic diffusion does however include a coefficient of diffusion in the direction perpendicular to pore axis (D_{perp}), whose finite value has been attributed to diffusion through the pore walls or because of disorder in porous structure in the length scale

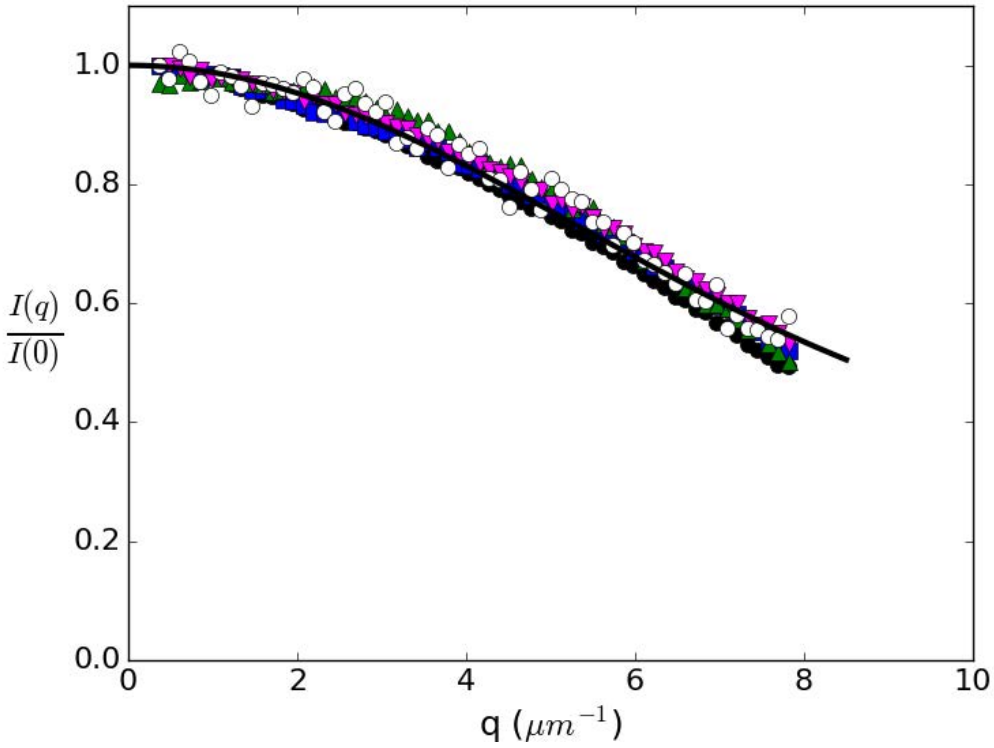

Figure 2.8: Fit of $\Psi = \frac{I(q)}{I_0}$ versus q(μm^{-1}) for attenuation curves from all Δ values

of experiment[27]. θ is the angle a diffusing molecule makes with the pore axis. Yohann Lechaux et al. calculated the attenuation of magnetization using the above equation for two cases, first, no diffusion perpendicular to the pore axis exists, i.e. $D_{perp} = 0$ and secondly with a finite value of diffusion perpendicular to pore axis such that $D_{perp} \neq 0$[21]. The author reports a strongly Δ dependent attenuation of magnetization irrespective of existence of any diffusive motion perpendicular to the pore axis or not, which is certainly not the case. Secondly, the attenuation curves were expected to either decay rather rapidly with q^2 and then plateau to a constant value in case $D_{perp} = 0$ or decay completely to zero in case of $D_{perp} \neq 0$ within the range of q values used in the experiment.

Since none of the above conditions are fulfilled by the experimental points, we find the model of unrestricted anisotropic diffusion not suitable for interpretation of the attenuation. Keeping in mind that the length of pore is in fact of finite length, a model for anisotropic restricted diffusion between two parallel planes given in equation 2.7 has been tested.

$$\Psi(q,\Delta) = \frac{2[1-\cos(2\pi qL)]}{(2\pi qL)^2} + 4(2\pi qL)^2 \sum_{n=1}^{\infty} \exp\left(\frac{-n^2\pi^2 D\Delta}{L^2}\right) \frac{1-(-1)^n\cos(2\pi qL)}{[(2\pi qL)^2-(n\pi)^2]} \quad (2.7)$$

Where L is the length of pore. $q = g\gamma\delta$ is the scattering vector parallel to the pore-axis. Thus varying the strength of g from low to high values is equivalent to probing diffusive

motions from low to high q values, in other words from a longer to smaller length scale, in the time period Δ. In figure 2.8, we see that the magnetization even at very high gradient strength (high q) decays only up to $\approx 50\%$ of it's original value.It is important to note that the signal attenuation given by equation 2.7 is Δ dependent as it is a sum of two terms, one of which varies with Δ. However the experimental attenuation curves are Δ-independent. This condition could be fulfilled only if the Δ dependent term in equation 2.7 is negligible, i.e.

$$4(2\pi qL)^2 \sum_{n=1}^{\infty} \exp\left(\frac{-n^2\pi^2 D\Delta}{L^2}\right) \frac{1-(-1)^n \cos(2\pi qL)}{[(2\pi qL)^2 - (n\pi)^2]} \approx 0$$

Which is possible when $D >> \dfrac{L^2}{\Delta\pi^2}$.
The experimental points of attenuation are thus fitted with the remaining term of equation 2.7, which depends on the length of pore L, shown by a solid black line in figure 2.8. The result of the fit gives $L = 0.65\,\mu\text{m}$.
Using this value of L, we have $D \gg 2 \times 10^{-12}\,\text{m}^2\,\text{s}^{-1}$. The diffusion under confinement could not be three orders of magnitude slower than bulk-like diffusion ($2 \times 10^{-9}\,\text{m}^2\,\text{s}^{-1}$). The mean square displacement of a molecule is related to the diffusion constant as

$$\langle u^2 \rangle = 2\Delta D$$

Thus if $L^2 << \Delta D$, i.e. the mean square displacement is much larger than length of pore, it suggests that even with very small Δ values that could be achieved experimentally (order of milliseconds), the self-diffusion of TOL is fast enough ($\gg 2 \times 10^{-12}\,\text{m}^2\,\text{s}^{-1}$), such that in the time scale of Δ, TOL molecules traverse a path much greater than length of the pore, i.e. several times along the length of pore.

Thus, owing to technical limitations, i.e., small pore length of MCM-41 and minimum possible value of δ in milliseconds range, determination of the translational diffusion coefficient of liquids under confinement was not possible. However it helped provide complementary information on the pore-architecture by giving the value of pore length (L). Unintended though, this is an essential information on the architecture of the host matrix used. To overcome the structural limitation (small pore length) in determination of D, the possible solution is the use of a porous matrix with pore length long enough to determine D in typical Δ time scales. Thus, SBA-15 owing to its longer pore size was considered to be a more prospective host matrix, experiments on which are discussed in the following section.

C.2 SBA-15

The diameter of typical SBA-15 pores is 8 nm, which is more than twice that of MCM-41 (3.4 nm). Thus the pore diameter of SBA-15 is large enough to accommodate 8-9 molecular layers compared to about 4 molecular layers in MCM-41. This increased size of spatial confinement eases the restrictions on molecular motion. With the additional property of corrugated pore-structure, we expect self-diffusion dynamics in SBA-15 to be different compared to MCM-41.

Just like MCM-41, SBA-15 nanopores also have pore lengths about three orders of magnitude larger than their pore diameter, promoting 1D molecular self-diffusion. Figure 2.9 shows the attenuation of NMR signal versus q^2 corresponding to the phenyl ring in TOL. i.e. TOL diffusion is being investigated for TBA:TOL compositions ranging from $\%TBA = 6\%$ to $\%TBA = 90\%$ for two different values of $\Delta = 5\,\text{ms}$ and $\Delta = 20\,\text{ms}$ shown in coloured circles and triangles respectively. The smaller T_2 (transverse) relaxation time for SBA-15 $T_2^{SBA} = 1.998\,\text{ms}$ compared to that of MCM-41,$T_2^{MCM} = 4.3\,\text{ms}$, prevents using greater Δ values for the experiment.

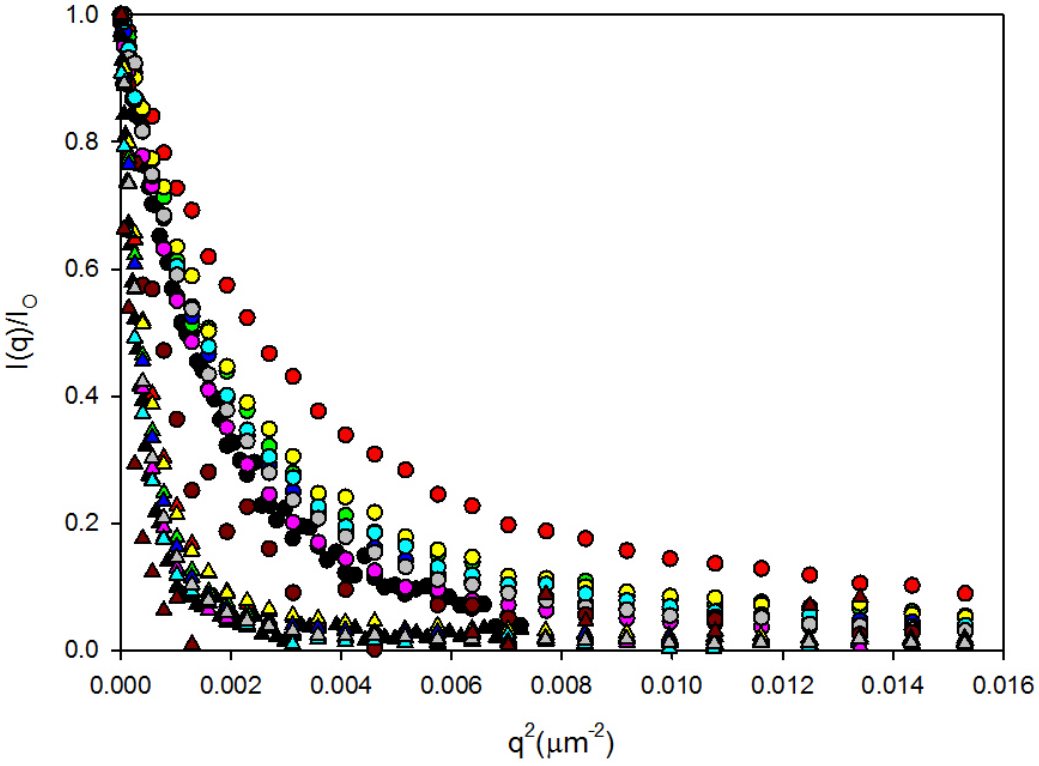

Figure 2.9: Attenuation of magnetization Ψ as a function of $q^2(\mu\text{m}^{-2})$ for different compositions of TBA:TOL mixtures at $\Delta = 5\,\text{ms}$ (coloured circles) and $\Delta = 20\,\text{ms}$ (coloured triangles) respectively.

The magnetization in SBA-15 decayed rapidly close to zero at very low q^2 values for both the Δ values used. A Δ-dependent attenuation is observed which decays fast at low q^2 values and approaches close to zero. Some degree of concentration dependence is observed between individual curves, although qualitatively we observe it to be non-linear. Since the attenuation in magnetization is related to the diffusion coefficient, such non-linear and small concentration-dependence of individual curves are in strong deviation from TOL diffusion coefficients in bulk mixtures which decrease steadily with decreasing TOL concentration as discussed in introduction chapter.These observations are completely different from that observed in MCM41. The fact that we observe a full decay of the at-

tenuation curves seems to indicate an unrestricted diffusion instead.

We know that SBA-15 pore length just like in MCM-41 surpasses its pore diameter (8 nm) by three orders of magnitude, an anisotropic diffusion model with restricted pore-length (equation 2.7) was tested keeping the length of pore and diffusion coefficient parallel to pore axis (D_{para}) as free parameters. The range of $D_{para} = 10^{-7}\,\mathrm{m^2/s}$ to $10^{-12}\,\mathrm{m^2/s}$ and length of pore from 1 to 100 µm were used. Figure 2.10 shows the plot of $I(q)/I_0$) versus $q^2\Delta$ for 40:60 TBA:TOL mixture composition by %volume for $\Delta = 5\,\mathrm{ms}$ and $\Delta = 20\,\mathrm{ms}$, both shown in black crosses. The closest possible fit for the curves were obtained for $D_{para} = 8 \times 10^{-8}\,\mathrm{m^2/s}$ and $L = 50\,\mu\mathrm{m}$. We observe that the attenuation for experimental points is much more rapid than predicted by the model of anisotropic diffusion in restricted pore length.

Thus the above model is found to be incompatible with experimental curves. One pos-

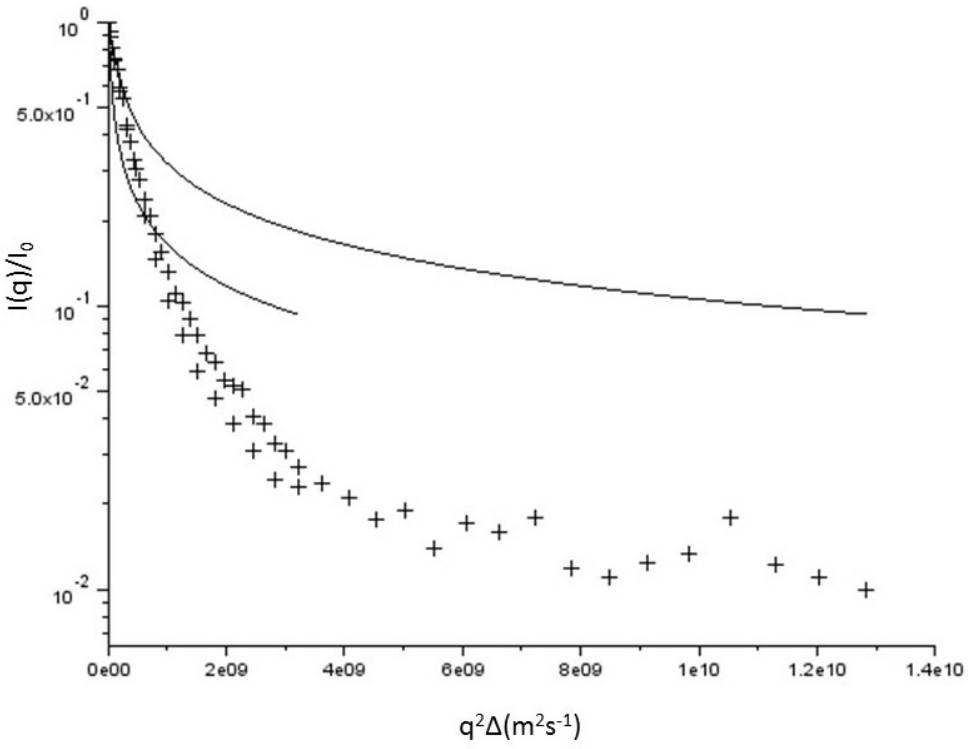

Figure 2.10: Attenuation of magnetization for 5 and 20 ms shown by crosses. Solid black lines are calculated curves of anisotropic self-diffusion in restricted pore-length along pore axis.

sibility of such an occurrence might be due to much greater length of SBA-15 pores than MCM-41, such that in the time scale of experiment the pore-length appears as infinitely long. If this is the case, then application of unrestricted anisotropic diffusion seems more apt. Recalling equation 2.6, by removing the perpendicular component of diffusion coefficient, we simply reduce equation 2.6 to the following expression.

$$\Psi(\delta, g, \Delta) = \frac{\sqrt{\pi}}{2\sqrt{D_{para}\Delta q}} erf(\sqrt{D_{para}\Delta q}) \tag{2.8}$$

Figure 2.11 shows the plot of experimental $I(q)/I_0$ versus q^2 curves of a $\%TBA = 40$ mixture for the different Δ values (circles) and the fit of curves (solid lines) using equation 2.8. We notice that only experimental points of $\Delta = 20\,\text{ms}$ could be fitted, the best fit of which was obtained for $D_{para} = 2 \times 10^{-8}\,\text{m}^2/\text{s}$. This value is an order of magnitude faster than TOL diffusion in the corresponding bulk mixture ($D_{TOL}^{40TBA} \approx 1.7 \times 10^{-9}\,\text{m}^2/\text{s}$) and is incompatible with the experimental points at $\Delta = 5\,\text{ms}$. A faster than bulk diffusion might have been interesting for interpretation has it been valid over both Δ values. Considering the rapid decay of attenuation followed by a much slower decay at higher q values, the interpretation of experimental points by a single unique diffusion coefficient might not be the most ideal option.

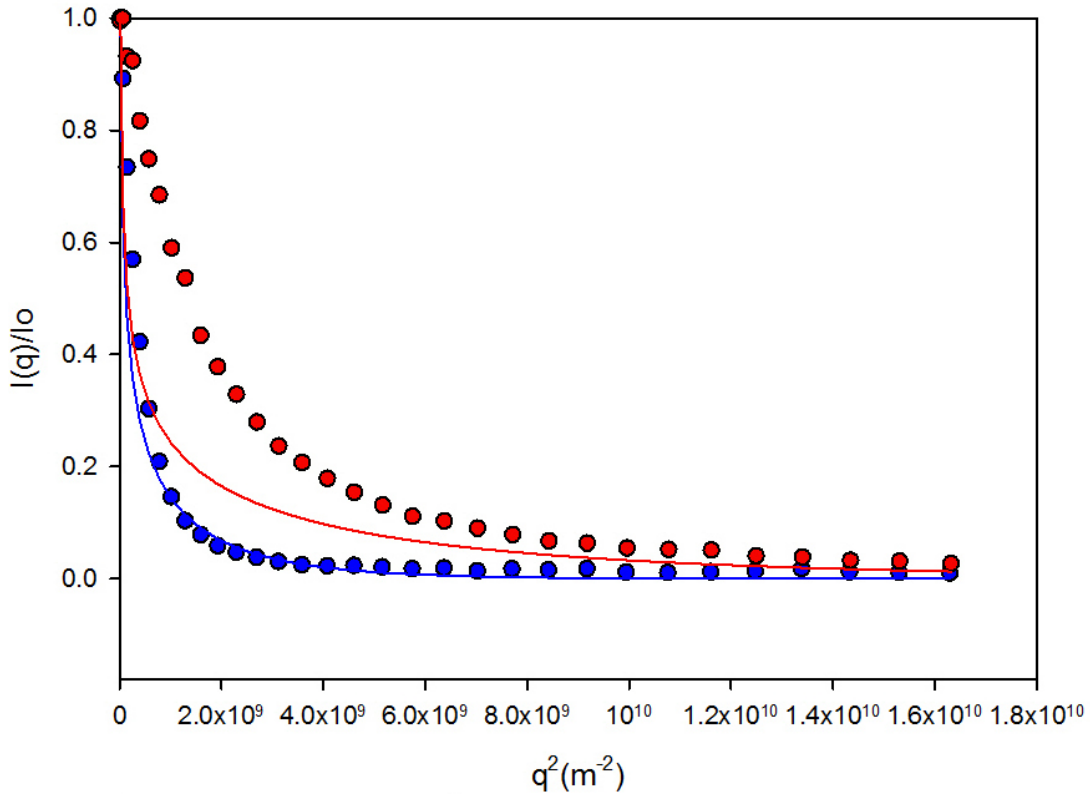

Figure 2.11: Experimental points for attenuation of $\%TBA = 40$ mixture at $\Delta = 5\,\text{ms}$ (red circles) and $\Delta = 20\,\text{ms}$ (blue circles) respectively. The solid lines (red and blue) show the best fit of experiments for an anistropic self-diffusion model restricted between two planes and only parallel to the pore axis (equation 2.8).

We can as well visualize the attenuation curve to represent two different populations, each with separate isotropic self-diffusion dynamics. Thus the attenuation for such double-component diffusion can be written as a double exponential as shown in the fol-

lowing equation.

$$\frac{I(q)}{I_0} = Ae^{-q^2 D_1 \Delta} + Be^{-q^2 D_2 \Delta} \tag{2.9}$$

Where D_1 and D_2 are the diffusion coefficients at the fast and slow diffusion regions respectively (low and high q respectively). A and B are constants. Figure 2.12 shows the plot of experimental points for attenuation of $\%TBA = 40$ mixture at 5 and 20 ms by red and blue circles respectively. The solid lines represent best fit of the curves using equation 2.9.

The result of fit gives $D_1^{5ms} = 1.3 \times 10^{-7}\,\mathrm{m^2/s} \pm 0.2$ and $D_2^{5ms} = 2.4 \times 10^{-8}\,\mathrm{m^2/s} \pm 0.2$

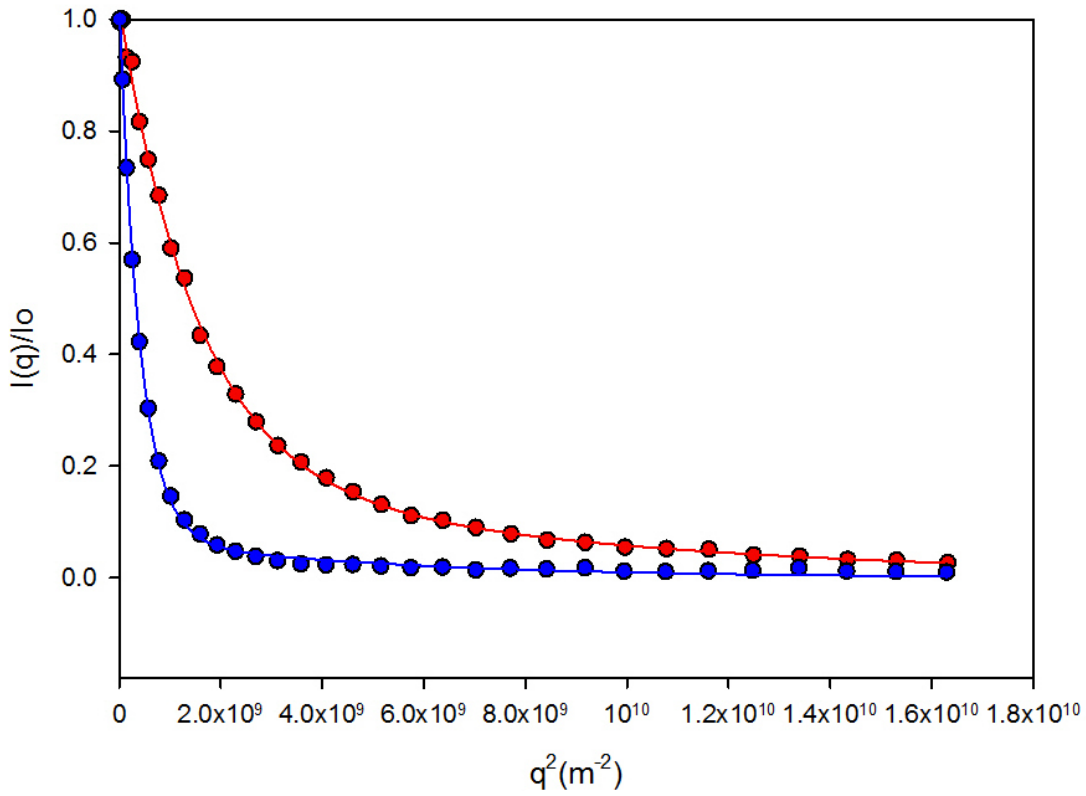

Figure 2.12: Experimental points for attenuation of $\%TBA = 40$ mixture at $\Delta = 5$ ms (red circles) and $\Delta = 20$ ms (blue circles) respectively. The solid lines (red and blue) show the best fit of experiments for a two-component diffusion model (equation 2.8).

for $\Delta = 5$ ms and $D_1^{20ms} = 1.22 \times 10^{-7}\,\mathrm{m^2/s} \pm 0.2$ and $D_2^{20ms} = 9.8 \times 10^{-9}\,\mathrm{m^2/s} \pm 0.2$ for $\Delta = 20$ ms, while the values of constants are $A^{5ms} = 0.83 \pm 0.03$, $B^{5ms} = 0.18 \pm 0.03$ and $A^{20ms} = 0.95 \pm 0.01$, $B^{20ms} = 0.07 \pm 0.01$. The values of A and B suggest that majority of dynamics belongs to very fast diffusive motions, $> 80\%$ at $\Delta = 5$ ms and $> 90\%$ at $\Delta = 20$ ms, that is two-orders of magnitude faster than bulk self-diffusion constant of TOL. On the other hand, the slower component which made up $\leq 18\%$ and $\leq 7\%$ of the signal for $\Delta = 5$ ms and $\Delta = 20$ ms is found to be an order of magnitude faster than TOL

diffusion in bulk mixture for the former, while about the same as bulk for the latter. One thing quite clear here is that most of the observed attenuation corresponds to very fast dynamics which might be due to fast exchange of molecules between the confined liquid and surrounding vapour phase. This is consistent for both values of Δ used. On the other hand, the D_2 diffusion coefficients though not in equally good agreement tend to be closer to bulk-like diffusion.

Finally, the diffusive dynamics of molecules in the binary mixture confined in SBA-15 materials is found to be very different, at least at first glance, from the one observed in the smaller pores of MCM-41 molecular sieves. Qualitatively, the observed dynamics appears unrestricted and much faster than expected. The analysis of the dataset that could be recorded within our experimental limitations did dot provide up to now a clear quantitative view on the translational molecular dynamics. In order to get deeper understanding of this system, measurements at both shorter and longer Δ values would be necessary, but are unfortunately unaccessible experimentally because of the unfavorable spin relaxation properties of the confined liquid.

V Conclusion

The general trend of lowering of -OH chemical shift upon dilution of TBA is similar under bulk and in confinement up to 20% TBA by vol. in mixtures, while its persistence to significant values upon high dilution of TBA under confinement is in strong contrast to the rapid decrease in its value to nearly zero in bulk liquid mixtures. In spite of the evidence for existence of TBA nanoclusters in confinement, their persistence at high dilutions is less likely even in bulk mixtures. These specific interactions between -OH group from TBA and silanol groups on MCM-41 pore surface, which might give rise to a new hydrogen-bonded network. If this is true, then MCM-41's surface selective nature towards TBA might drive a confinement induced nano-segregation process of molecules, leading to a richer concentration of TBA at pore surface.

The possible effect of a nanosegragation on self-diffusion dynamics was studied for confinement of TBA:TOL mixtures in MCM-41 and SBA-15. A Δ independent nature of attenuation was observed in case of MCM-41. This was interpreted in terms of fast molecular motions, with a mean-square displacement exceeding the pore length found to be close to 0.65 µm.

The diffusion dynamics in SBA-15 though expected to be characteristic of an anisotropic diffusion, were rather found to be two-component in nature, although this interpretation still needs to be confirmed. Composed mostly of a very fast diffusing component, with diffusion coefficient two-order of magnitude larger than TOL molecules in bulk TBA:TOL mixture of the same composition. Such fast diffusive motion could be associated to fast exchange of molecules between confined molecules and surrounding vapour phase of TBA and TOL molecules. The slower component was closer to a bulk-like diffusion and depending on the Δ time used to probe, was found to be faster or slower than bulk.

Bibliography

[1] Abdel Hamid, A. R., Lefort, R., Lechaux, Y., Moreac, A., Ghoufi, A., Alba-Simionesco, C., and D, M. Solvation Effects on Self-Association and Segregation Processes in tert -Butanol and Aprotic Solvent Binary Mixtures. *Journal of Physical Chemistry B 117* (2013), 10221–10230.

[2] Adem, Z., Guenneau, F., Springuel-Huet, M.-A., Gédéon, A., Iapichella, J., Cacciaguerra, T., and Galarneau, A. Diffusion Properties of Hexane in Pseudomorphic MCM-41 Mesoporous Silicas Explored by Pulsed Field Gradient NMR. *The Journal of Physical Chemistry C 116*, 25 (jun 2012), 13749–13759.

[3] Aksnes, D. W., Førland, K., and Stöcker, M. 1H NMR relaxation and diffusion studies of cyclohexane and cyclopentane confined in MCM-41. *Microporous and Mesoporous Materials 77*, 1 (jan 2005), 79–87.

[4] Aksnes, D. W., and Gjerda, L. NMR line width , relaxation and diffusion studies of cyclohexane confined in porous silica. 27–34.

[5] Azaïs, T., Tourné-Péteilh, C., Aussenac, F., Baccile, N., Coelho, C., Devoisselle, J.-M., and Babonneau, F. Solid-State NMR Study of Ibuprofen Confined in MCM-41 Material. *Chemistry of Materials 18*, 26 (dec 2006), 6382–6390.

[6] Babonneau, F., Yeung, L., Steunou, N., Gervais, C., Ramila, A., and Vallet-Regi, M. Solid State NMR Characterisation of Encapsulated Molecules in Mesoporous Silica. *Journal of Sol-Gel Science and Technology 31*, 1-3 (aug 2004), 219–223.

[7] Buntkowsky, G., Breitzke, H., Adamczyk, A., Roelofs, F., Emmler, T., Gedat, E., Grünberg, B., Xu, Y., Limbach, H.-H., Shenderovich, I., Vyalikh, A., and Findenegg, G. Structural and dynamical properties of guest molecules confined in mesoporous silica materials revealed by NMR. *Physical chemistry chemical physics : PCCP 9*, 35 (sep 2007), 4843–53.

[8] Canet, D., Canet, E., and Boubel, J.-C. La rmn: concepts, møthodes et applications.

[9] Courivaud, F., Hansen, E., Karlsson, A., Kolboe, S., and Stöcker, M. Pulsed field gradient NMR study of the diffusion of n-hexane confined in hydroxylated and dehydroxylated MCM-41 of various pore diameters. *Microporous and Mesoporous Materials 35-36* (apr 2000), 327–339.

[10] Courivaud, F., Hansen, E., Kolboe, S., Karlsson, A., and Stöcker, M. Enhanced n-hexane diffusion in partially filled MCM-41 of different surface hydrophobicity probed by NMR. *Microporous and Mesoporous Materials 37*, 1-2 (may 2000), 223–232.

[11] Dubbeldam, D., and Snurr, R. Q. Recent developments in the molecular modeling of diffusion in nanoporous materials. *Molecular Simulation 33*, 4-5 (apr 2007), 305–325.

[12] Dvoyashkin, M., Khokhlov, A., Naumov, S., and Valiullin, R. Pulsed field gradient NMR study of surface diffusion in mesoporous adsorbents. *Microporous and Mesoporous Materials 125*, 1-2 (oct 2009), 58–62.

[13] Edison, A. S., and Long, J. R. Spectroscopy: The magic of solenoids. *Nature 447*, 7145 (2007), 646–647.

[14] Gedat, E., Schreiber, A., Findenegg, G. H., Shenderovich, I., Limbach, H.-H., and Buntkowsky, G. Stray field gradient NMR reveals effects of hydrogen bonding on diffusion coefficients of pyridine in mesoporous silica. *Magnetic Resonance in Chemistry 39*, S1 (dec 2001), S149–S157.

[15] Ghoufi, A., Hureau, I., Morineau, D., Renou, R., and Szymczyk, A. Confinement of tert-butanol nanoclusters in hydrophilic and hydrophobic silica nanopores. *The Journal of Physical Chemistry C 117*, 29 (2013), 15203–15212.

[16] Gjerdåker, L., Aksnes, D. W., Sørland, G. H., and Stöcker, M. Relaxation and diffusion studies of cyclohexane confined in MCM-41 by NMR. *Microporous and Mesoporous Materials 42*, 1 (jan 2001), 89–96.

[17] Hamid, A. R. A. *Nanoségrégation d'un liquide binaire confiné dans des matériaux mésoporeux*. PhD thesis, Université Rennes 1, 2012.

[18] Hennel, J. W., and Klinowski, J. Magic-Angle Spinning : a Historical Perspective. 1–14.

[19] Hore, P. *Nuclear magnetic resonance*. Oxford University Press, 2015.

[20] Kärger, J., Stallmach, F., and Vasenkov, S. Structure-mobility relations of molecular diffusion in nanoporous materials. *Magnetic Resonance Imaging 21*, 3-4 (apr 2003), 185–191.

[21] Lechaux, Y. Etude experimentale de la dynamique de liquides nanoconfines. Master thesis, Institut de Physique de Rennes, Université de Rennes 1, Institut de Physique de Rennes UMR CNRS 6251 Bat. 11 A, B, C, D, E 263 Avenue du Général Leclerc 35042 Rennes CEDEX France Tél : 02 23 23 52 92, 2013. Nom du responsable : M. Lefort Ronan Maître de conférences Tel : 02 23 23 69 07 ronan.lefort@univ-rennes1.fr.

[22] Price, W. S. Pulsed-field gradient nuclear magnetic resonance as a tool for studying translational diffusion: Part 1. basic theory. *Concepts in magnetic resonance 9*, 5 (1997), 299–336.

[23] Roberts, J. Nuclear magnetic resonance. *J. Am. Chem. Soc 80* (1958), 501.

[24] Romanova, E. E., Grinberg, F., Pampel, A., Kärger, J., and Freude, D. Diffusion studies in confined nematic liquid crystals by MAS PFG NMR. *Journal of magnetic resonance (San Diego, Calif. : 1997) 196*, 2 (feb 2009), 110–4.

[25] Shaw, D. Fourier transform nmr spectroscopy. 2.

[26] Stallmach, F., Gräser, A., Kärger, J., Krause, C., Jeschke, M., Oberhagemann, U., and Spange, S. Pulsed field gradient NMR studies of diffusion in MCM-41 mesoporous solids. *Microporous and Mesoporous Materials 44-45* (apr 2001), 745–753.

[27] Stallmach, F., Kärger, J., Krause, C., Jeschke, M., and Oberhagemann, U. Evidence of Anisotropic Self-Diffusion of Guest Molecules in Nanoporous Materials of MCM-41 Type. *Journal of the American Chemical Society 122*, 38 (sep 2000), 9237–9242.

[28] Stejskal, E. O., and Tanner, J. E. Spin diffusion measurements: spin echoes in the presence of a time-dependent field gradient. *The journal of chemical physics 42*, 1 (1965), 288–292.

[29] Valiullin, R., Kortunov, P., Körger, J., and Timoshenko, V. Concentration-dependent self-diffusion of liquids in nanopores: a nuclear magnetic resonance study. *The Journal of chemical physics 120*, 24 (jun 2004), 11804–14.

[30] Vyalikh, a., Emmler, T., Gedat, E., Shenderovich, I., Findenegg, G. H., Limbach, H.-H., and Buntkowsky, G. Evidence of microphase separation in controlled pore glasses. *Solid state nuclear magnetic resonance 28*, 2-4 (sep 2005), 117–24.

3

Dynamic vapour sorption study of binary gas adsorption in nanopores

I Scientific background and motivation

In the previous chapter with the help of a ^{1}H MAS NMR chemical shift study we found evidence for persistence of a hydrogen-bonded network in TBA:TOL mixtures confined in MCM-41 nanopores even at high TBA dilutions. Hydrogen-bonded network of TBA clusters present in bulk TBA:TOL mixtures have been shown to disintegrate and disappear rapidly once its concentration in mixture goes below 20% by a combination of Raman spectroscopy, ^{1}H NMR and neutron scattering experiments and we speculated that persistence of a hydrogen-bonded network in nanoconfinement could be the result of H-bonding interactions between TBA and silica surface. Certainly this speculation needs a stronger justification and its resulting effect on the molecular organization needs to be investigated.

In this chapter we use gravimetric vapour sorption technique to find answers to the questions raised above. It is an isothermal vapour sorption process in which the relative pressure of the vapour of an adsorbing species is increased very gradually step-wise, such that at each step the system is under thermodynamic equilibrium. The resulting mass uptake can be systematically interpreted to understand from a thermodynamic point of view the role played by specific interactions between the adsorbing molecules and the substrate starting from the formation of first molecular layers at low relative pressures till complete condensation into liquid phase at high pressure. The extent of intermolecular interactions between different adsorbing species on a given surface can be compared by their relative thermodynamic affinity for the surface.

Adsorption phenomena for single-component systems consisting of a pair of adsorbate and adsorbent have been explained well since several decades from a thermodynamics and statistical physics standpoint[4,9,10,13,27,38,40–43,51,53]. However, the establishment of fundamentals on adsorption of multi-component systems[34,35] continues to face challenges due to the ever growing complexity such systems in spite of the progress in numerical simulations[1,6,19,24,25,31,33,36]. Currently, scientific interest has grown to understand adsorption of multicomponent systems[55,60] which show a very low gap of miscibility[12,17,22,23,25–27]. One of the earliest attempts were from Siperstein and Myers[53]. Besides, the ideal adsorbed solution theory, vacancy solution theory[28], extended Langmuir isotherm model[9] and other models[45,46,52] for binary liquid mixtures have provided significant improvement in explaining mixed-gas adsorption. Some of these models attempt to explain multicomponent adsorption equilibria from the individual single-component data.

The current work provides a model to interpret semi-quantitatively the role played by relative differences in thermodynamic affinity of components of a binary gas towards a substrate utilizing the mixed gas adsorption data, which in the case of TBA:TOL confinement in nanopores of different chemical environment shall be highly useful in interpreting and comparing the relative strength of interaction of each component with the pore surface and the possible role played by it to lead confinement induced structuration.

II Fundamentals of vapour sorption

The vapour sorption technique utilizes the property of adsorption of gases on given substrates for their characterization. This technique helps obtaining varied sorts of information, from understanding co-adsorption of gases essential for gas separation and filtration applications, to characterizing porous substrates and understanding the specific interactions between adsorbing gas molecules and the host matrix as discussed in the previous section. The adsorption mechanism of pure gases on solid substrates is understood to a great extent by the Langmuir[32] and Brunauer Emmett and Teller (BET)[10] developed on the basis of thermodynamics and statistical physics. The success of these models is shown in their wide application in characterization of porous systems.

The Langmuir model assumes, firstly, that all adsorption occurs only up to one monolayer of molecules in contact with the solid substrate, secondly, the entire surface is made of up a certain number of equivalent adsorption sites and thirdly, that particles adsorbed in adjacent sites do not interact with each other. The average number of adsorbed particles on a surface according to the Langmuir model is given as follows (equation 3.1)[20]

$$\langle N \rangle = \frac{N_0 \exp((\epsilon_0 + \mu)/k_B T)}{1 + \exp((\epsilon_0 + \mu)/k_B T)} \tag{3.1}$$

Here ϵ_0 is the energy of interaction of a single particle (atom) adsorbed on the surface, μ and T are the chemical potential and temperature of the gas reservoir. k_B is the Boltzmann constant and N_0 is the number of available sites for adsorption.

The BET model on the other hand assumes that besides the first monolayer adsorbed on a substrate's surface, the rest of incoming molecules adsorb as a continuous liquid film above the monolayer and in thermodynamic equilibrium with the reservoir of particles in gas phase. Since the BET model could account for more than a monolayer of adsorbed material, it is the classical choice for treatment of adsorption data and is widely used for determination of specific surface area of porous materials. Similar to the Langmuir model, the adsorbed particles on the adjacent sites to not interact with each other, neither do the particles in liquid state adsorbed over monolayer particles at adjacent sites. The BET model seems calculates the number of adsorbed particles at a given partial pressure of the gas as follows[20]

$$\langle N \rangle = \frac{N_0 K \xi}{(1 - \xi)[1 + (K - 1)\xi]} \tag{3.2}$$

Here K is known as the BET constant which depends on ϵ_0 and ϵ_l, the energy of interaction of an adsorbed particle on the surface of substrate and energy per particle of the multi-layer liquid film formed above the first adsorbed monolayer respectively. They are related together as $K = \exp\left(\frac{\epsilon_0 - \epsilon_l}{k_B T}\right)$. The term ξ is given as $\xi = \exp\left(\frac{\mu + \epsilon_l}{KT}\right) = \frac{P}{P_{sat}}$, where P_{sat} is the saturating pressure of the adsorbing, while $\frac{P}{P_{sat}}$ is the relative pressure.

Thus, according to a BET model, the number of adsorbed particles is simply dependent on ξ, considering that N_0 and K are constants for a given surface and adsorbing gas pair. In the context of real substances, the weight gained by the porous substance upon adsorption of certain gas atoms or molecules could be translated directly into the number of particles by converting it into number of moles gained (1 mole=N_A, Avagadro number of particles). As the value of ξ heads towards 1, the number of adsorbed particles as predicted by the BET equation heads towards infinity. However when we talk about adsorption inside a pore, the restricted spatial environment puts a limit to the number of particles that could be adsorbed, thus making the BET model valid only up to low relative pressures $\xi = 0.15 - 0.3$, beyond which the adsorbing particles tend to condense into liquid state.

The following section describes the experimental procedure used to adsorb our model binary gas mixture of TBA:TOL in a porous substrate of choice over a range of different concentrations.

III Experimental procedure

The adsorption of binary gas mixture of TBA and toluene was carried out by the VTI–SA+ Vapour Sorption apparatus from TA instruments, a Dynamic Vapour Sorption apparatus[56] using nitrogen as a carrier gas. The two liquids, TBA and toluene were mixed together in a desired ratio and filled into the reservoir. The reservoir was maintained at 35 °C, which was sufficient to vaporize the liquid mixture to a binary gas mixture, thanks to high volatility of the two liquids at room temperature itself. Dry nitrogen gas was connected to the setup and its pressure was maintained at 1.4 bar approximately in order to create a flow of the gas from the nitrogen cylinder to the apparatus. A flow of nitrogen gas went and mixed with binary gas mixture located in the evaporator, forming an organic vapor carried by nitrogen with a partial pressure corresponding to the binary liquid saturating pressure. This saturated gas flow is then mixed with a second flow of dry nitrogen gas in order to tune the resulting partial pressure. The concentration of the organic vapor in the gas stream reaching the sample is determined by the fraction of gas going through the organic solvent evaporator and the fraction of dry gas by using mass flow controllers, one for dry nitrogen and the other for nitrogen saturated with organic vapor. The mixture of dry nitrogen and binary gas was sent to the sample chamber consisting of a microbalance with two pans, one of which contained MCM–41 powder, while the other was left empty as a reference for measuring the change in weight of the sample.

A drying step prior to the adsorption process was carried out, where the powder was heated to 120 °C, at a heating rate of 2 °C min^{-1} under dry nitrogen flux for 120 minutes to remove any possible remaining adsorbed solvents or water inside the pores of MCM–41. After the completion of this step, a mixture of binary gas and nitrogen was being sent to the sample. The partial pressure steps which we denote by $\frac{P}{P_0}$, where P_0 is the saturating pressure for the binary gas and P is the partial pressure of the binary gas, were increased from 0 to 0.95 and decreased from 0.95 to 0 again during the adsorption and desorption steps respectively. The adsorption of gas on the MCM substrate was

quantified at equilibrium. The equilibrium criterion in our experiments before moving on from a certain partial pressure step to the next one was a change in weight of the sample lower than 0.0010 % during at least 5 minutes. Both the sample cell and reservoir (saturator) of liquid are maintained at the same temperature (35 °C), with an accuracy of a few degrees. The increase/decrease in mass of the sample during adsorption/desorption respectively was recorded as percentage-change in mass of the sample and was plotted against increasing/decreasing values of $\frac{P}{P_0}$. The liquid reservoir was filled with TBA and toluene mixtures in different compositions, ranging between pure toluene and pure TBA.

Several liquid bath compositions have been studied, the corresponding list of TBA volume fractions is : 0.0, 0.2, 0.5, 1.0, 2.0, 5.0, 10.0, 30.0, 50.0, 70.0, 90.0 and 100.0 %. The schematic of the vapour sorption setup is shown in figure 3.1. The humidity sensor shown in the setup is simply a part of the instrument used only for water adsorption experiments and is not to be taken into account in the context of current work. The porous substrates

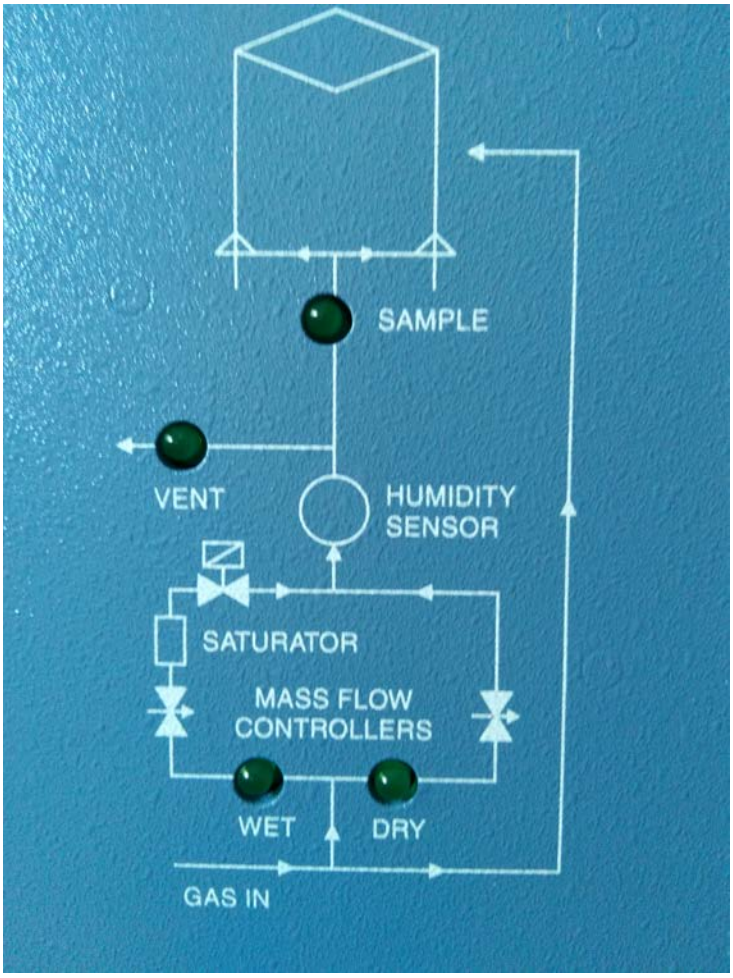

Figure 3.1: Schematic diagram of the vapour sorption experiment

of choice were MCM-41 and CMK-13, both having pore sizes a few molecular layers wide, a hexagonal arrangement of pores, however differing in the chemical nature of the pores. While MCM-41 consists of silanol groups on its pore walls giving it a hydrophilic nature,

CMK-13 has carbonized pore walls, giving it a hydrophobic character. Understanding of the nature of TBA:TOL binary gas adsorption in these two different materials is discussed in the following sections.

IV MCM-41: Results and discussion

Typical adsorption isotherms of TBA:TOL adsorption in MCM-41 pores are shown in figure 3.2. Here the x-axis is represented by $\frac{P}{P_{sat}}$, the partial pressure relative to P_{sat} which is the saturation pressure of the binary gas-liquid equilibrium. Although complete cycles of adsorption and desorption were carried out, due to highly ordered MCM-41 with very little pore size distribution (see introduction), the adsorption and desorption curves are almost completely identical with negligible to no hysteresis as shown in figure 3.3. The vapour sorption curve of TOL was found to be in good agreement with previously reported volumetric-adsorption experiment of TOL in MCM-41[5]. In the current work we focus our attention only to the adsorption process. All isotherms can be divided in three regions. The partial-pressure region with $\frac{P}{P_{sat}} \leq 0.1$ is characteristic of formation of first few monolayers. By this point we notice that these monolayers already contribute to about 30% weight increase of the powder. Succeeding to it is the capillary condensation region marked by a step-rise of adsorbed mixture which occurs due to condensation of the adsorbing gas mixture into a binary liquid mixture. Finally we reach a plateau beyond which the weight of the porous powder does not increase any more owing to completely filled pores. We now treat step by step each stage of the adsorption process in the following sections.

A Low partial pressure region

As discussed in section II the BET model for treatment of adsorption data at low pressures is widely used for single-component systems. We developed a multi-component BET adsorption model with same basic assumptions as in the single-component BET model. Like in the classical BET model for a pure gas, we assume that a binary gas made of two components $i = 1, 2$ is adsorbed on a planar surface divided in N_0 equivalent adsorption sites. The scheme of the binary gas adsorption is shown in figure 3.4.

A.1 Calculating the grand canonical partition function

Pure gas

The canonical partition function Z of a perfect gas adsorbing on a single site is given by $Z = \frac{1}{N!}\left(\frac{V}{\lambda^3}\right)^N$, where N and V are the number of particles and volume of the gas respectively and λ is called the thermal length given by $\lambda = \dfrac{h}{\sqrt{2\pi m K_B T}}$. We thus calculate the free energy as:

$$F = -k_B T \ln(Z) \simeq N k_B T[\ln\left(\frac{N}{V}\lambda^3\right) - 1]$$

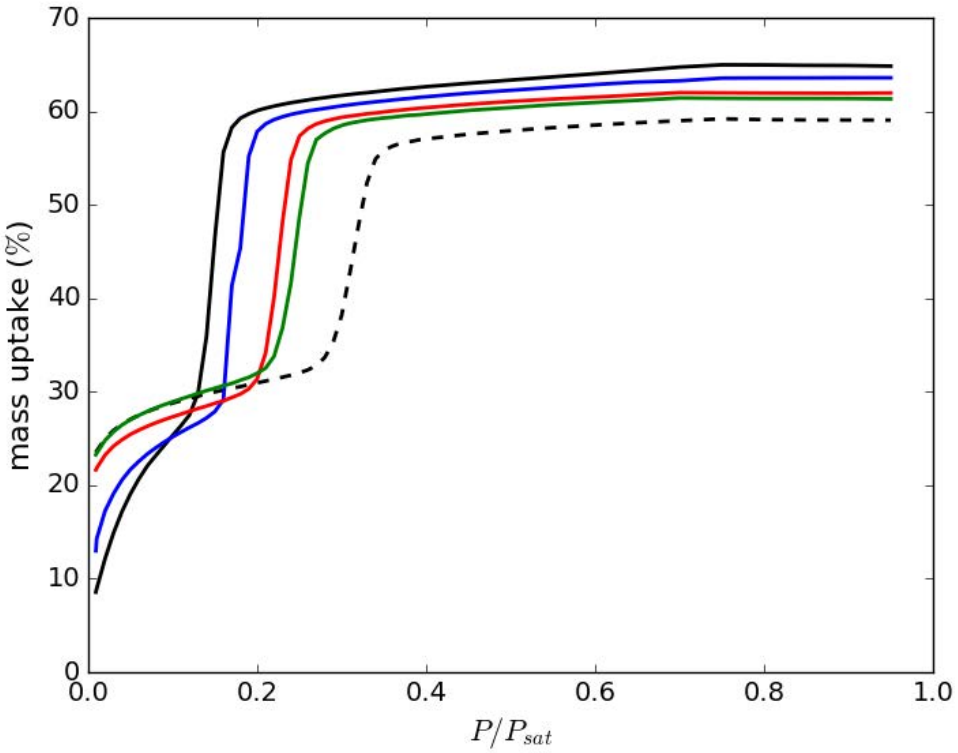

Figure 3.2: Vapour sorption isotherms (adsorption branch) of TBA:TOL mixtures in MCM-41 measured at 35 °C for different volume fractions:pure toluene (solid black line), $x_{TBA} = 0 : 5\%$ (blue line), $x_{TBA} = 10\%$ (red line), $x_{TBA} = 50\%$ (green line) and pure TBA (black dashed line). For clarity, only a few concentrations ar shown.

And thus pressure of the gas as

$$P = -\left.\frac{\partial F}{\partial V}\right|_{T,N} = \frac{N k_B T}{V}$$

(equation of state of a gas). The chemical potential of the gas is calculated as:

$$\begin{aligned}\mu_g &= \left.\frac{\partial F}{\partial N}\right|_{T,V} \\ &= k_B T \ln\left(\frac{N\lambda^3}{V}\right) \\ &= k_B T \ln\left(\frac{P\lambda^3}{k_B T}\right) \\ &= k_B T \ln\left(\frac{P}{P_0}\right)\end{aligned} \tag{3.3}$$

Where $P_0 = \dfrac{k_B T}{\lambda^3}$ is the reference pressure. However it is more practical to use the liquid saturation pressure P_{sat} as a reference. The chemical potential μ_l and energy per particle

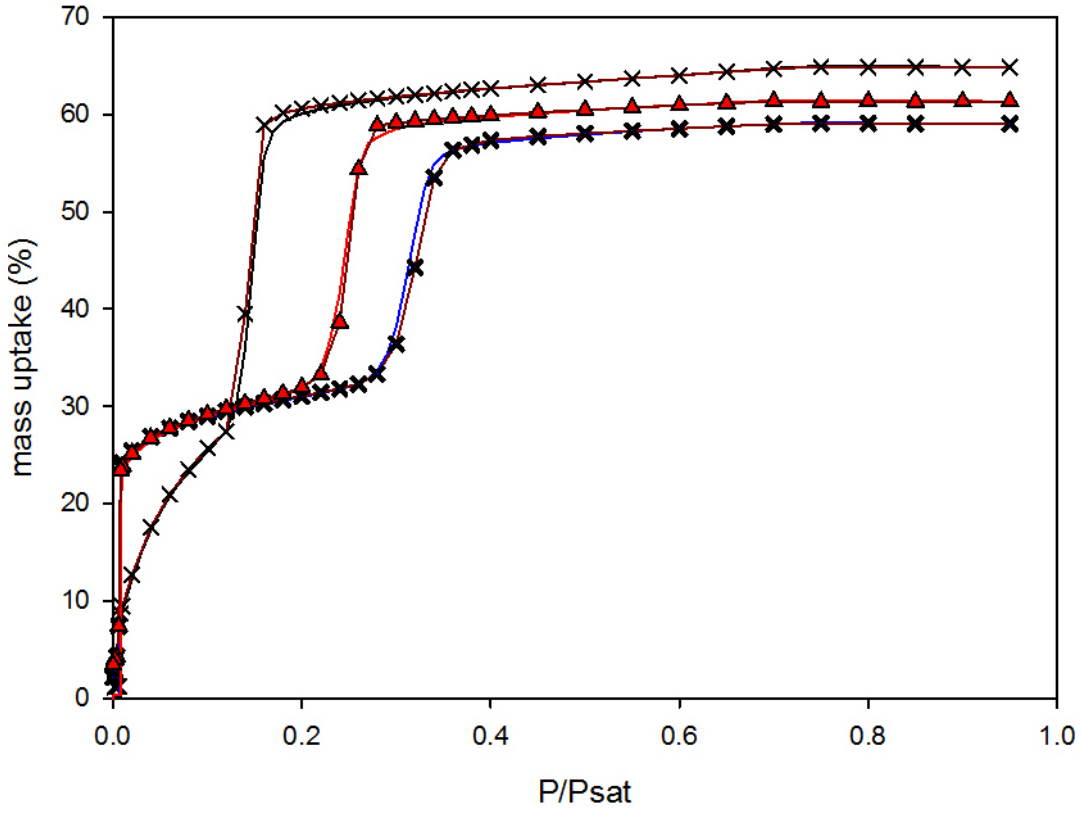

Figure 3.3: Adsorption branch of TBA, TOL and TBA:TOL mixture with 50% TBA by volume, shown by solid blue, black and red lines respectively and their corresponding desorption curves shown by thick black crosses, thin black crosses and red triangles respectively in MCM-41 measured at 35 °C.

of the liquid are related to each other as $\mu_l = -\varepsilon_l$. The chemical potential of gas and liquid are related to the P_{sat} as shown in equation 3.4.

$$\mu_g - \mu_l = k_B T \ln\left(\frac{P}{P_{sat}}\right) \tag{3.4}$$

or equivalently:

$$\xi = \frac{P}{P_{sat}} = \exp\left(\frac{\mu_g + \varepsilon_l}{k_B T}\right) \tag{3.5}$$

Multi-component gas

In the current chapter we will use x and y to denote volume fraction/mole fraction of a certain component in a liquid mixture and gas mixture respectively. The partial pressure of the i^{th} component in a gas mixture can be related to the total pressure by:

$$P_i = y_i P \tag{3.6}$$

Where y_i is its mole(or volume) fraction in the gas mixture. At the mixture liquid-vapour equilibrium $P = P_{sat}$, the saturation pressure. At this point the chemical potentials of

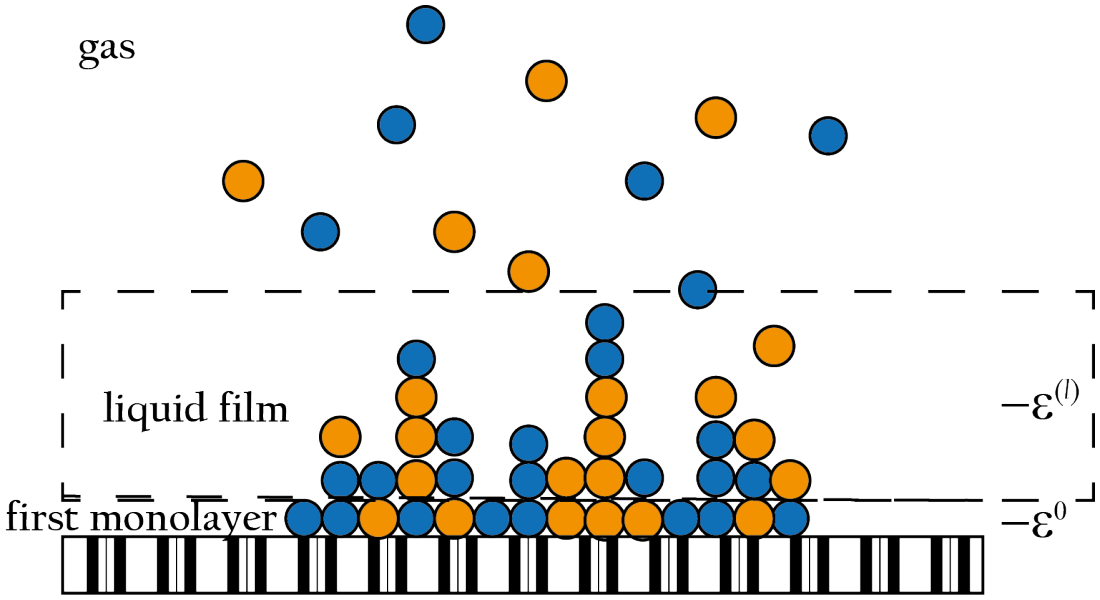

Figure 3.4: Scheme of the adsorption of a binary gas mixture on independent sites of a planar surface as described by a binary BET model.

the i^{th} component of in the gas and liquid mixture are related as :

$$\mu_i^{(g)}(P = P_{sat}) = \mu_i^{(l)} = -\varepsilon_i^{(l)}$$

$\varepsilon_i^{(l)}$ being the energy per particle of the i^{th} component in the liquid state. If we generalize equation 3.4 for the mixture we have for each component at any partial pressure P_i :

$$\mu_i^{(g)} - \mu_i^{(l)} = k_B T \ln\left(\frac{P_i}{P_{sat}}\right) \tag{3.7}$$

or equivalently :

$$q_i = \frac{P_i}{P_{sat}} = y_i \xi = \exp\left(\frac{\mu_i^{(g)} + \varepsilon_i^{(l)}}{k_B T}\right) \tag{3.8}$$

A.2 The multi-component BET model

We denote the canonical partition function of adsorption on a single site by z, then the grand canonical function of adsorption on all the N_0 sites is given by

$$Z = z^{N_0} \tag{3.9}$$

The energy of the first adsorbed particle on a site and energy per particle making up the multi-layer liquid film are given by $-\varepsilon^0$ and $-\varepsilon^l$ respectively as shown in figure 3.4. For the component i of mixture, this is denoted by $-\varepsilon_i^0$ and $-\varepsilon_i^l$ respectively. In the context of this work, $i = 1, 2$ as we are dealing with a binary gas mixture. A given state on one site is then determined by only two numbers: the number of particles of type i adsorbed, and the total number of adsorbed particles on the site. Depending on its energy an adsorbed particle is present in three different states:

1. Zero particle adsorbed, reference energy $\varepsilon = 0$

2. Particle of type 1 is adsorbed on the surface directly. n particles are adsorbed on it making the multiple layers, consisting of n_1 particles of type 1, and $n - n_1$ particles of type 2. The total number of particles at a given site is thus $n+1$ and the number of type 1 particles is n_1+1. The particles making up the multi-layer film are present in $C_n^{n_1}$ equivalent states, each with energy $\varepsilon = \varepsilon_1^0 + n_1\varepsilon_1^{(l)} + (n - n_1)\varepsilon_2^{(l)}$.

3. Particle of type 2 is adsorbed on the surface directly instead of particle 1 and all the conditions remain same as in 2. above. Thus the particles making up the multi-layer film are present in $C_n^{n_1}$ number of equivalent states, each with energy $\varepsilon = \varepsilon_2^0 + n_1\varepsilon_1^{(l)} + (n - n_1)\varepsilon_2^{(l)}$.

The partition function for a given adsorption site z is thus given by:

$$z = 1 + \sum_{n=0}^{\infty}\sum_{n_1=0}^{n} \mathbb{C}_n^{n_1} \exp\left(\frac{\mu_1 + \varepsilon_1^0 + n_1\mu_1 + n_1\varepsilon_1^{(l)}}{k_BT}\right) \times \exp\left(\frac{(n - n_1)\mu_2 + (n - n_1)\varepsilon_2^{(l)}}{k_BT}\right) \tag{3.10}$$

The liquid film comprising the adsorbed multi-layers is in equilibrium with the gas reservoir, thus having the same chemical potential, i.e. $\mu_i = \mu_i^{(g)}$. Applying this to equation 3.7, we have

$$\exp\left(\frac{\mu_i + \varepsilon_i^{(l)}}{k_BT}\right) = q_i = y_i\xi$$

Therefore we re-write equation 3.10 as:

$$\begin{aligned} z =& 1 + \left[\exp\left(\frac{\mu_1 + \varepsilon_1^0}{k_BT}\right) + \exp\left(\frac{\mu_2 + \varepsilon_2^0}{k_BT}\right)\right] \times \\ & \sum_{n=0}^{\infty}\sum_{n_1=0}^{n} \mathbb{C}_n^{n_1} \exp\left(\frac{n_1\mu_1 + n_1\varepsilon_1^{(l)}}{k_BT}\right) \exp\left(\frac{(n - n_1)\mu_2 + (n - n_1)\varepsilon_2^{(l)}}{k_BT}\right) \\ =& 1 + \left[\exp\left(\frac{\mu_1 + \varepsilon_1^{(l)} - \varepsilon_1^{(l)} + \varepsilon_1^0}{k_BT}\right) + \exp\left(\frac{\mu_2 + \varepsilon_2^{(l)} - \varepsilon_2^{(l)} + \varepsilon_1^0}{k_BT}\right)\right] \times \sum_{n=0}^{\infty}\sum_{n_1=0}^{n} \mathbb{C}_n^{n_1} q_1^n q_2^{n-n_1} \end{aligned} \tag{3.11}$$

According to Newton's binom, we can rewrite the term $\sum_{n_1=0}^{n} \mathbb{C}_n^{n_1} q_1^n q_2^{n-n_1}$ as

$$\sum_{n_1=0}^{n} \mathbb{C}_n^{n_1} q_1^n q_2^{n-n_1} = (q_1 + q_2)^n$$

This leads us to

$$z = 1 + \frac{K_1q_1 + K_2q_2}{1 - q_1 - q_2} \tag{3.12}$$

With the constants

$$K_i = \exp\left(\frac{\varepsilon_i^0 - \varepsilon_i^{(l)}}{k_B T}\right)$$

Where K_i is equivalent to the BET constant of the i^{th} component of the mixture (see equation 3.2), which is indicative of the strength of interaction of an adsorbed particle on the substrate surface relative to that with the multi-layer liquid phase. Thus a higher value of K indicates stronger affinity of a given particle to adsorb on the substrate surface. We now calculate $\langle N_i \rangle$, the average number of particles of type i adsorbed as follows:

$$\langle N_i \rangle = N_0 k_B T \frac{\partial \ln z}{\partial \mu_i} = N_0 k_B T \frac{\partial \ln z}{\partial q_i}\frac{\partial q_1}{\partial \mu_i} = N_0 \frac{q_i}{z}\frac{\partial z}{\partial q_i}$$

Utilizing equation 3.12 here, we obtain

$$\frac{\partial z}{\partial q_i} = \frac{K_i(1-\xi) + K_1 q_1 + K_2 q_2}{(1-\xi)^2}$$

Which leads us to equation 3.13

$$\langle N_i \rangle = N_0 y_i \frac{\xi}{1-\xi}\frac{K_i(1-\xi) + K_1 q_1 + K_2 q_2}{1-\xi + K_1 q_1 + K_2 q_2} \tag{3.13}$$

We re-write equation 3.13 based on S_p, the total specific surface area of the sample and a, the average effective surface area of the adsorbing particles such that $N_0 = \frac{S_p}{a}$

$$\boxed{\langle N_i \rangle = \frac{S_p y_i}{a}\frac{\xi}{1-\xi}\frac{K_i + \xi[(K_i - K_j)y_i + K_j - K_i]}{1 + \xi[(K_i - K_j)y_i + K_j - 1]}} \tag{3.14}$$

Where $i, j = 1, 2$ for referring to TBA and TOL.The value of S_p is determined experimentally through nitrogen-adsorption, while y_i is known before-hand. ξ are simply the partial-pressure steps, thus leaving us with $K_{i,j}$, relative energetic affinities of the two adsorbing components upon which $\langle N_{i,j} \rangle$ and consequently the total number of adsorbed particles $\langle N \rangle = \langle N_i \rangle + \langle N_j \rangle$ depends, with "a" being a result of relative number of i and j particles adsorbed. From nitrogen-adsorption isotherms carried out on MCM-41 synthesized in our lab we have the BET specific surface area $S_p = 970\,\mathrm{m^2\,g^{-1}}$. The values of ξ belong to $\frac{P}{P_{sat}} \leq 0.15$, characteristic of low partial pressure region, as already discussed. The values of y_i were not determined directly by experiment, but were calculated from volume fraction x_i of the liquid solution, which elaborated in the introduction.

From the $\langle N_i \rangle$ values, the corresponding % mass uptake could be calculated using the following equation.

$$\%massuptake = \frac{\langle N_1 \rangle M_1 + \langle N_2 \rangle M_2}{N_A m_i} \times 100 \tag{3.15}$$

Where $\langle N_{1,2} \rangle$ and $M_{1,2}$ are the number of molecules of component 1 and 2 adsorbed and their molecular weights respectively. N_A is the Avogadro number ($6.023 \times 10^{-23}\,\mathrm{mol^{-1}}$) and m_i is the initial (empty) weight of the porous substrate.

A.3 Composition of the first monolayer

The average total number of adsorbed particles in the low partial pressure region can be calculated from equation 3.14 as $\langle N_t \rangle = \langle N_i \rangle + \langle N_j \rangle$. From equation 3.14 we have

$$\langle N_t \rangle = \frac{S_p}{a} \frac{\xi}{1-\xi} \frac{\bar{K}}{1+\xi(\bar{K}-1)} \tag{3.16}$$

Where $\bar{K} = K_i y_i + K_j y_j$. A monolayer would be formed when all the N_0 sites are completely filled, in other words when $\langle N_t \rangle = N_0 = \frac{S_p}{a}$. From equation 3.16 we thus have

$$\frac{\xi}{1-\xi} \frac{\bar{K}}{1+\xi(\bar{K}-1)} = 1$$

We denote the ξ at monolayer formation as ξ_m. The above equation could be expressed as function of ξ_m as

$$\xi_m = \frac{\sqrt{\bar{K}}-1}{\bar{K}-1} \tag{3.17}$$

The monolayer composition x_m at ξ_m is thus given by:

$$x_m(\xi_m) = \frac{\langle N_i \rangle}{\langle N_t \rangle} = y_i \frac{(\bar{K}-K_i)+\sqrt{\bar{K}}(K_i-1)}{\sqrt{\bar{K}}(\bar{K}-1)} \tag{3.18}$$

In further discussions the reference to compositions of the binary gas, monolayer or liquid reservoir will be made to TBA i.e. i=TBA.

A.4 Application of the Multi-component BET to adsorption isotherms

Figure 3.5(a) shows the best fits of experimental points in the adsorption isotherm (dots) by equation 3.15 by keeping the value of S_p constant (see section A.2) and adjusting a single set of K_i for all curves and a different value of effective molecular area a for each concentration.

The best fit of the curves gives

$$K_{TBA} = 3652 \pm 200$$

$$K_{TOL} = 36 \pm 2$$

while the best fit values of a are shown in figure 3.5(b). We find that K_{TBA} is two orders of magnitude larger than K_{TOL}. This indicates a much higher thermodynamic affinity of MCM-41 surface to adsorb TBA molecules compared to TOL. The effect of this is observed evidently in the composition of monolayer formed on MCM-41 pore surface as shown in figure 3.5(b)(dashed line) where the TBA composition of monolayer is plotted against its concentration in the binary gas (y_{TBA}) and in the bulk liquid reservoir (x_{TBA}). Once the concentration of TBA in vapour crosses $\approx 20\%$ ($\approx 10\%$ in liquid), its concentration in the monolayer is almost 100% and with increasing TBA concentration in the

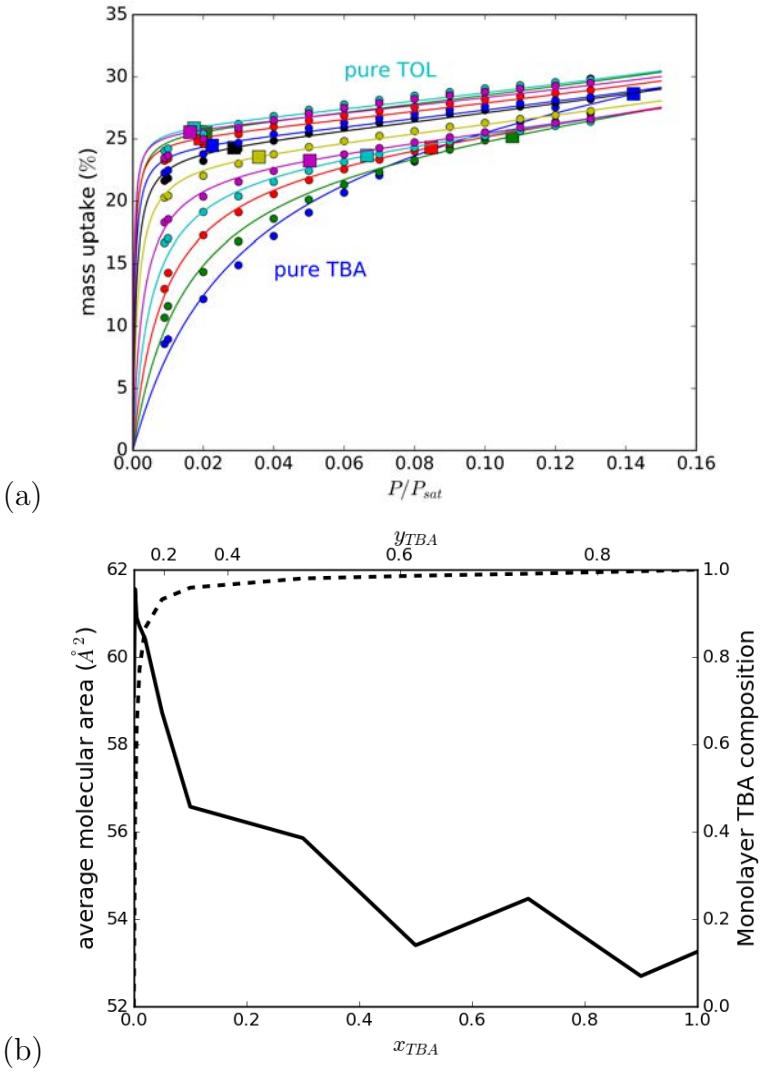

Figure 3.5: **(a)** Multi-component BET fits (full lines) of adsorption isotherms (dots) for ξ or $\frac{P}{P_{sat}} \leq 0.15$ from pure TBA (light blue, topmost) to pure TOL (dark blue, lower most). The squares are ξ_m, partial pressure of monolayer formation. **(b)** Monolayer TBA composition x_m^{TBA} (dashed line) and average molecular area a versus TBA composition in liquid reservoir x_{TBA} and in the binary gas y_{TBA} (solid line)

vapour (and liquid respectively) it makes up 100% of the monolayer.

The variation of the effective BET molecular a a with composition of TBA (figure 3.5(b)) qualitatively follows the same trend as that of monolayer composition, highest at pure TOL and decreasing with increasing TBA composition, however not equally sharply. From equation 3.14 the value of P/P_{sat} at complete monolayer adsorption was calculated and using equation 3.18 the mass of monolayer at that pressure was calculated as shown by the squares in figure 3.5(a). The mass of monolayer estimated for pure TOL is an artificial value as its capillary condensation step occurs before the calculated value of P/P_{sat}

for monolayer formation. However, instead of a monotonic decrease in mass of monolayer as should be expected with increase in TBA composition, we observe that after decreasing to some extent, the monolayer mass begins to increase once again as composition of TBA reaches higher values. This is consistent with the non-constant effective molecular area. At this point we reach certain limits of our multi-component model, which does not account for the differences in nature of molecular interactions in the two components, being a mix of Van der Waal's and aromatic potential for TOL, while hydrogen-bonding for TBA which is related to the density of silanol groups on the pore surface of MCM-41. Also, the possibility of specific interactions between neighbouring sites could not be totally ruled out. In the frame of BET approach, a lower density of adsorption sites is equivalent to a higher effective molecular area. Considering that the cross-sectional area of TBA molecules is smaller than TOL, an increase in mass of monolayer at high TBA concentration could be explained by the possibility of filling in more TBA molecules in a give area leading to densification of the monolayer and an increase in its mass.

The increasing partial pressure leads to adsorption of more number of molecules over the monolayer leading us to the next phase of the adsorption process known as capillary condensation.

B Capillary Condensation

The increasing partial pressure continues to build up more number of molecular layers on the pore surface until we reach a certain pressure where a condensed liquid phase becomes thermodynamically more favourable[11,14,47]. We denote this as the capillary condensation pressure P_c. At P_c we notice a sharp rise in mass of adsorbed material (figure 3.2). The $\frac{P_c}{P_{sat}}$ values are found to be strongly concentration dependent and increase with increasing TBA composition in the gas phase (y_{TBA}) as shown by black dots in figure 3.6.

We find here that the capillary condensation pressures are much higher than that of monolayer formation (see figure 3.5 (a) (square boxes)), giving a clear indication that capillary condensation does not occur directly after monolayer formation. This is also visible in the mass of adsorbed material, which is approximately twice at capillary condensation step than at monolayer formation. Following the works of Celestini[11] and Pellenq et al[15], the capillary condensation pressure P_c can be related to the surface tension σ of the bulk liquid at the liquid-gas interface through a modified-Kelvin equation:

$$\frac{P_c}{P_{sat}} = \exp\left[-\frac{\sigma}{k_B T \rho (R_0 - t - \lambda)}\right] \tag{3.19}$$

Where R_0, ρ and T are the radius of pore, number density of the adsorbed film and the temperature respectively. t is thickness of the adsorbed film and λ is a nanometric correlation-length between the solid-film and film-gas interfaces. Surface tension measurements of pure TBA, TOL and their bulk mixtures were carried out at 35 °C and plotted in figure 3.7 (black dots) against the x_{TBA} mixture compositions of the liquid reservoir while the solid blue line shows the best fit obtained using the Hildebrand and Scott model[58] for

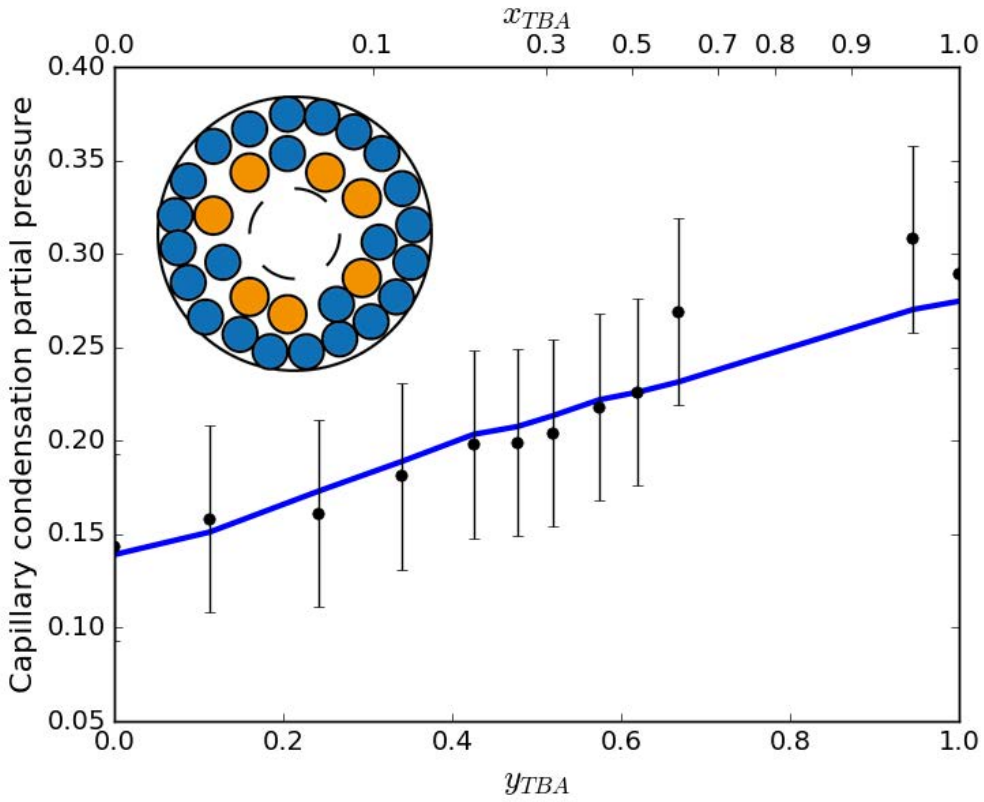

Figure 3.6: Experimental capillary condensation relative partial pressures ($\frac{P_c}{P_{sat}}$) of the TBA/TOL solutions adsorbed in MCM–41 versus TBA composition of the gas (y_{TBA}) or liquid (x_{TBA}) solution. The solid line is the best fit according to the modified Kelvin equation 3.19 (see text). Inset: Scaled schematic representation of the adsorbed film at the capillary condensation pressure. The blue (resp. orange) filled circles represent TBA (resp. TOL) molecules. The dashed circle shows the predicted inner radius of the adsorbed liquid film at the capillary condensation.

calculating surface tensions of bulk liquid mixtures.

$$\sigma = \sigma_{tba}x_{tba} + \sigma_{tol}x_{tol} - \frac{(\sigma_{tba} - \sigma_{tol})^2}{k_B T}(x_{tba}A_{tol} + x_{tol}A_{tba})x_{tba}x_{tol} \tag{3.20}$$

Where σ, σ_{tba} and σ_{tol} are the surface tensions of TBA:TOL mixtures, TBA and TOL respectively. x_{tba} and x_{tol} are their mole fractions and the fitting parameters are their molecular cross-sections A_{tba} and A_{tol} respectively. The result of fit gives us:

$$A_{tba} = 2.9 \times 10^{-19}\,\mathrm{m}, A_{tol} = 3.5 \times 10^{-19}\,\mathrm{m}$$

They correspond to effective molecular radii of $r_{tba} = 0.3\,\mathrm{nm}$ and $r_{tol} = 0.33\,\mathrm{nm}$ respectively which are not so far from their Van der Waals radii $r^v_{tba} = 0.43\,\mathrm{nm}$ and $r^v_{tol} = 0.47\,\mathrm{nm}$[25] respectively. The good correlation between the two radii suggests that the correction to be made to the Hildebrand and Scott model due to the non-ideal nature of our solutions is small.

A concentration dependent $\frac{P_c}{P_{sat}}$ (figure 3.6) indicates that irrespective of forming a nearly

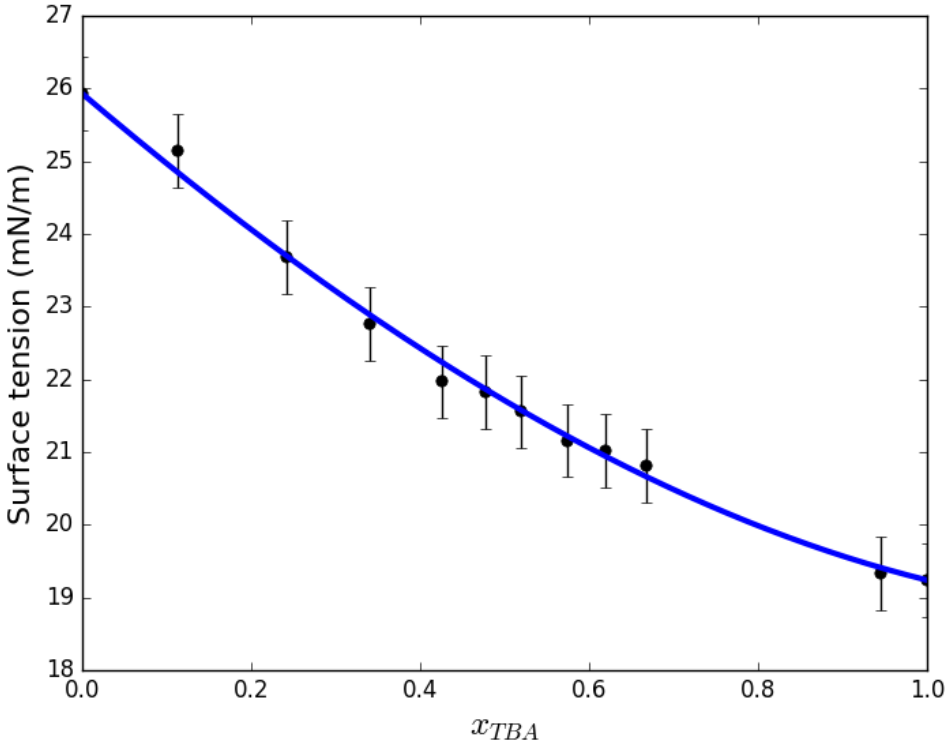

Figure 3.7: Experimental surface tensions of the bulk TBA/TOL solutions. The solid line is the best fit obtained using the Hildebrand–Scott equation (see text).

pure TBA monolayer of fixed thickness equivalent to a size of TBA molecule for almost all mixture compositions, the situation just prior to capillary condensation step varies with concentration. The solid blue line in figure 3.6 is a fit of the black points with the modified-Kelvin equation (eq.3.19). Surface tension σ and number density ρ values of bulk liquid mixtures of composition x_{TBA} at 35 °C were used along with known radius of MCM-41 (3.4 nm) pores keeping the term $t + \lambda = \delta$ as the adjustable parameter. The best fit is obtained for $\delta = 1.14$ nm. This value is approximately twice the thickness of a monolayer of TBA, which might as well be interpreted from the mass of adsorbed material at capillary condensation, which is about twice of that at monolayer (see figures 3.2 and 3.5 (a)).

We do not have any direct measurement on either t or λ, but we are certainly sure that $t > 0.43$ nm, i.e. thickness of one monolayer of TBA. Thus we have $\lambda < 0.71$ nm, a value for correlation length too high for simple liquids[47]. However it is easily noticed that capillary condensation takes place at a partial pressure much higher than of monolayer formation. Thus with the assumption of t to be approximately two monolayers thick we arrive at the correlation length, $\lambda \approx 0$, implying that there exists two uncorrelated layers making up the film preceding capillary condensation. We interpret this to be a result of complete coverage of the silica surface by a monolayer of TBA. This blocks

the silanol groups which were formerly freely available and prohibits the possibility of hydrogen-bonding interactions with incoming molecules. The second layer is formed on a hydrocarbon surface of TBA molecules which does not have specific preference to either of the two molecules. This layer is made up of both TBA and TOL and is not correlated with the TBA monolayer strongly attached to the pore wall. Considering how well equation 3.19 fits the experimental points using surface tension and number-density values of bulk TBA:TOL mixtures of x_{TBA} composition, it appears that the average composition of the adsorbed film is about the same as x_{TBA}.

If the conclusions above are true, then we expect the monolayer of TBA which is strongly attached to the pore wall to exist even after the capillary condensation pressure. This point is addressed in the following section.

C High partial pressure region

Subsequently after the capillary condensation stage we notice in figure 3.2 at high partial pressures the adsorption curves reach a plateau implying that the pores are completely filled with a binary mixture of TBA and TOL. The final mass of the adsorbed material m_f could be written as as a function of x_{TBA} as

$$m_f(x_{TBA}) = V_p \left[\rho_{TBA}\phi_{TBA} + \rho_{TOL}(1 - \phi_{TBA})\right] \tag{3.21}$$

Where $V_p = 0.67\,\mathrm{cm^3\,g^{-1}}$ is the porous volume of MCM-41, ϕ_{TBA} is the volume fraction of TBA inside the pore and ρ_{TBA}, ρ_{TOL} are the densities of pure TBA and TOL. Equation 3.21 could be re-written to express ϕ_{TBA} in terms of the final adsorbed masses of a given mixture (m_f), TBA ($m_f(1)$) and TOL ($m_f(0)$).

$$\phi_{TBA}(x_{TBA}) = \frac{m_f(x_{TBA}) - m_f(0)}{m_f(2) - m_f(0)} \tag{3.22}$$

Figure 3.8 shows the variation of ϕ_{TBA} as a function of both x_{TBA} and y_{TBA} (black dots). Similar to the behaviour observed at low partial pressures, we notice a strong affinity of MCM-41 for adsorbing TBA preferentially as its volume fraction inside the pore is much higher compared to its corresponding composition in the mixture at liquid or vapour state. Even at very low amounts of TBA in the liquid (respectively vapour) state, the value of ϕ_{TBA} increases rapidly, up to a certain threshold for $\phi \approx 0.44$, beyond which its rise is more gradual with its increase in the liquid or vapour phase. From geometrical consideration, the volume fraction of pore occupied by a monolayer of TBA could be written down as

$$\phi_{mono} = \frac{(r_0 - d_{tba})^2}{(r_0)^2} \approx 0.44$$

Thus we speculate here that there is a phase separation of the two liquids, with formation of a monolayer or shell of TBA molecules as soon as we reach $\phi_{TBA} \approx 0.44$. Thus we can estimate the composition of the core enclosed inside the TBA-shell by the following equation.

$$x_{core} = \frac{\phi_{TBA} - \phi}{1 - \phi} \tag{3.23}$$

The red points in figure 3.8 show the variation of the volume fraction of TBA in the core (x_{core}) with x_{TBA} and y_{TBA}. We find the core to be highly concentrated in TOL, more than the initial liquid mixture in the reservoir. MCM-41 materials thus definitely act as a selective sieve for the alcohol (TBA). The key role of hydrogen bonding network of TBA in the physical mechanism of this selectivity is revealed clearly in the adsorption isotherms. A change in the selectivity is thus expected by tuning the chemical nature of the pore walls, i.e. from hydrophilic to hydrophobic. Vapour-sorption of TBA:TOL mixtures described in the following section on hydrophobic CMK-3 consisting of pore walls made of carbon addresses this question.

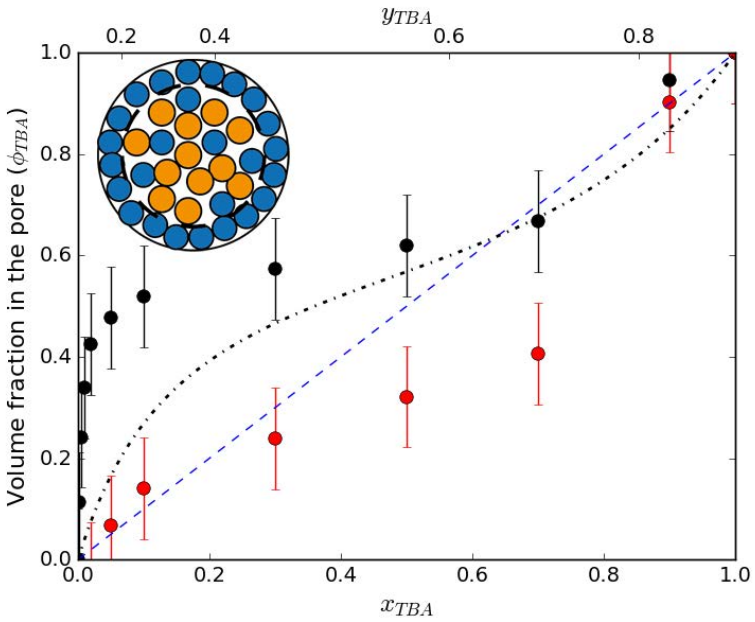

Figure 3.8: Final composition ϕ_{TBA} of the liquid inside the pores after capillary condensation versus the original composition x_{TBA} (black circles). The red circles show the deduced composition of the liquid in the core of the pore within the frame of a core–shell model. The black dotted curve shows the composition of TBA in binary gas versus in binary liquid mixture, while the blue dashed line is $y = x$ line indicating the composition of original liquid mixture as a guide for the eye.

V CMK-3: Results and discussion

In the previous sections, by the example of TBA:TOL mixtures confined in MCM-41 nanopores we saw how a greater thermodynamic affinity of silica surface towards TBA led to its strongly preferential adsorption and phase separation at complete pore filling. Switching the chemical nature of the surface from hydrophilic to hydrophobic would change the nature of interactions of TBA and TOL with the pore surface and consequently their thermodynamic affinity towards the surface, effects of which on the adsorption characteristics of our binary gas are worth investigating. For this purpose we choose CMK-3,

which as described in the introduction (chapter 1) is an ordered nanoporous material, possessing the same 2-D periodicity as its template matrix SBA-15, but with hydrophobic carbon walls instead of hydrophilic silica ones.

Due to an unfortunate drift in the sample environment (thermal insulation of the saturator reservoir) that occurred but could not be fixed during the present work, it was not possible to carry out the DVS experiments on CMK-3 materials at the same temperature as for silica matrices. Hence, TBA:TOL adsorption on CMK-3 was carried out at 25 °C, in order to limit the effects of temperature gradients on the measurements. The adsorption and desorption curves for all experiments are shown in figure 3.9.The data provided here for adsorption of $x_{TBA} = 0.9$ mixture is only for the adsorption branch and up to $P/P_{sat} = 0.13$.

As is clearly noticeable here, unlike MCM-41, in CMK-3 the adsorption branch does not follow the same shape. Mass uptake continues to increase quite linearly to high P/P_{sat} values and instead of a sharp first order change in mass uptake characteristic of capillary condensation phenomenon, a smoother gradual transition is observed between $P/P_{sat} = 0.4 - 0.6$. The final mass uptake changes proportionately with increasing concentration of TBA, however a significantly low mass uptake is seen for TBA which might be attributed to the fact that it starts crystallizing at ≈25 °C which can cause pore blocking and prevention of further uptake of molecules. As a consequence, we have decided not to take into account the data on pure TBA in the following analysis.

On the other hand we notice another major difference in the nature of desorption curves when comparing CMK-3 to MCM-41. Not only a strong hysteresis is observed, but also the desorption occurs in two steps. Such observation was made for nitrogen adsorption isotherms as well and is indicative of a broader pore size distribution (see introduction).

As in the case of MCM-41, we maintain our focus on the adsorption branch of CMK-3 as it is a step-by-step process in thermodynamic equilibrium, more suitable to understand surface-specific interactions between host and guest molecules.

A Low-partial pressure region

For adsorption in CMK-3, we observe a rather broad range of values of P/P_{sat} where formation of the first monolayers possibly take place, i.e. the region preceding capillary condensation pressure. We recall equation 3.13, the multi-component BET model derived in previous sections in order to calculate the average number of adsorbed particles and the resulting weight increase of the porous sample. We utilise $S_p = 368\,\mathrm{m^2\,g^{-1}}$ as obtained from BET surface area characterisation of our CMK-3 powder obtained from nitrogen adsorption isotherm.

Figure 3.10 (a), shows the experimental points of the adsorption of pure TOL and mixtures with composition $x_{TBA} = 0.5, 0.7, 0.9$ and their fits using the multi-component BET model (equation 3.15) obtained by keeping the BET specific surface area of CMK-3, $S_p = 368\,\mathrm{m^2\,g^{-1}}$ constant and once again adjusting a single set of K_i values, while letting

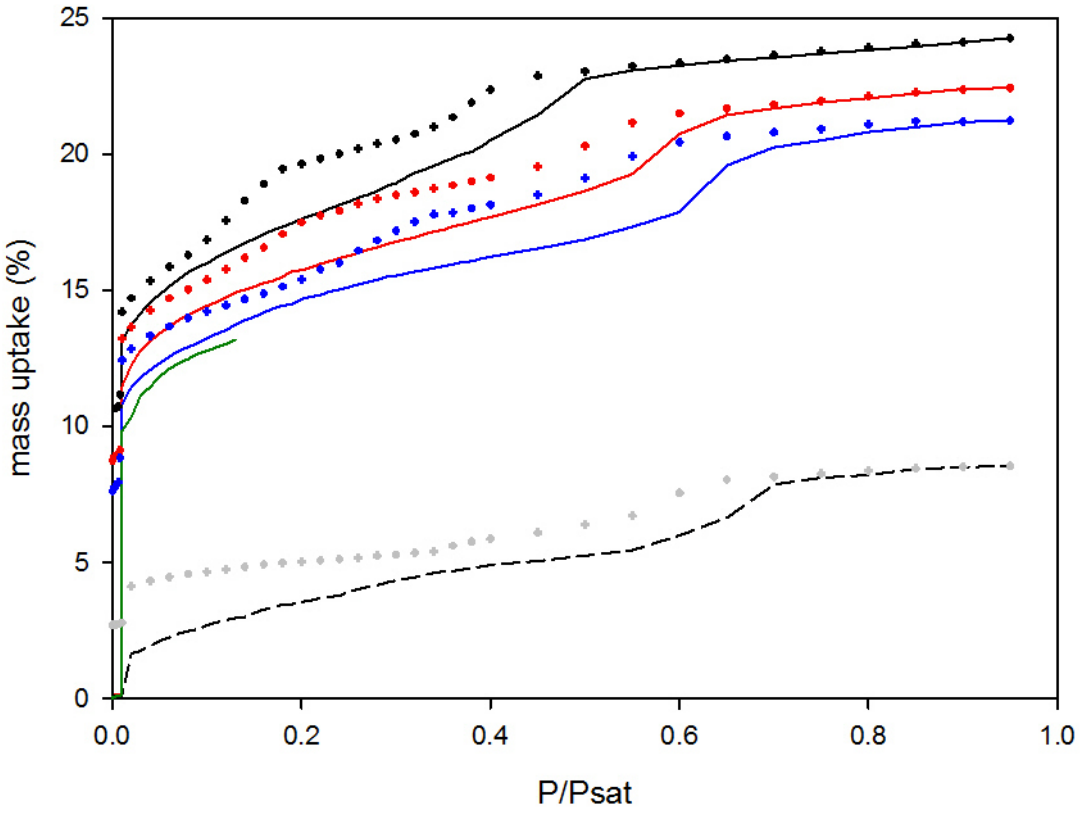

Figure 3.9: Adsorption curves of vapour sorption isotherms of TBA:TOL mixtures in CMK-3 measured at 25 °C for different volume fractions. Pure TOL: black solid line, $x_{TBA} = 0.5$: red, $x_{TBA} = 0.7$: blue, $x_{TBA} = 0.9$: green and pure TBA: dashed black line. The corresponding desorption curves are shown in black, red, blue and grey symbols for Pure TOL, $x_{TBA} = 0.5$, $x_{TBA} = 0.7$ and pure TBA respectively .

a, the effective BET molecular area to vary with each composition.

The best fit of the experiment yields

$$K_{TOL}^{cmk} = 1411 \pm 150$$

$$K_{TBA}^{cmk} = 239 \pm 30$$

i.e. K_{TOL} is approximately six times greater than K_{TBA}. This is in strong contrast to their corresponding values for adsorption in MCM-41, being $K_{TOL}^{mcm} = 36 \pm 2$ and $K_{TBA}^{mcm} = 3652 \pm 200$.

Even though the difference between these two values is not as high in CMK-3 as MCM-41, the thermodynamic affinity has obviously been reversed making TOL much more preferable for adsorption on CMK-3 surface than TBA. The impact of this reversal in surface-specific interactions is also observed as a smaller TBA monolayer concentration in comparison to its corresponding binary gas/binary liquid mixture as shown in figure 3.10(b) (dashed line). The composition of this monolayer in CMK is however not pure

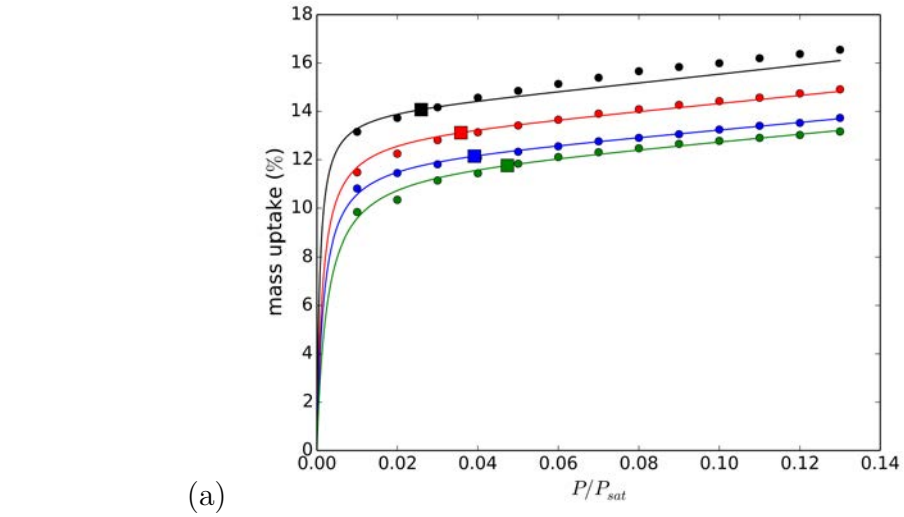

(a)

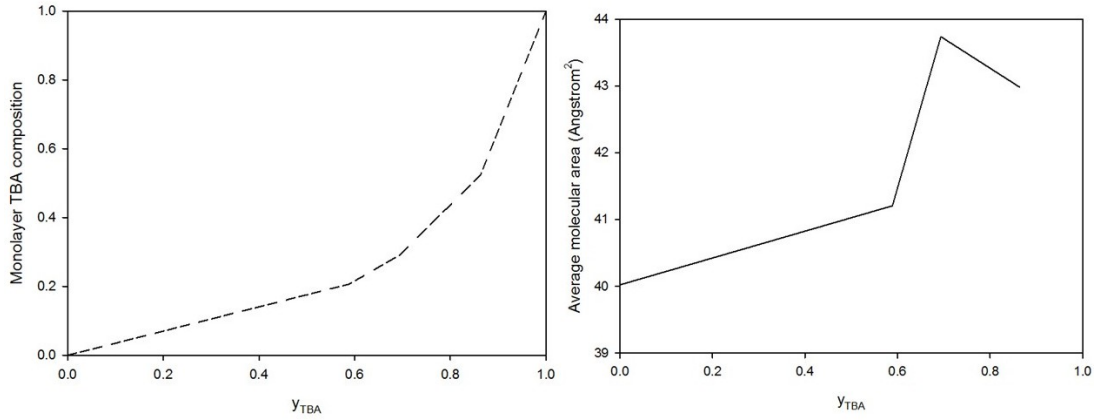

(b)

Figure 3.10: (a) Multi-component BET fits (full lines) of adsorption isotherms (dots) on CMK-3 up to $P/P_{sat} = 0.13$. Pure TOL (blue), $x_{TBA} = 0.5$ (red) and $x_{TBA} = 0.7$ (blue), $x_{TBA} = 0.9$ (green). Square points indicate the partial pressure at which monolayer is formed for each case. (b) Monolayer TBA composition versus y_{TBA} shown by dashed line while the solid line shows effective BET molecular area.

TOL, and this observation is in agreement with the smaller difference between K_{TBA} and K_{TOL}. On the other hand, the effective molecular area shown by solid line in figure 3.10(b) does not show any specific concentration dependence, rather stays in a narrower range when compared to its qualitative concentration dependence for MCM-41. The mass of monolayer decreases with increasing TBA concentration as seen in figure 3.10(a) (square points), which is in good agreement with the corresponding increase in TBA monolayer composition, TBA having a molecular weight lower than TOL .

The mass rise gradually continues much further to the partial pressure of monolayer formation ($0.4 \leqslant P/P_{sat} \leqslant 0.6$) until capillary condensation takes place, which shall be discussed in the following subsection.

B Capillary condensation

In figure 3.9 we observe a step-increase in the mass uptake between P/P_{sat} values ranging from 0.4-0.6, which appear to be characteristic of condensation of adsorbing molecules inside the pores as discussed earlier in this chapter for adsorption in MCM-41. However the major difference here is the smooth nature of this transition when compared to the abrupt change observed in MCM-41. It has been shown previously by GCMC simulations that for adsorption in nanopores with constant diameter as well as with constrictions of smaller diameters along the length of pore, the capillary condensation step becomes increasingly smoother with the increase of temperature beyond critical hystersis temperature (temperature beyond which adsorption-desorption hysteresis disappears) and we tend towards a critical point where the phase boundary between vapour and liquid state diminishes significantly[16]. It is important to note here that we observe a strong hystersis between adsorption and desorption curves in CMK-3 (figure 3.9) which leads us to interpret the observation on the basis of a second possibility.

As discussed earlier in the introduction chapter, the BJH treatment of nitrogen adsorption isotherms revealed a broad pore size distribution in CMK-3. Since capillary condensation pressure depends strongly on the curvature of a pore, such distribution of pore diameters prevents from having one sharp step rise at capillary condensation unlike MCM-41. Thus prediction of P_c/P_{sat} on the basis of modified Kelvin equation (equation 3.19) is not favourable. This adds to the fact that only three concentrations could be accessible to the experiment within the time available for this study, which is obviously too small for a detailed characterization of the capillary condensation behaviour, especially at low TBA concentrations.

However we do make an attempt to apply equation 3.19 for predicting capillary condensation pressures for two cases, first using the average pore radius $r_0 = 1.95\,\text{nm}$ as obtained by BJH treatment and secondly using the most probable pore radius obtained by the same treatment $r_0^1 = 2.8\,\text{nm}$ which are significantly different.

Figure 3.11 shows the plot of experimental P_c/P_{sat} values (black dots) obtained from the onset or first point of inflexion and its fit using the modified Kelvin-equation (equation 3.19) for $r_0 = 1.95\,\text{nm}$ (dashed blue line) and $r_0^1 = 2.8\,\text{nm}$ (solid red line), both of which superimpose on each other, arguing of the same (and good) quality of the fit. The measured values of bulk surface tensions at 298 K of TBA:TOL mixture compositions from 0 to 100% were used. Number densities were calculated from mass density values of TBA:TOL mixtures at 298 K as reported in literature[44].

Following the same analysis procedure as for MCM41 materials, the fit of the experimental points for $r_0 = 1.95\,\text{nm}$ gives $\delta \approx 4.5\,\text{Å}$ while for $r_0^1 = 2.8\,\text{nm}$ $\delta \approx 12.9\,\text{Å}$ obtained by keeping $\delta = t + \lambda$ as the fitting parameter and assuming the liquid film on the pore surface to have composition equal to that of adsorbing gas mixture, i.e. y_{TBA}.

Comparing figures 3.10(a) and 3.9, we find that the mass uptake right at the onset of capillary condensation is about 1.4 times greater than the mass uptake at monolayer. Thus, we might interpret the situation just prior to capillary condensation as existence of a liquid film made of one monolayer with more molecules adsorbing over it, which might

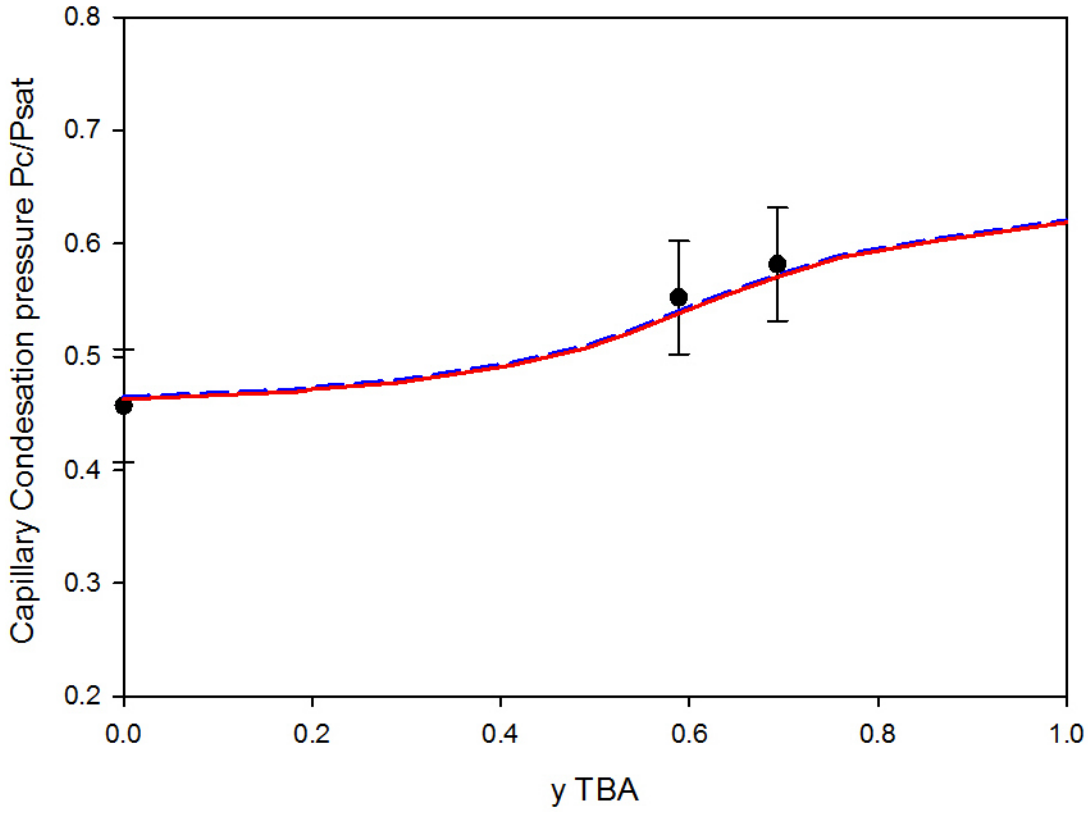

Figure 3.11: Fit of experimentally obtained values of P_c/P_{sat} (black dots along with error bars) fitted by calculated P_c/P_{sat} by the modified Kelvin-equation for $r_0 = 1.95\,\text{Å}$ (dashed blue line) and $r_0^1 = 2.8\,\text{nm}$ (solid red line).

be in the form of capillary bridges linking the adsorbed film across the pore.

Considering $\delta \approx 4.5\,\text{Å}$ which is approximately equal to thickness of a monolayer of TOL $\approx 4.7\,\text{Å}$, then we conclude that λ, the correlation length is nearly zero and the thickness of adsorbed film, $t \approx$thickness of one monolayer. This is incompatible with the fact that mass uptake at the onset of capillary condensation is about 1.4 times greater than at monolayer and the thickness of adsorbed film must account for this additional mass.

On the other hand, considering $\delta \approx 12.9\,\text{Å}$, a value more than twice as much as thickness of a single monolayer, because of the lack of information on the values of t and λ, we examine the situation based on the information that mass uptake is 1.4 times greater at capillary condensation. This means that $t >$ thickness of a monolayer. Thus for $t > 4.7\,\text{Å}$ we obtain $\lambda < 8.2\,\text{Å}$, once again a value probably too high for simple liquids. However if $\lambda \approx 0$, the thickness of film at capillary condensation should be more than twice as much of a monolayer, which is totally in disagreement with experimental observation .

As anticipated already, we confirm that the application of modified-Kelvin equation is unsuitable for interpreting quantitatively the capillary condensation pressure for ad-

sorption in CMK-3, as a broad pore size distribution prevents having one unique capillary condensation, instead a distribution of capillary condensation pressures results into smearing of this step into a smooth transition.

C High Partial Pressure region

Finally we examine the adsorption isotherms at high partial pressures, usually considered the region beyond capillary condensation leading to complete filling of nanopores. Keeping in mind the linear mass increase at the end of adsorption branch is not related to pore filling, we consider the maximum mass uptake for TOL, $x_{TBA} = 0.5$ and $x_{TBA} = 0.7$ to be at $P/P_{sat} = 0.53, 0.65, 0.75$ respectively. The volume porosity known from nitrogen adsorption isotherms based on pores 3.5 nm in diameter is $\approx 0.22\,\mathrm{cm^3\,g^{-1}}$. The volume porosity as calculated from the total amount of TOL adsorbed at the end of adsorption branch, assuming the density of confined TOL equal to its mass density at 25 °C, i.e. $0.861\,\mathrm{g\,cm^{-3}}$ [21] was found to be $\approx 0.264\,\mathrm{cm^3\,g^{-1}}$, which is quite comparable to that obtained from nitrogen isotherm. This corresponds to a porous volume of $V_p = 1.575\,\mu\mathrm{l}$.

From V_p and bulk density of TBA at 25 °C, ($0.7803\,\mathrm{g\,cm^{-3}}$), known from literature[21] we may calculate the mass of TBA adsorbed assuming the porous volume to be completely filled with TBA molecules. Then using equation 3.22 we can estimate the concentration of TBA in the pores at complete filling from final weights of adsorbed mixtures. Figure 3.12 shows the estimated volume fraction of TBA inside the pores as a function of its concentration in the liquid reservoir x_{TBA}. The error bars were estimated based on the error in measurement of initial weight of the dry sample.

We do notice two things here, firstly the volume fraction of TBA in pore matches very well its binary gas concentration (y_{TBA}) for corresponding $x_{TBA} = 0.5$ mixture (liquid reservoir), and secondly the volume fraction of TBA in pore for $x_{TBA} = 0.7$ mixture is apparently equal to pure TBA. Obviously the second observation is unrealistic.

Assuming the composition of adsorbed material in the pores to be the same as its corresponding vapour phase composition i.e. y_{TBA}, we calculate the volume occupied by the adsorbed material from its mass uptake at complete filling and its bulk density at $y_{TBA} = 0.5889$ and $y_{TBA} = 0.6935$ composition to be approximately 1.577 µl and 1.528 µl respectively. If the volume uptake of TOL (1.575 µl) corresponds to 100% of available pore volume, then the % of pore filled for the mixtures is $\approx$ 100% and 97% respectively. Since density of TBA is less than that of TOL, the corresponding mass uptake at complete filling has to be lower for TBA. Therefore values closer to mass uptake of TBA at complete filling will indicate a higher TBA composition. For the $x_{TBA} = 0.7$ mixture, we find the mass uptake at complete filling (1.2247 µg) to be less than the calculated mass uptake of TBA (1.227 µg). This may be attributed to partial filling of pores irrespective of its composition. If the pore composition of this mixture is indeed same as its gas phase, then this partial filling corresponds to 97% of porous volume filled, as calculated above. Although this value is not far from complete pore-filling, its still sufficient to make a difference of few tens of micro-grams in final weight of adsorbed material which is enough to cause significant error in estimation of pore composition owing to very high sensitivity of the technique, thus giving an apparent composition equal to 100% TBA.

On the other hand for the $x_{TBA} = 0.5$ mixture we find the final pore composition

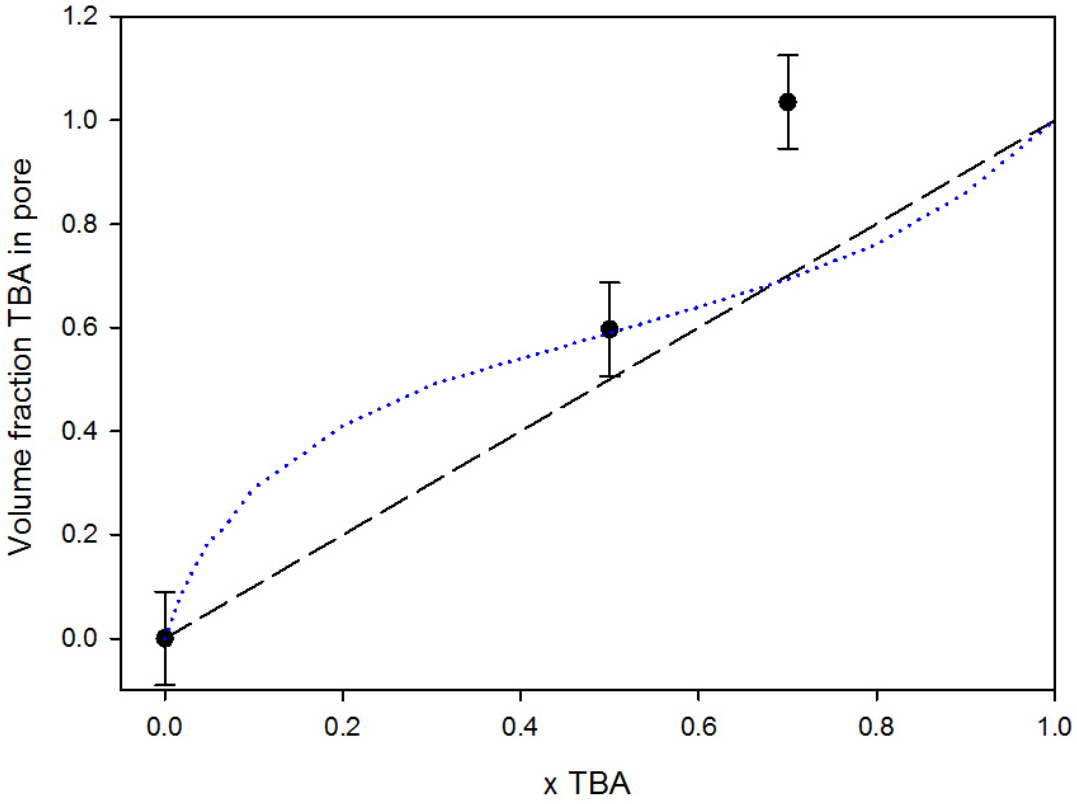

Figure 3.12: Volume fraction of TBA inside the pore at complete filling (black points). The blue dotted line is the corresponding binary gas composition (y_{TBA}), while the black dashed line is a guide for the eye.

to follow the adsorbing binary gas composition, thus being much richer in TBA ($\approx$ 59% TBA) than its corresponding monolayer stage ($\approx$ 21% TBA). This condition necessitates the preferential adsorption of TBA subsequent to monolayer formation. As discussed in the case of adsorption in MCM-41, after coverage of pore surface with first monolayer it loses any specific preference to either TBA or TOL for subsequent adsorption. If that is the case, then the pore composition at complete filling could not be explained by preferentially greater TBA adsorption. Indeed we arrive at the limitation of our method for the calculation of pore composition which necessitates the availability of experimental value of mass uptake for pure TBA. Considering the high sensitivity of this method, an error in estimation of mass uptake simply by calculation from bulk density and porous volume is enough to produce significant error in the final pore composition. At this point, we have to admit that lack of data, i.e. unavailability of experimental mass uptake of pure TBA and more number of mixtures restricts our ability to probe the situation at complete filling reliably as done for MCM-41.

VI Conclusion

The isothermal adsorption of TBA, TOL and their mixtures occurs in three major stages going from lower to higher partial pressures. The high affinity of TBA to adsorb on the solid silica pore-walls in MCM-41 at low partial pressures leads to complete coverage of the pore-surface by a monolayer of TBA even at very small concentration of TBA in the binary gas mixture. This is attributed to the presence of free silanol groups on the pore-surface capable of making hydrogen-bonds with TBA. However a monolayer of TBA modifies the pore-surface as it covers the free silanol groups and it is the methyl groups of TBA instead which face towards the core of the pore.

As partial pressure increases, the incoming TBA and TOL molecules now facing TBA methyl groups do not adsorb so selectively, thus forming the succeeding layer which is a mixture of both TBA and TOL. From the application of modified-Kelvin equation, we find that an approximately two-layer thick film precedes the capillary condensation pressure and that the last layer formed before condensation seems to have lost the memory of the interaction with the silica surface. The strong contrast between the nature of intermolecular forces in the two layers, hydrogen-bonding for TBA attached to pore-surface while Van der Waals interactions for the TBA:TOL mixed layer is seen as the reason for the loss of correlation with the pore wall. The finite pore size prevents natural clustering of TBA molecules as observed in ^1H NMR MAS experiments (section III, chapter 2).

The fit of experimental capillary condensation pressures by the modified-Kelvin equation is compatible with a composition of the adsorbed film at P_c identical to the one of the liquid phase mixture. We attribute this to the non-selective adsorption of the second layer which leads to an average film composition equal to x_{TBA}. The high affinity for TBA continues to exist even at complete pore filling at high partial pressures. We interpret that the TBA monolayer formed at low partial pressures persists even beyond capillary condensation as the volume fraction of TBA in completely filled pores corresponds to that of one monolayer of TBA ($\phi \approx 0.44$) even at very low concentrations in its respective liquid or gas phase mixture. Such self-assembly would essentially leave a toluene-rich core and has been experimentally confirmed by neutron-scattering experiments on TBA:TOL binary liquid mixtures confined in MCM-41[2].

On the other hand, a reversal of adsorption characteristics is observed to a significant extent upon changing the chemical nature of pore wall from hydrophilic to hydrophobic with the use of CMK-3. At low partial pressures, this is confirmed by the analysis of the molecular energy of interaction at the pore wall in the frame of a BET approach. The composition of monolayer is found to be noticeably richer in TOL than its corresponding binary gas/liquid mixture, even though less dramatically when comparing to TBA monolayer concentration on MCM-41 pore surface.

The current chapter thus provides a sound thermodynamic basis to understand the phase separation and structuration of adsorbing gases at the nanoscale based on specific interactions between the adsorbing species and host matrix. Since our discussions so far have been centered on nanoconfined systems at thermodynamic equilibrium, which have been addressed thoroughly, an open question remains whether these fundamentals

of confinement induced phase separation can be extended to a system of nanoconfined binary liquids out of thermodynamic equilibrium, where bulk motion fully miscible binary liquids take places in nanochannels. We answer this question in the next chapter.

Bibliography

[1] Abdel Hamid, A. R., Lefort, R., Lechaux, Y., Moréac, A., Ghoufi, A., Alba-Simionesco, C., and Morineau, D. Solvation effects on self-association and segregation processes in tert-butanol-aprotic solvent binary mixtures. *The journal of physical chemistry. B 117*, 35 (sep 2013), 10221–30.

[2] Abdel Hamid, A. R., Mhanna, R., Lefort, R., Ghoufi, A., Alba Simionesco, C., Frick, B., and Morineau, D. Micro-Phase Separation of Binary Liquids Confined in Cylindrical Pores. *The Journal of Physical Chemistry C* (apr 2016), acs.jpcc.6b01446.

[3] Adiga, S. P., Jin, C., Curtiss, L. A., Monteiro-Riviere, N. A., and Narayan, R. J. Nanoporous membranes for medical and biological applications. *Wiley interdisciplinary reviews. Nanomedicine and nanobiotechnology 1*, 5, 568–81.

[4] Arnold, J. R. Adsorption of Gas Mixtures. Nitrogen-Oxygen on Anatase. *Journal of the American Chemical Society 71*, 1 (jan 1949), 104–110.

[5] Audonnet, F., BrodieâLinder, N., Morineau, D., Frick, B., and Alba-Simionesco, C. From the capillary condensation to the glass transition of a confined molecular liquid: Case of toluene. *Journal of Non-Crystalline Solids* (sep 2014).

[6] Ayappa, K. G. Simulations of Binary Mixture Adsorption in Carbon Nanotubes : Transitions in Adsorbed Fluid Composition. 880–890.

[7] Berezovska, I., Fettaka, H., Salmon, T., Toye, D., and Lodewyckx, P. Redistribution of a mixture of organic vapours inside an activated carbon filter. *Chemical Engineering Journal 280* (nov 2015), 677–681.

[8] Brigo, L., Scomparin, E., Galuppo, M., Capurso, G., Ferlin, M. G., Bello, V., Realdon, N., Brusatin, G., and Morpurgo, M. Mesoporous silica sub-micron spheres as drug dissolution enhancers: Influence of drug and matrix chemistry on functionality and stability. *Materials science & engineering. C, Materials for biological applications 59* (feb 2016), 585–93.

[9] Brocos, P., Amigo, A., and Lemus, M. G. Extended Langmuir Isotherm for Binary Liquid Mixtures. 4261–4266.

[10] Brunauer, S., Emmett, P. H., and Teller, E. Adsorption of Gases in Multimolecular Layers. *Journal of the American Chemical Society 60*, 2 (feb 1938), 309–319.

[11] Celestini, F. Capillary condensation within nanopores of various geometries. *Physics Letters A 228*, 1-2 (mar 1997), 84–90.

[12] Chen, B., Ji, Y., Xue, M., Fronczek, F. R., Hurtado, E. J., Mondal, J. U., Liang, C., and Dai, S. Metal-organic framework with rationally tuned micropores for selective adsorption of water over methanol. *Inorganic chemistry 47*, 13 (jul 2008), 5543–5.

[13] Choy, K. K. H., Porter, J. F., and Mckay, G. Langmuir Isotherm Models Applied to the Multicomponent Sorption of Acid Dyes from Effluent onto Activated Carbon. 575–584.

[14] Coasne, B. *Adsorption and Condensation of Simple Fluids in Mesoporous Silicon : Experiment and Molecular Simulation*. PhD thesis, 2007.

[15] Coasne, B., Alba-Simionesco, C., Audonnet, F., Dosseh, G., and Gubbins, K. E. Adsorption, structure and dynamics of benzene in ordered and disordered porous carbons. *Physical chemistry chemical physics : PCCP 13*, 9 (mar 2011), 3748–57.

[16] Coasne, B., Gubbins, K. E., and Pellenq, R. J.-M. Temperature effect on adsorption/desorption isotherms for a simple fluid confined within various nanopores. *Adsorption 11*, 1 (2005), 289–294.

[17] Costa, E., and Sotelo, J. L. Adsorption Of Binary And Ternary Hydrocarbon Gas Mixtures On Activated Corbon : Experimental Determination And Theoretical Prediction Of The Ternary Equilibrium Data. 5–12.

[18] de Clippel, F., Khan, A. L., Cano-Odena, A., Dusselier, M., Vanherck, K., Peng, L., Oswald, S., Giebeler, L., Corthals, S., Kenens, B., Denayer, J. F. M., Jacobs, P. A., Vankelecom, I. F. J., and Sels, B. F. CO 2 reverse selective mixed matrix membranes for H 2 purification by incorporation of carbonâ??silica fillers. *J. Mater. Chem. A 1*, 3 (2013), 945–953.

[19] Dirir, Y. I., Hanafi, Y., Ghoufi, A., and Szymczyk, A. Theoretical investigation of the ionic selectivity of polyelectrolyte multilayer membranes in nanofiltration. *Langmuir : the ACS journal of surfaces and colloids 31*, 1 (jan 2015), 451–7.

[20] Diu, B. *Éléments de physique statistique*. Collection Enseignement des sciences. Hermann, 1989.

[21] Dumitrescu, V., and Pântea, O. Viscosities of binary mixtures of toluene with butan-1-ol and 2-methylpropan-2-ol. *Journal of the Serbian Chemical Society 70*, 11 (2005), 1313–1323.

[22] Elamin, K., Jansson, H., and Swenson, J. Dynamics of aqueous binary glass-formers confined in MCM-41. *Physical chemistry chemical physics : PCCP 17*, 19 (may 2015), 12978–87.

[23] Formisano, F., and Teixeira, J. Appearance of critical fluctuations in a binary fluid mixture confined in Vycor glass. *Journal of Physics: Condensed Matter 12*, 8A (feb 2000), A351–A356.

[24] Ghassemzadeh, J., Xu, L., Tsotsis, T. T., and Sahimi, M. Statistical Mechanics and Molecular Simulation of Adsorption in Microporous Materials : Pillared Clays and Carbon Molecular Sieve Membranes â . 3892–3905.

[25] Ghoufi, A., Hureau, I., Morineau, D., Renou, R., and Szymczyk, A. Confinement of tert -Butanol Nanoclusters in Hydrophilic and Hydrophobic Silica Nanopores. *The Journal of Physical Chemistry C 117*, 29 (jul 2013), 15203–15212.

[26] Guo, X.-Y., Watermann, T., and Sebastiani, D. Local microphase separation of a binary liquid under nanoscale confinement. *The journal of physical chemistry. B 118*, 34 (aug 2014), 10207–13.

[27] Hansen, R. S., Fu, Y., and Bartell, F. E. Multimolecular Adsorption from Binary Liquid Solutions. *The Journal of Physical and Colloid Chemistry 53*, 6 (jun 1949), 769–785.

[28] Hydrogen-chabazite, I. G., Roy, P., and Lond, S. O. C. Vacancy Solution Theory of Adsorption From Gas Mixtures.

[29] Kadam, A. A., Karbowiak, T., Voilley, A., and Debeaufort, F. Techniques to measure sorption and migration between small molecules and packaging. A critical review. *Journal of the Science of Food and Agriculture 95*, 7 (may 2015), 1395–1407.

[30] Karan, S., Jiang, Z., and Livingston, A. G. MEMBRANE FILTRATION. Sub-10 nm polyamide nanofilms with ultrafast solvent transport for molecular separation. *Science (New York, N.Y.) 348*, 6241 (jun 2015), 1347–51.

[31] Kusalik, P. G., Lyubartsev, A. P., Bergman, D. L., and Laaksonen, A. Computer Simulation Study of tert -Butyl Alcohol. 1. Structure in the Pure Liquid. *The Journal of Physical Chemistry B 104*, 40 (oct 2000), 9526–9532.

[32] Langmuir, I. The adsorption of gases on plane surfaces of glass, mica and platinum. *Journal of the American Chemical society 40*, 9 (1918), 1361–1403.

[33] Lerbret, A., Lelong, G., Mason, P. E., Sabougni, M.-L., and Brady, J. W. Molecular dynamics and neutron scattering study of glucose solutions confined in MCM-41. *The journal of physical chemistry. B 115*, 5 (feb 2011), 910–8.

[34] Li, G., Xiao, P., and Webley, P. Binary adsorption equilibrium of carbon dioxide and water vapor on activated alumina. *Langmuir : the ACS journal of surfaces and colloids 25*, 18 (sep 2009), 10666–75.

[35] Li, M., Xu, E., Wang, T., and Liu, J. Adsorption equilibria of binary gas mixtures on graphitized carbon black. *Langmuir : the ACS journal of surfaces and colloids 28*, 5 (mar 2012), 2582–8.

[36] Maddox, M. W., Sowers, S. L., Gubbins, K. E., and Hall, O. Molecular Simulation of Binary Mixture Adsorption in Buckytubes and MCM-41. 23–32.

[37] Martínez-Soria, V., Peña, M. P., and Montón, J. B. Vapor-Liquid Equilibria for the Binary Systems tert -Butyl Alcohol + Toluene, + Isooctane, and + Methylcyclohexane at 101.3 kPa. *Journal of Chemical & Engineering Data 44*, 1 (1999), 148–151.

[38] Mieczyslaw, B. Y. Statistical Thermodynamics of Mixed-Gas Adsorption. 933–938.

[39] Mohammad, A., Teow, Y., Ang, W., Chung, Y., Oatley-Radcliffe, D., and Hilal, N. Nanofiltration membranes review: Recent advances and future prospects. *Desalination 356* (nov 2014), 226–254.

[40] Myers, A. L. Rigorous Thermodynamic Treatment of Gas Adsorption. 1887–1893.

[41] Myers, A. L. Thermodynamics of Adsorption in Porous Materials.

[42] Myers, A. L., and Prausnitz, J. M. Thermodynamics of Mixed-Gas Adsorption. 121–127.

[43] NAGY, L., and SCHAY, G. ADSORPTION OF BINARY LIQUID MIXTURES ON SOLID SURFACES - THERMODYNAMICAL DISCUSSION OF ADSORPTION EQUILLIBRIUM .1. *ACTA CHIMICA ACADEMIAE SCIENTARIUM HUNGARICAE 39*, 3 (1963), 365–&.

[44] Nikam, P. S., Jagdale, B. S., Sawant, A. B., and Hasan, M. Densities and Viscosities of Binary Mixtures of Toluene with Methanol, Ethanol, Propan-1-ol, Butan-1-ol, Pentan-1-ol, and 2-Methylpropan-2-ol at (303.15, 308.15, 313.15) K. *Journal of Chemical & Engineering Data 45*, 4 (jul 2000), 559–563.

[45] Park, J. Extension of the Brunauer-Emmett-Teller Equation to Mixtures. *Journal of Chemical Engineering of Japan 48*, 11 (nov 2015), 927–932.

[46] Pasinetti, P. M. A semiempirical model for adsorption of binary mixtures. *Physical Chemistry Chemical Physics 16* (2014), 24063–24068.

[47] Pellenq, R. J.-M., Coasne, B., Denoyel, R. O., and Coussy, O. Simple Phenomenological Model for Phase Transitions in Confined Geometry. 2. Capillary Condensation/Evaporation in Cylindrical Mesopores. *Langmuir 25*, 3 (feb 2009), 1393–1402.

[48] Pen, M. P., Monto, J. B., Quimica, D. D. I., Quimica, F. D., and Valencia, U. D. Vapor - Liquid Equilibria for the Binary Systems tert -Butyl Alcohol + Toluene , + Isooctane , and + Methylcyclohexane at 101 . 3 kPa Vicente MartÄ? 148–151.

[49] Pérez-Esteve, É., Ruiz-Rico, M., de la Torre, C., Villaescusa, L. A., Sancenón, F., Marcos, M. D., Amorós, P., Martínez-Máñez, R., and Barat, J. M. Encapsulation of folic acid in different silica porous supports: A comparative study. *Food Chemistry 196* (apr 2016), 66–75.

[50] Poling, B. E., Prausnitz, J. M., and O'Connell, J. P. Constants for the Antoine Equation for Vapour Pressures of Pure Species, 2001.

[51] Rao, M. B., and Sircar, S. Thermodynamic Consistency for Binary Gas Adsorption Equilibria. *Langmuir 15*, 21 (oct 1999), 7258–7267.

[52] Science, N. Binary Langmuir and Freundlich Isotherms for Ideal Adsorbed Solutions. 3247–3250.

[53] Siperstein, F. R., and Myers, A. L. Mixed-Gas Adsorption. 1141–1159.

[54] Sumida, K., Rogow, D. L., Mason, J. A., Mcdonald, T. M., Bloch, E. D., Herm, Z. R., Bae, T.-h., and Long, R. Carbon Dioxide Capture in Metal À Organic Frameworks. 724–781.

[55] Tanaka, H. Double phase separation in a confined, symmetric binary mixture: Interface quench effect unique to bicontinuous phase separation. *Physical Review Letters 72*, 23 (jun 1994), 3690–3693.

[56] Thielmann, F., Butler, D., Williams, D., and Baumgarten, E. *Characterisation of microporous materials by dynamic sorption methods*, vol. 129 of *Studies in Surface Science and Catalysis*. Elsevier, 2000.

[57] Wang, Y., Tsotsis, T. T., and Jessen, K. Competitive Sorption of Methane/Ethane Mixtures on Shale: Measurements and Modeling. *Industrial & Engineering Chemistry Research 54*, 48 (dec 2015), 12187–12195.

[58] Xu, Y., Zhu, H., and Yang, L. Estimation of Surface Tension of Ionic Liquid-Cosolvent Binary Mixtures by a Modified Hildebrand-Scott Equation. *Journal of Chemical & Engineering Data 58*, 8 (aug 2013), 2260–2266.

[59] Yin, J., Kim, E.-S., Yang, J., and Deng, B. Fabrication of a novel thin-film nanocomposite (TFN) membrane containing MCM-41 silica nanoparticles (NPs) for water purification. *Journal of Membrane Science 423-424* (dec 2012), 238–246.

[60] Yun, J. H., Düren, T., Keil, F. J., and Seaton, N. A. Adsorption of Methane, Ethane, and Their Binary Mixtures on MCM–41: Experimental Evaluation of Methods for the Prediction of Adsorption Equilibrium. *Langmuir 18*, 32 (2002), 2693–2701.

[61] Zhang, Y., Wei, S., Liu, F., Du, Y., Liu, S., Ji, Y., Yokoi, T., Tatsumi, T., and Xiao, F. S. Superhydrophobic nanoporous polymers as efficient adsorbents for organic compounds. *Nano Today 4*, 2 (apr 2009), 135–142.

4

Spontaneous imbibition of binary liquids into a nanoporous network

I Scientific background and motivation

In the last two chapters we discovered systematically about the existence of hydrogen-bonding interactions between TBA and silica surface from the chemical shifts in ^{1}H MAS NMR spectra of mixtures. We show semi-quantitatively using a thermodynamic model that the strong affinity of silica surface for TBA leads to its preferential adsorption when adsorbing a binary gas mixture of TBA and TOL at low relative pressures, while at complete filling of pores by binary liquid mixture such hydrogen bonding interactions in silica nanopores leads to phase separation of TBA:TOL mixtures into a shell of TBA-monolayer attached to the silica wall encompassing a core of TBA:TOL mixture, highly rich in TOL. However we must note that such phenomena were observed under conditions of thermodynamic equilibrium.

Based on these findings we extend the discussion to systems out of thermodynamic equilibrium, i.e. investigating if such hydrogen-bonding interactions between silica surface and TBA has the potential to affect flow properties of TBA:TOL mixtures through silica nanopores.

The method of choice was spontaneous imbibition of our binary liquid mixtures into silica nanopores. Liquid uptake by porous materials is a regular occurrence in our daily lives, for example coffee getting soaked into a cube of sugar, a dry cloth or sponge soaking up water from surface, uptake of water by plants through their roots and so on. This phenomenon known as spontaneous imbibition is driven purely by viscous forces without any applied external pressure leading to a capillary-rise action into the porous network which is effectively a collection of capillaries. An essential condition for occurrence of spontaneous imbibition is that the surface of porous material must be highly wetting towards the liquid to be imbibed, i.e. the contact angle between liquid and surface of pore wall must be less than 90°. As discussed in the previous chapter, contact angle θ_c measurements of TBA, TOL and their mixtures were carried out on silica surface and it was found that $\theta \approx 0°$ for most mixtures. Thus silica surface is highly favourable for imbibition of TBA:TOL mixtures.

As discussed in the chapter 1 (introduction), the porous substrate of choice was a monolithic nanoporous silica called Vycor, chosen for its thermo-mechanical and chemical stability as well the possibility of being carved into precise geometric shapes, which is imperative for quantitative studies of fluid dynamics.

In the current chapter spontaneous imbibition has been investigated by two different approaches, the first one is a gravimetric method where mass uptake of a Vycor block is studied as a function of time when imbibing the binary liquid mixtures from a reservoir. In the second technique, its the rise level of liquid inside the porous block which is monitored as a function of time using neutron radiography technique, the choice of which is centred on the possibility to tune the contrast of liquid being imbibed by deuterating either of the mixture components to enable both visual identification and quantitative analysis of any multicomponent flow that may arise due to confinement induced phase separation.

II Fundamentals of spontaneous imbibition

We recall again the concepts discussed previously in the introduction chapter (section B) regarding dynamics of spontaneous imbibition of a liquid in nanopores. The mass uptake of a porous block and the respective rise in liquid level inside it for pure liquids is given by the equation 4.1 and 4.2 from the Lucas-Washburn law.

$$m(t) = \rho A \sqrt{\frac{\phi_a \sigma \cos\theta}{2\eta}} I \sqrt{t} \tag{4.1}$$

$$h(t) = \sqrt{\frac{\sigma \cos\theta}{2\phi_a \eta}} I \sqrt{t} \tag{4.2}$$

Where ρ is the mass density, σ the surface tension, η the bulk viscosity, ϕ_a the apparent porosity of block, θ the contact angle between the liquid meniscus and pore wall, A is the cross-sectional area of block perpendicular to the axis of liquid rise and I is the Imbibition strength given by equation 4.3

$$I = \frac{r_h^2}{r} \sqrt{\frac{\phi_0}{r_L \tau}} \tag{4.3}$$

Where r_h and r_L are known as the hydrodynamic pore radius and Laplace radius respectively. r_h is associated to the stick and slip flow of liquids through pores[3] and is the radial distance from centre of pore to the point where velocity of liquid layers is equal to zero. r_L is the reduced radius of the pore due to formation of pre-adsorbed water layer(s) due to ambient humidity. I is fundamental to a porous matrix and derives from its topology and pore-architecture, being independent of the liquid imbibed.

The measure of imbibition dynamics is thus obtained from the proportionality constant C_M and C_H, betweern mass uptake versus $\sqrt{t}$ and liquid rise level versus $\sqrt{t}$ given by equations 4.4 and 4.5 respectively.

$$C_M = \rho A \sqrt{\frac{\phi_a \sigma \cos\theta}{2\eta}} I \tag{4.4}$$

$$C_H = \sqrt{\frac{\sigma \cos\theta}{2\phi_a \eta}} I \tag{4.5}$$

Imbibition dynamics of pure liquids in nanopores have already been shown to be well predicted by the Lucas-Washburn law. The evidence of phase-separation in TBA:TOL mixtures confined in silica nanopores in equilibrium conditions owing to hydrogen-bonding interactions between TBA and silica surface prompts us to question if this preferential interaction for one component over the other might give rise to a two-component flow with separate dynamics as the concept of bulk physical properties of mixtures, i.e. a unique surface tension, viscosity and density for a given mixture composition may no longer apply, eventually leading to a deviation from Lucas-Washburn dynamics. In the following sections we find out answers to these questions raised.

III Experiments and results

In the following section are discussed the two major experiments carried out in order to characterize rise dynamics of TBA:TOL mixtures in Vycor by (i) mass rise as a function of time, referred to here as gravimetric technique, and (ii) observing rise of liquid level in the block as a function of time by neutron radiography. Two Vycor blocks with slightly different pore characteristics were used for the two experiments respectively owing to their availability at the time of experiment. The following work was carried out under the guidance and supervision of Prof. Dr. Patrick Huber, partly at the Institute of Materials Physics and Technology at the Hamburg University of Technology (TUHH, Hamburg, Germany) and part at the French Neutron source for research, Laboratoire Léon Brillouin (Saclay, France). The following sections discuss in detail the experimental setup, conditions and their respective results.

A Spontaneous imbibition study through gravimetry

Figure 4.1 shows the experimental setup used..

The sample used was a Vycor block ($0.9 \times 0.8 \times 1.25$cm) with pore radius $r = 4.54\,$nm and a volume porosity of $\phi_0 = 0.32$.The block is suspended into a glass beaker from the top using an easily malleable metal wire glued to the top of the block using a two-part epoxy glue. A fast drying epoxy glue ($< 2\,$min) was used in order to achieve fast polymerization and prevention of any glue component entering into the pores. The glass beaker serves as a reservoir of the liquid mixtures. This is a slight modification over the original setup which used a metallic cell to enclose both the sample and liquid reservoir in order to provide a closer temperature control. Due to high vapour pressure of TBA and TOL, position of the suspended Vycor block inside such closed cell was found to be very unstable, thus giving lot of fluctuations in the readings of its mass. As a result, the glass beaker with an open top was found to be a practical solution to this problem.

Adsorption from the gas phase leading to pore filling by capillary condensation[11] is also another concern while working with high vapour pressure liquids. Thus it was imperative to seal all sides of the Vycor block with the same fast drying epoxy glue, except the bottom of block in contact with the liquid reservoir, in order to allow imbibition only from the bottom while preventing pore filling by adsorption from sides.

In figure 4.1, the cross-section parallel to vertical axis of the block is shown only for clarity. The chemical resistance of this epoxy glue to TOL and TBA:TOL mixtures was tested prior to use by coating a test Vycor block with the glue and keeping it submerged inside these solvents (TOL, TBA:TOL mixtures) for several hours. No physical or chemical changes on the glue, such as swelling, cracking or degradation were noticed, thus clearing out to be fit for the experiment. A cantilever mechanism with adjustable height was used to raise the beaker partially filled with the desired liquid to touch the bottom of Vycor block. Once in contact, the liquid is taken up by the porous matrix instantaneously

giving rise to increase in weight of the block as a function of time $m(t)$ which is recorded live into a text file at a time-interveral of every 2 s. The following section describes more about the specific experimental details.

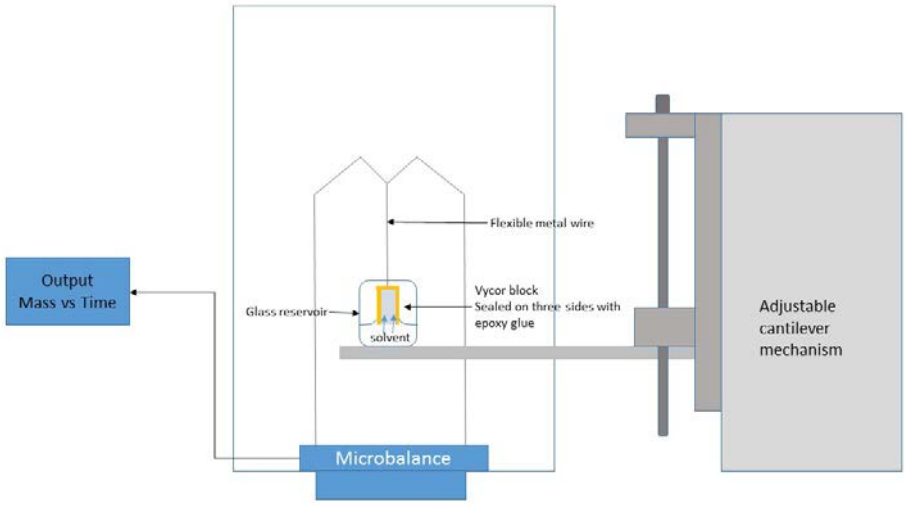

Figure 4.1: Schematic diagram of the experimental setup for studying spontaneous imbibition of TBA:TOL mixtures through Vycor by gravimetry

A.1 Experiment

A 50 ml glass beaker was used for the experiment which was filled with 10 ml of the liquid to be imbibed. The liquids used were pure TOL and a series of mixtures with increasing TBA concentration from $\%TBA = 10$ (by volume) to $\%TBA = 90$. The experiments were carried out at room temperature ($\approx 25(2)\,^{\circ}\mathrm{C}$). However considering the relatively small effect of temperature on bulk physical properties of TB:TOL mixtures, i.e. their viscosity, surface tension and density even within a temperature range of 5 °C[5,14], we do not expect any significant changes in the imbibition dynamics from small temperature fluctuations during the experiment. However imbibition of pure TBA was not possible at this temperature because of its tendency to crystallize.

Prior to beginning each experiment, the Vycor block was heated at 65 °C for 48 hours in an oven which is sufficient to remove the TBA and TOL molecules adsorbed in the pores. However it is hard to comment if it removes pre-adsorbed layer(s) of water effectively stuck to pore walls or not. Since there exist no specific technique to monitor the removal of adsorbed solvents or pre-adsorbed water upon drying, the practical solution to judge whether the pores properly emptied was to measure the weight of block. One must note that the weight of block now is inclusive of glue layers sealing its surface as well as the metallic wire glued to its top. Thus achieving the same initial weight at the beginning

of each experiment ensures that we are starting with a completely empty porous matrix, at least theoretically.

As the liquid reservoir is raised gradually, at some point the block's bottom surface comes in contact with the liquid surface. At this point, the apparent mass of the sample falls suddenly. This happens due to the upward buoyant force exerted by the liquid on the block, causing it to appear lighter suddenly. Instantaneously after this, mass of the block starts to increase as the liquid mixture starts penetrating inside the pores. We denote the initial mass of the sample as m_i and the apparent initial mass right after coming in contact with the liquid surface as m_i^a. Thus the mass gain $m(t)$ is recorded with respect to m_i^a. As the imbibition process continues $m(t)$ keeps increasing and plateau's after a certain time indicating complete filling of the porous matrix, such that mass of the sample no more increases.

The liquid is then slowly lowered to free the sample from it and as their contact breaks we notice a quick increase in mass of the completely filled sample as it is freed from the buoyant force acting on it. The final mass of the block is noted as its mass at the point when its breaks contact with the liquid reservoir, ensuring that there exists no attached drop of liquid at the bottom of block. The mass uptake can be simply calculated as follows.

$$\Delta m = m_f - m_i$$

A systematic study of imbibition of liquid mixtures from %TBA=0 (i.e.pure TOL) to %TBA=90 was carried out and their results are discussed in the following section.

A.2 Results

Figure 4.2 shows the mass uptake versus time for imbibition of pure TOL. We observe that even after complete filling of the block, its mass continues to rise linearly with time before it reaches a brief plateau and then drops suddenly as the liquid reservoir is physically lowered breaking contact between the liquid surface and Vycor block.

The apparent mass uptake of block has two contributions, (i) filling of porous matrix by imbibing liquid leading to mass rise of the block (ii) decrease of buoyant force exerted by the liquid on the block due to the volatile nature of TBA:TOL mixtures causing a gradual lowering of liquid meniscus surrounding the bottom of Vycor block, in other words decreasing the volume of block submerged inside the liquid during course of experiment. Although this lowering is not fast enough to cause a break of contact between the liquid and porous block in the time scale of experiments, lowering of its level does lead to gradual decrease in volume of block immersed in the liquid. This results into a sustained lowering of the upward buoyant force from the liquid, or in other words increase in apparent mass of the sample.

It was found that after correcting the mass rise for the additional linear mass rise (figure 4.2) due to falling liquid meniscus we arrive to the $\sqrt{t}$ dependence of mass rise as predicted by equation 4.1 with mass uptake plateauing at complete filling of block, just

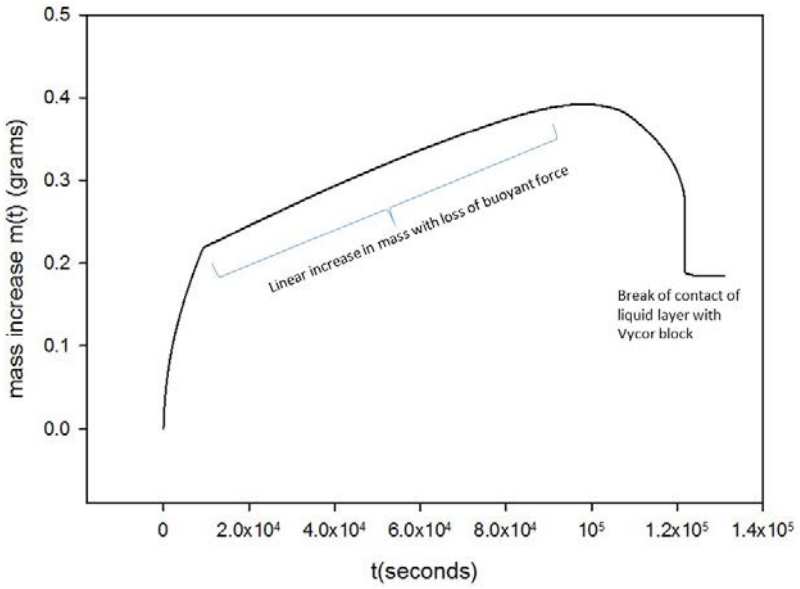

Figure 4.2: m(t) versus time showing the apparent mass increase caused due to lowering of meniscus leading to reducing buoyant force or increased apparent mass rise

as would be expected. In figure 3.6, the mass uptake $m(t)$ has been shown for different concentrations as a function of $\sqrt{t}$ for simplicity.

An important concern here is the decrease in initial porosity of the porous matrix due to pre-adsorbed water layers. Although there was no direct way of determining the initial porosity ϕ_a, it was possible to calculate it from the mass of liquid taken up by the Vycor block at complete filling.

$$\phi_a = \frac{\Delta m}{\rho V_{block}}$$

Where, Δm is the mass of liquid taken up and ρ is its density and V_{block} is volume of the Vycor block ($0.9\,\mathrm{mm}^3$). Assuming that the completely filled Vycor block has the exact same composition as the liquid reservoir, we find $\phi_a = 0.274 \pm 0.005$ with no correlation to composition of the mixture imbibed. It is thus possible to calculate the Laplace radius r_L from ϕ_a by assuming the pores to be cylindrical by the following formula.

$$r_L = r\sqrt{\frac{\phi_a}{\phi_0}}$$

We find $r_L = 4.2\,\mathrm{nm}$. Thus the thickness of pre-adsorbed layer is

$$t = r - r_L = (4.54 - 4.2)\mathrm{nm} = 3.4\,\text{Å}$$

This corresponds roughly to the thickness of a monolayer of water[7,9].

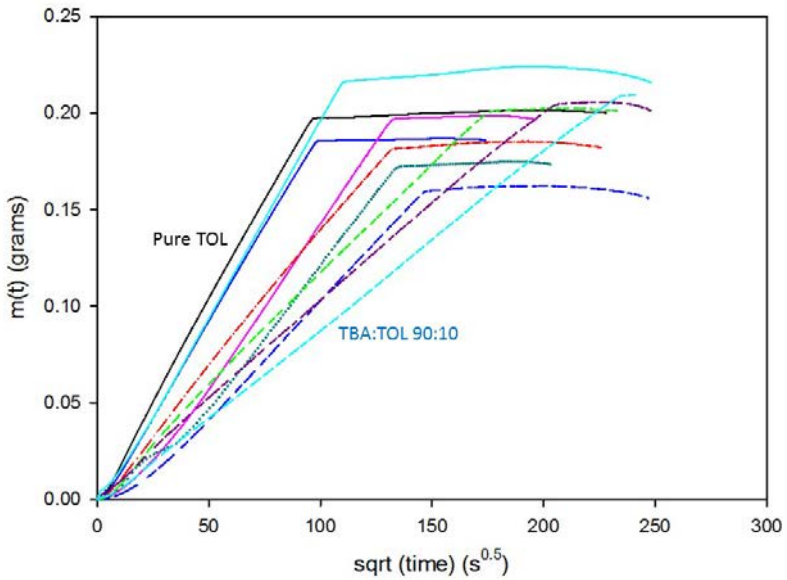

Figure 4.3: m(t) versus $\sqrt{t}$ curves of all the concentrations measured between pure TOL and $\%TBA = 90$. The colour code for the curves is as follows solid black:TOL,solid blue: $\%TBA = 10$, solid cyan: $\%TBA = 20$, solid pink: $\%TBA = 30$, dotted: $\%TBA = 40$, dashed red: $\%TBA = 50$, dashed blue: $\%TBA = 60$, dashed green: $\%TBA = 70$, dashed violet: $\%TBA = 80$, dashed cyan: $\%TBA = 90$

Having known the reduced porosity of the Vycor block we are able to calculate the imbibition strength I for imbibition of TOL from equation 4.1 as follows.

$$I = \frac{1}{\rho A}\sqrt{\frac{2\eta}{\phi_i \sigma \cos\theta_0}}$$

The slope of $m(t)$ versus $\sqrt{t}$ in figure 4.3 gives us the pre-factor C_M of equation 4.1. $\cos\theta_0 \approx 1$ since the contact angle $\theta_0 \approx 0$ as found from contact-angle measurements of TBA:TOL mixtures on silica surface.

We find $I = 1.325 \times 10^{-5}\sqrt{\text{m}}$ which is well in agreement with the known imbibition strengths of Vycor materials[9]. It is important to note that I is a property associated with the structural characteristics of the solid matrix and the value obtained is constant irrespective of the liquid imbibed. From the known values of density, surface tension and viscosity of bulk TBA:TOL liquid mixtures at 25 °C in the reservoir and constant values of A, ϕ_a and I, we calculated the value of the imbibition coefficient C_M^{calc} using equation 4.1 and compared them to ones obtained from the slope $m(t)$ vs $t^{1/2}$ fits from figure 4.3 (C_M^{exp}) as shown in figure 4.4.

We find here that the values of C_M^{exp} vary similarly as C_M^{calc} with TBA concentration with some fluctuations, while no general trend of deviation between the two sets of values could be noticed. We also calculate the final mass of liquid mixture taken up by the Vycor

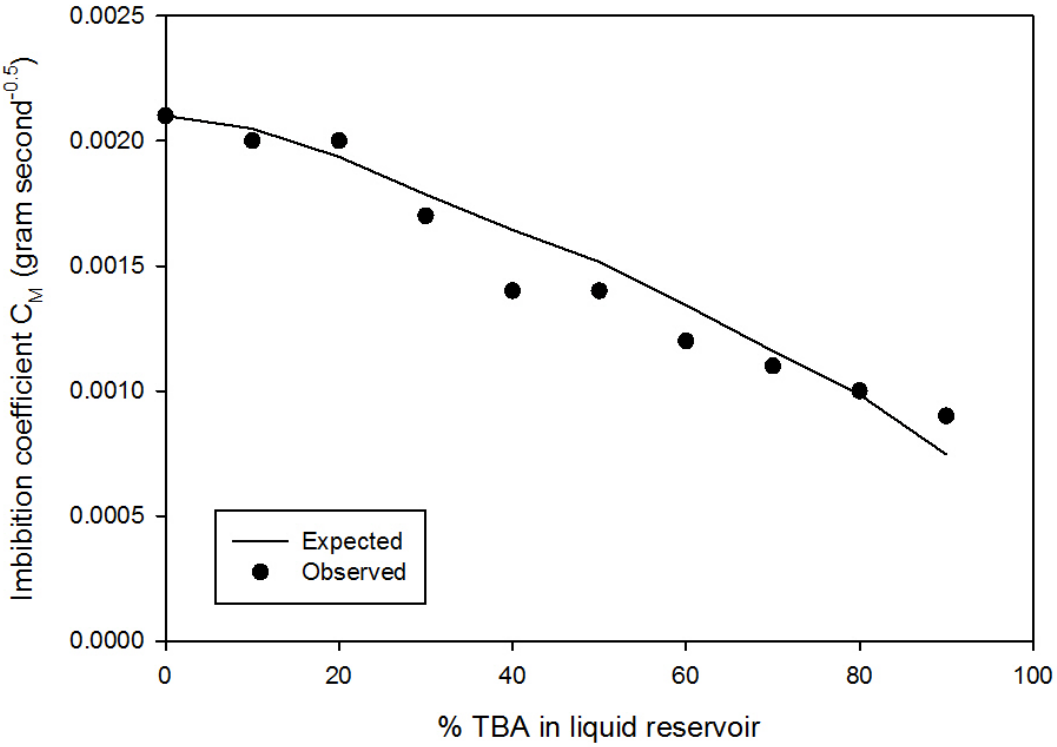

Figure 4.4: Comparison of C_M^{calc} values calculated (solid black line) from bulk physical properties (ρ,ϕ_a and σ) with C_M^{exp} values obtained from fitting of the $m(t) vs \sqrt{t}$ curves (black dots)

block using the corresponding bulk densities of the mixtures and assuming the composition of liquid mixture inside the pores to be same as in the reservoir at complete filling by using equation 4.6 and compare them with the experimental values of $\Delta m^{exp} (= m_f - m_i)$ as shown in figure 4.5.

$$\Delta m^{calc} = \phi_a \times V_{block} \times \rho \tag{4.6}$$

The final mass uptake from experiment follows a similar trend with TBA concentration as expected by calculation with some fluctuations around it indicating that the mixture composition inside the pores is nearly the same as its corresponding composition in the liquid reservoir. Such fluctuations of experimentally obtained values from their corresponding calculated values both for (C_M^{exp}) and Δm^{exp} may be attributed to small temperature differences between individual experiments, difference in vapour pressures between TBA and TOL which might lead to modification in the reservoir composition and slight differences in initial porosity ϕ_a of the Vycor block.

We find here that the Lucas-Washburn approach works very well even for a mixture,

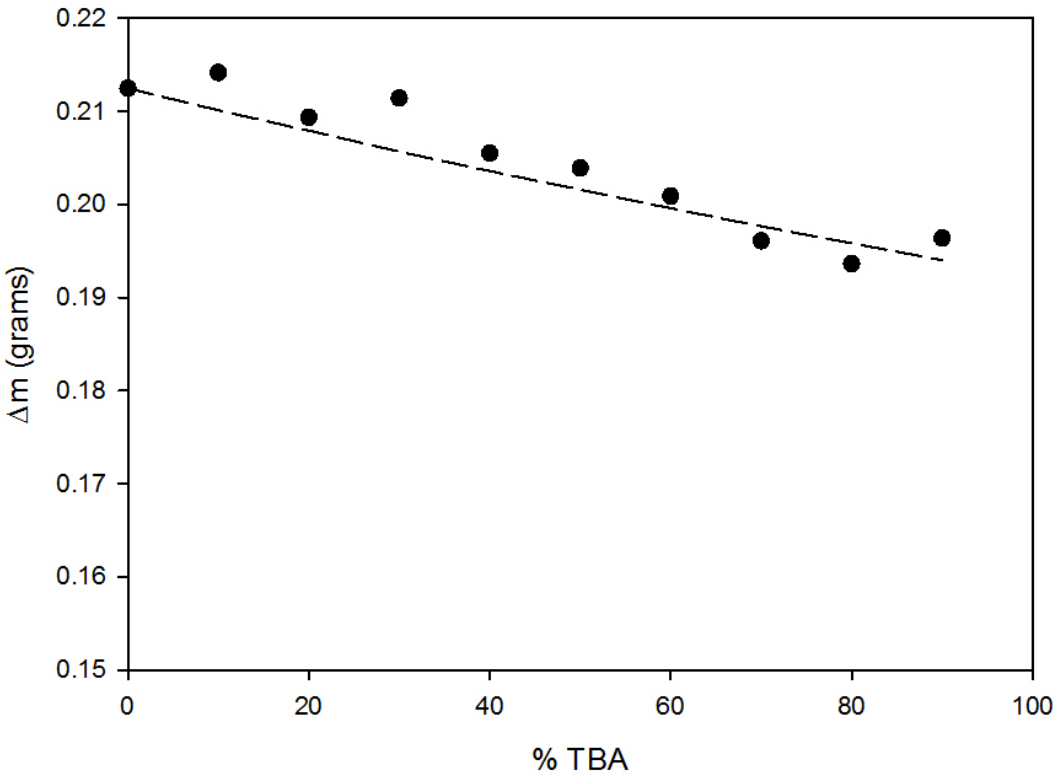

Figure 4.5: Comparison of the final masses of liquid mixtures taken up by the Vycor block at complete filling. The dashed line gives Δm^{calc}, which is the expected mass gain from densities of bulk TBA:TOL mixtures. Δm_{exp} is calculated from the difference in initial and weight (complete filling) of the sample outside liquid reservoir

assuming it to be a homogeneous liquid having average properties (density, viscosity, surface tension) of the bulk liquid mixtures without any demixion. In the next section we approach the spontaneous imbibition of TBA:TOL mixtures using a technique which can enable us to qualitatively and quantitatively examine the rising imbibition front and clarify whether it is actually a homogeneous liquid following its corresponding reservoir composition or not.

B Spontaneous imbibition study through neutron radiography

In the current section we investigate the dynamics of imbibition of TBA:TOL mixtures into Vycor through an imaging technique which provides us space and time resolved information of the process. The use of x-rays for tomographic and imaging purposes is already very prevalent. However, x-rays are less sensitive to small atomic number molecules such as hydrogen, carbon, oxygen and nitrogen because of their low electron density which results into a low scattering cross-section.

The use of neutrons provides much better solution to investigate soft matter as they interact directly with the nucleus of an element and the scattering/absorption cross-section is independent of the electronic density and thus the atomic number of an element. The exclusive advantage which comes with neutrons is the difference in scattering/absorption cross-section between two isotopes of the same element, for example $\sigma_{1H}^{scatt} = 82.03\,\mathrm{b}$, while $\sigma_{2H}^{scatt} = 7.64\,\mathrm{b}$[15]. This helps to tune the contrast between two hydrocarbons mixed with each other by simply deuterating one, without the risk of modifying its chemical nature.

In the context of radiography, differentiating one material from the other depends upon their relative transmissions to the incoming neutron beam. The transmission T of a material with thickness d which is basically the ratio of final intensity of transmitted neutron beam to its initial intensity $\left(\frac{I}{I_0}\right)$ is calculated by the Beer-Lambert Law.

$$T = \frac{I}{I_0} = e^{-(\rho\sigma_{total})d}$$

Where ρ, σ_{total} are the molecular density (molecules/cm^3) and total scattering cross-section respectively, their product known as the total scattering-length density (SLD). The total SLD of a sample is calculated by the formula

$$SLD_{total} = SLD_{scatt} + SLD_{Abs} = \rho\sigma_{scatt} + \rho\sigma_{Abs}$$

Where SLD_{scatt} and SLD_{Abs} are the scattering length densities for the scattering and absorption processes respectively. From the known scattering and absorption cross-sections of ^{28}Si,^{16}O,^{12}C,^{1}H and ^{2}H[15] the transmissions of Vycor, hydrogenated TOL, TBA denoted here by TOL-H, TBA-H and deuterated TOL, denoted by TOL-D through a thickness of 1 cm were calculated for comparison and the result was as follows.

$$T_{tolH} = 0.961$$
$$T_{tol-D} = 0.994$$
$$T_{tba-H} = 0.948$$
$$T_{Vycor} = 0.998$$

Thus we find that Vycor is nearly transparent to neutrons, making it possible to observe the liquids rising inside upon imbibition owing to their lower transmittance. This situation however during a radiography experiment leads to a transmittance composed of two contributions, one from Vycor and the other from imbibing liquid whose position changes with time, resulting in a time dependent transmission given by.

$$T_{imb}(t) = e^{-(\rho_v\sigma_v + \rho_{mix}\sigma_{mix}^{(t)})d} \tag{4.7}$$

Where $T_{imb}(t)$ is the time-dependent transmission of the Vycor block getting constantly filled with the mixtures, ρ_v, σ_v are the number density and total scattering cross-section of the Vycor block while ρ_{mix} and $\sigma_{mix}^{(t)}$ are the density and time-dependent scattering cross-section of the rising liquid, its time-dependence being related to its change of height. Application of such time-dependent transmissions to understand flow dynamics of TBA:TOL mixtures would be discussed more in detail later in this section.

B.1 Experiment

The experiments were carried out at the neutron imaging station "IMAGINE" of the French neutron source for research, Laboratoire Léon Brillouin (LLB) in Saclay, France. Located at the cold neutrons guide G3bis, the wavelength of available neutron beam ranges between 0.3-2 nm with a flux of 2×10^7 neutrons/ sec /cm^2. A sCMOS camera (Photonics Science) coupled to lithium scintillators of 50-100 mm thickness was used for detection which in principle provide a resolution of up to 100 µm.

The Vycor block used in these experiments is noted as V5, its radius and porosity being $r = 3.4\,\text{nm}$ and $\phi_0 = 0.32$ respectively. Figure 4.6 shows the setup for the imbibition experiment studied by neutron radiography. A cuboid shaped Hellma cell made of quartz was used as a reservoir of the liquid mixture to be imbibed. An aluminium holder with slots made to hold the Vycor blocks was placed on top of the Hellma cell, thus covering it and converting into a closed container, thus slowing down the loss of liquid inside the reservoir due to evaporation. The liquid in Hellma cell was filled up to the level that it just touches the base of Vycor block, whose position was fixed. The entire system was placed on a rotatable platform, whose height could be adjusted as well. The Hellma cell was placed perpendicular to the incoming neutron beam. The aluminium sample holder was used because of its high transmission to neutrons. For the same reason, the Vycor sticks were sealed on all sides with aluminium tape to avoid pore-filling from the gaseous phase, while staying quite transparent to incoming neutrons at the same time. The top section of Vycor blocks was sealed with an epoxy glue, while the bottom was left free for the liquids to penetrate into the block. A sheet of cadmium was used to cover up most of the aluminium exposed to neutrons in order to prevent unwanted scattering and protecting it from radioactive activation.

Prior to starting the experiment, the Vycor block was dried under vacuum for 4-5 hours at 70 °C.The sample set had to be kept small due to the short period of time available for the experiments in comparison to the time taken for completion of a typical imbibition experiment (6-20 hours) and preparation for the next one. The chosen liquids being pure TOL-H, TBA-H:TOL-H 50:50 (by volume), TBA-H:TOL-D 50:50 and TBA-H:TOL-H 90:10. The aim of using deuterated TOL in one of the mixtures was to achieve a contrast of the mixture where in the event of any phase separation, the contribution of pure TOL would be masked as TOL-D has a much smaller absorption cross-section.

The kinetics of imbibition experiment was captured as series of images, each exposed to the neutron beam for a fixed period of 3 minutes and a time period of 3 minutes between each image exposure. Figure 4.7 shows the image of a typical experiment. Comparing it with figure 4.6 we can easily locate all the components of setup. In figure 4.7 we observe the position of liquid front can be located easily.

For a quantitative treatment, the images were analysed using ImageJ software. To improve resolution, the image was cropped to cover only the Vycor block along with some additional space left around it. We can re-write the transmission of the system during an imbibition experiment from equation 4.7 as a product of two transmissions, one of the

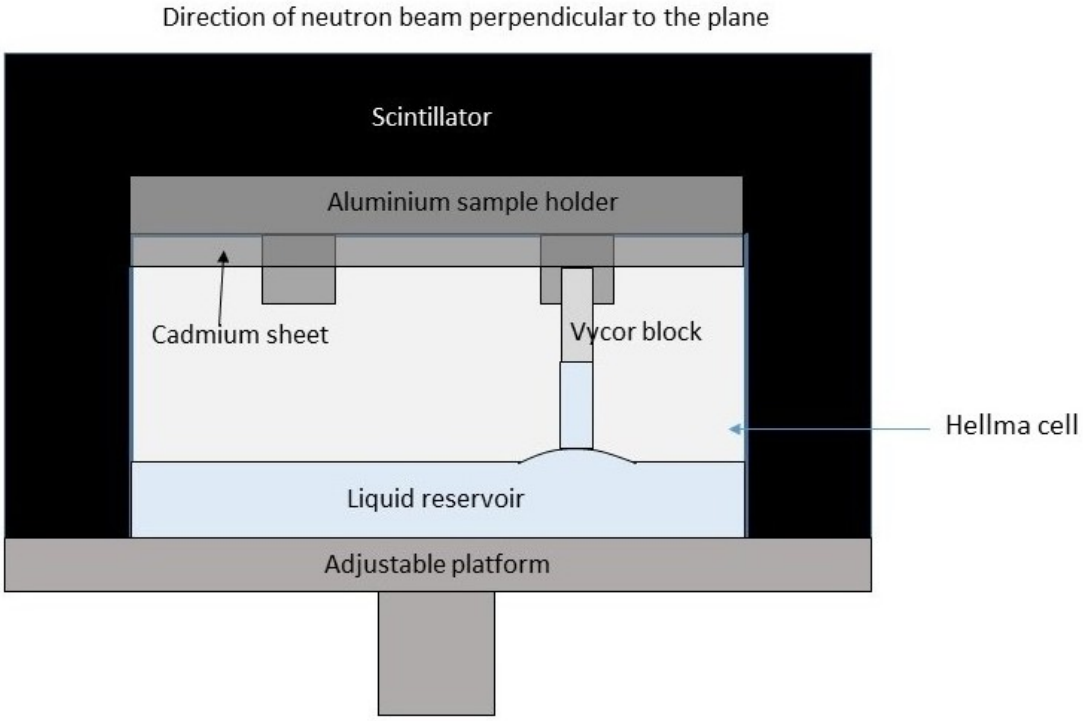

Figure 4.6: Setup of the imbibition experiment comprising of the quartz Hema cell filled with a TBA:TOL mixture. Vycor block is attached to a aluminium holder. A cadmium sheet to prevent radioactive activation of aluminium. Incoming neutron beam parallel to the plane of figure.

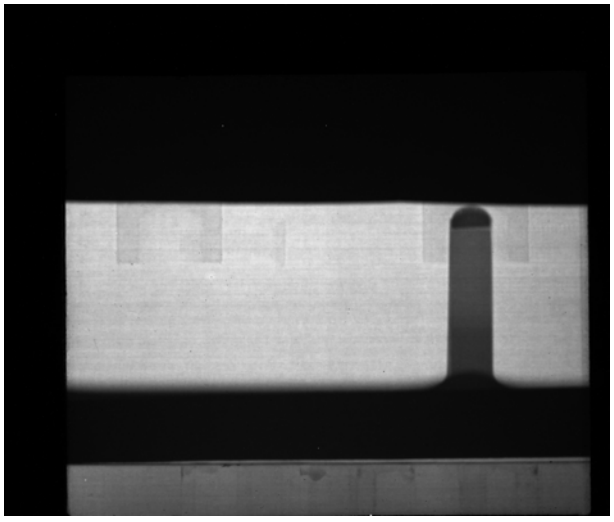

Figure 4.7: Image from a radiography experiment of imbibition in Vycor

empty Vycor and other the liquid mixture imbibing into it as

$$T_{imb}(t) = T_v \times T_{mix}(t)$$

We might as well take into account the contribution of Hellma cell in the above equation even though it is nearly completely transparent. We thus have

$$T_{imb}(t) = T_v \times T_{Hellma} \times T_{mix}(t)$$

Since the transmission at time $t = 0$ depends simply on the Vycor block and Hellma cell, we have

$$T_{imb}(t = 0) = T_v \times T_{Hellma}$$

Thus the transmission of the only dynamic part i.e. the rising liquid can be found by simply normalizing transmissions of all images by that of the first, consisting of empty Vycor and Hellma cell as given by.

$$\frac{T_{imb}(t)}{T_{imb}(t = 0)} = \frac{T_{imb}(t)}{T_v \times T_{Hellma}} = T_{mix}(t)$$

Plot profiles of transmission of the Vycor block were calculated using the ImageJ software for quantitative analysis. The details of which are discussed in the following section.

B.2 Results

Figure 4.8 shows a neutron radiography image of TOL imbibition into Vycor along with its plot profile after being normalized as described in the previous section. The block is presented here horizontally instead of vertically to make it easier to analyse its plot profile more conveniently as a function of time and distance. The distance here is represented in pixels which could be converted into SI units simply by multiplying a distance in pixels by the ratio of length of the Vycor block in metres (0.02 m) to the length in pixels such that 1 pixel$\approx$ 0.31 µm.

Figure 4.9 (a) shows the transmission plot profile of the entire experiment. We notice that the imbibition front is not moving parallel to the y-axis and has a broadened profile instead. In figure 4.9 (b) the corresponding derivative of transmission plot profile with respect to distance is shown. Calculating the derivative helps locating the position of front more precisely from the peak-position of curves, while the front broadening can be estimated from full width at half maxima (FWHM). The curves showing derivative of transmission plot profiles have been smoothed by a local smoothing technique using polynomial regression (degree 1) and weights computed from Gaussian density function.

We locate the position of each peak and its respective roughening (FWHM) and plot their variation with $\sqrt{t}$ as shown in figure 4.10.The very clear linear dependence of rise level of liquid front with $\sqrt{t}$ is completely in accordance to the Lucas-Washburn equation 4.2. The value of its slope thus gives the imbibition coefficient of TOL $C_H = 1 \times 10^{-4}\,\mathrm{m/s^{1/2}}$. We find the front roughening to be varying linearly with $\sqrt{t}$ as well for most of the process before reaching a plateau.

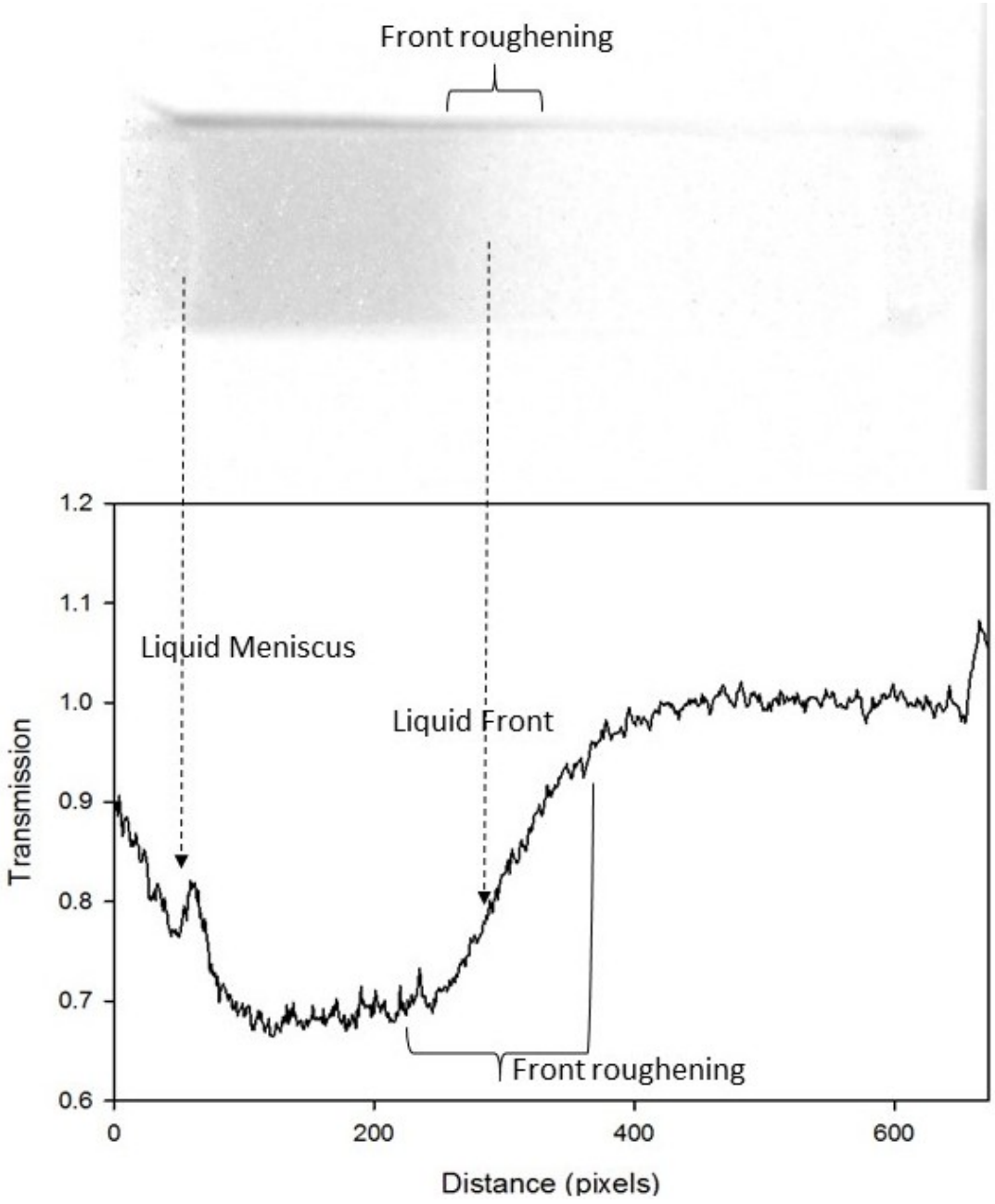

Figure 4.8: Image of TOL imbibition through Vycor, normalized by the first image along with the plot profile of its transmission

The front broadening has been reported in the past for imbibition of different liquids into Vycor block and has been explained to occur mainly because of the following reasons, the major one being the mechanism of pore-filling in such inter-connected porous network with pore-radius distribution. At the junction of two-interconnected capillaries of unequal radii, the one with smaller radius fills up faster than one with bigger radius due to greater Laplace pressure across it. However this movement of liquid in the smaller capillary is arrested momentarily when the pressure in both smaller and larger capillaries

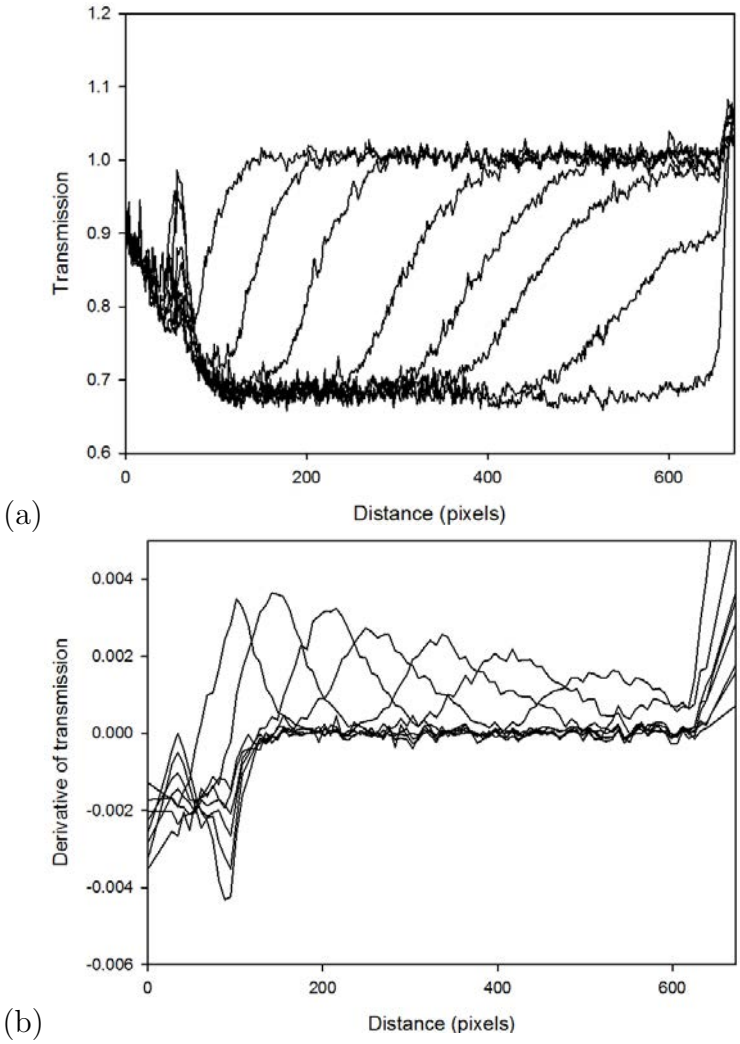

Figure 4.9: (a) Plot profiles of transmission of TOL for entire imbibition process versus distance travelled by the liquid front (pixels)
(b) Derivative of the plot profiles with respect to distance. The centre of peak shows position of the liquid front, while the FWHM of peaks give the roughening of front

are equal, with the larger one filled to lesser extent. Soon after the larger capillary starts filling and the imbibition process continues. This phenomenon of menisci arrest is very well described in the work of Simon Gruener et al[8] from a numerical simulation approach and was reported to follow a $\sqrt{t}$ itself, same as observed here for TOL imbibition. This broadening is reported in literature mostly as front-roughening.

Another important reason for such strong front-roughening is high volatility of TOL, such that the liquid front is preceded by its vapours, which eventually condense via capillary condensation to fill up the pores, which perhaps is the reason for plateauing of the front-roughening (figure 4.9(b)).

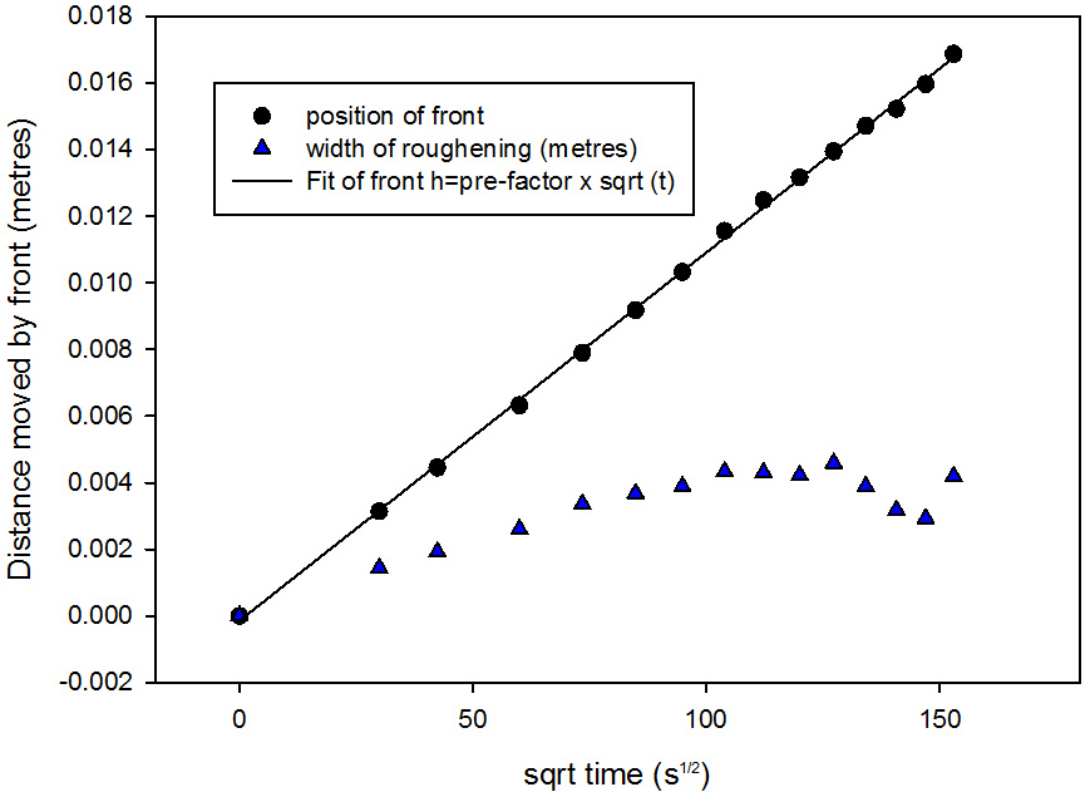

Figure 4.10: Position of the rising liquid front (in metres) (black points) and width of the roughening (metres) (blue triangles)as a function of $\sqrt{t}$. Fit of the experimental points by Lucas-Wasburn equation 4.2 $h(t) = C_H \times \sqrt{t}$.

Finally, the slower rate of image acquisition with respect to dynamics of imbibition causes the images to be slightly deformed in time, however this effect is technical in nature and minor compared to the previous two effects.

The exact same image processing steps were taken for TBA:TOL mixtures, 50:50 and 90:10, however unlike TOL, the images for imbibition of mixtures are not available until complete block filling. Figure 4.11 shows the imbibition process in few images for each sample.

Qualitatively it is possible to spot a few differences between individual experiments. We notice the rise level to be fastest in TOL, which gets slower with increasing concentration of TBA in the mixture. The difference in contrast between the 50:50 HH (TBA:TOL) and 50:50 HD mixture is clearly visible as well. For the 90:10 mixture (figure 4.11(d)) we notice the Vycor block filling up from the top which can be caused due to a loss in sealing causing TBA:TOL vapour mixture to fill up the Vycor block by capillary condensation. However its effect on the imbibition process in the time-scale of experiment could be ignored in a first approximation as long as no interaction between the two fronts is observed.

To quantitatively treat the images, similar data treatment was carried out as for pure

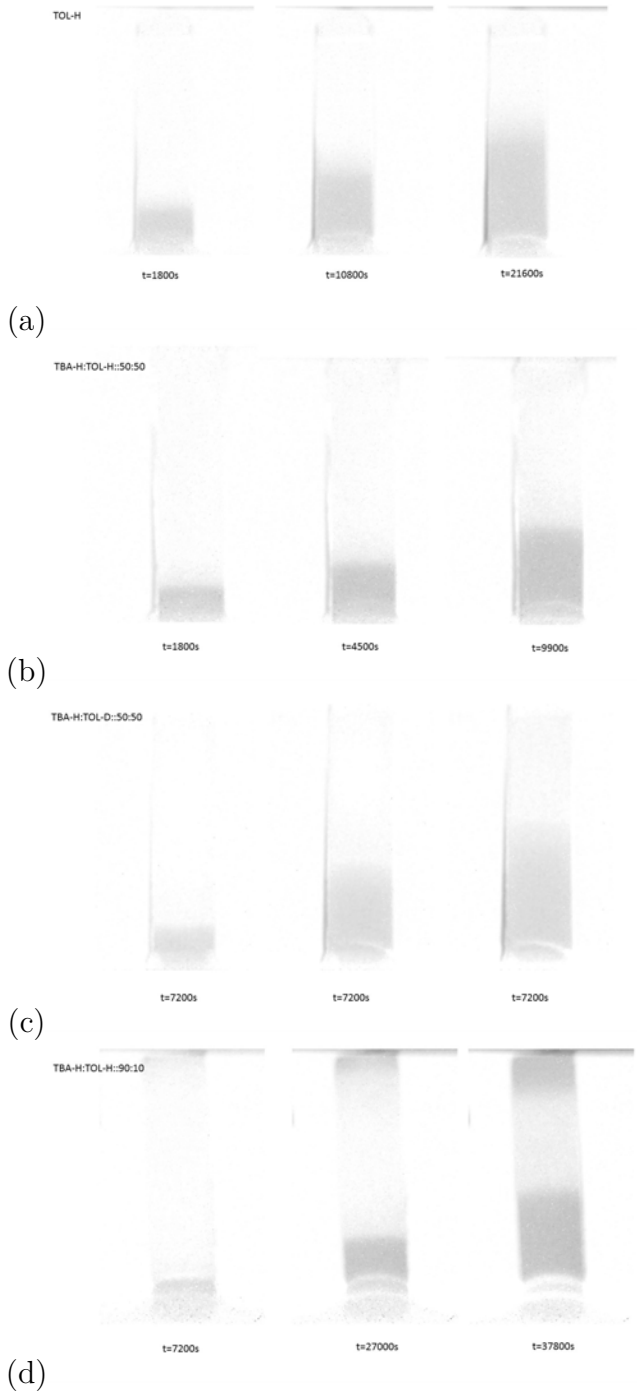

Figure 4.11: Imbibition images from neutron radiography for various expeirments(a) pure TOL (b) TBA-H:TOL-H 50:50 (c) TBA-H:TOL-D 50:50 (d) TBA-H:TOL-H 90:10

TOL in order to obtain the transmission profiles as shown in figure 4.12.

One can notice for the 50:50 mixture (TBA-H:TOL-H) shown in figure 4.12(a), that the imbibition front seen in the transmission profile is clearly different from that of pure

TOL (figure 4.9) because of the two visible slopes instead of one, indicating the presence of two different fronts and their respectively front-roughening. In the corresponding curves showing the derivative of transmission we observe a main peak of higher intensity and a shoulder peak of low intensity. These two peaks progressively shift forward and simultaneously broaden.

On the other hand such a two-front flow is not evidently observed for the 50:50 (TBA-H:TOL-D) mixture (figure 4.12(a)). It becomes clearer in the corresponding derivative of transmission, where the curves though not completely symmetric, do lack evidence of any second peak unlike 50:50 (TBA-H:TOL-H) mixture.

Finally for the case of 90:10 (TBA-H:TOL-H) mixture shown in figure 4.12(c), we notice the progression of two fronts, one due to imbibition from the bulk reservoir while the second possibly due to capillary condensation from the top. The derivative of transmission profiles reveal existence of a main peak and a shoulder peak for the imbibition front just like 50:50 (TBA-H:TOL-H) mixture.

The positions and FWHM of all peaks were extracted and have been plotted against the square root of time in figure 4.13. Positions of fronts for all mixtures as well as pure TOL are found to be varying linearly with $\sqrt{t}$ in accordance to the Lucas-Washburn equation. We notice in the case of 90:10 mixture a deviation from linear Lucas-Washburn dynamics in the initial part of the experiment. This is attributed to the position of rising front coinciding with the liquid meniscus of reservoir liquid for the first three hours of the imbibition due to its slow dynamics

On the other hand, widths of front-roughening were found to be very scattered but they do appear to be roughly increasing with time, although not strictly linear enough to be following Lucas-Washburn dynamics. Such a scattering can be expected from high vapour pressure liquids like TOL and TBA as the front-roughening is strongly influenced by the volatile nature of these liquids such that their vapours precede the liquid front.

Finding the slope of front position versus $\sqrt{t}$ for each experiment the imbibition coefficient C_H of the Lucas-Washburn equation for rise level dynamics (equation 4.2) and are listed in table below.

C_H	$\mathrm{m/s^{1/2}}$
TOL	1×10^{-4}
50:50 HH Main peak	7.4×10^{-5}
50:50 HH Shoulder peak	1×10^{-4}
50:50 HD	5.03×10^{-5}
90:10HH Main peak	4.02×10^{-5}
90:10HH Shoulder peak	5.31×10^{-5}

We now proceed to calculate the imbibition strength I of the Vycor block using the surface tension, density and viscosity values of bulk TOL from the following equation:

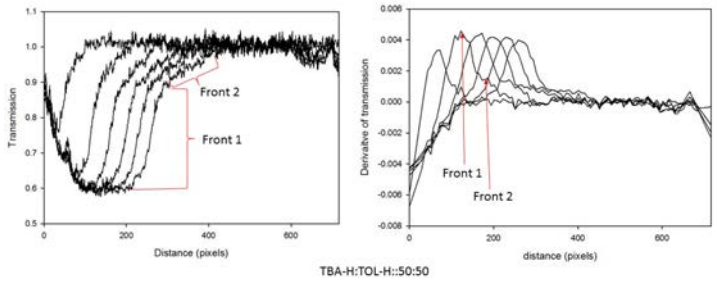

(a)

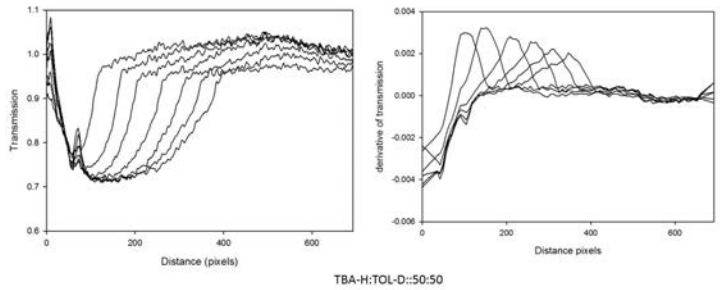

(b)

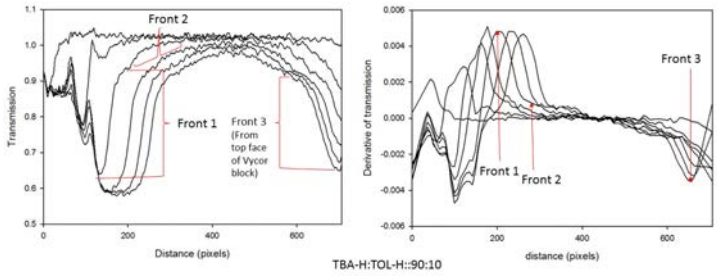

(c)

Figure 4.12: Transmission plot profiles of mixtures along with their respective derivatives with respect to distance (a) TBA-H:TOL-H 50:50 (b) TBA-H:TOL-D 50:50 (c) TBA-H:TOL-H 90:10

$$C_H = \sqrt{\frac{\sigma \cos\theta}{2\phi_a \eta}} I$$

Although we did not have any means to measure the weight of block right after its extraction from the liquid reservoir in order to determine the reduced porosity due to possible formation of pre-adsored water layers, we assign $\phi_a = 0.2746$, the same value as in the section of gravimetric study of imbibition, since it corresponds to one monolayer of

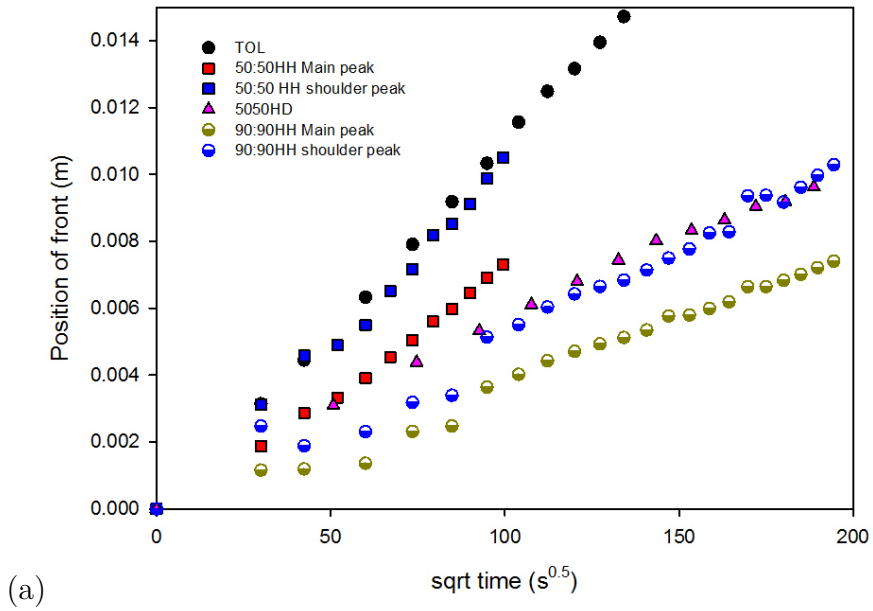

(a)

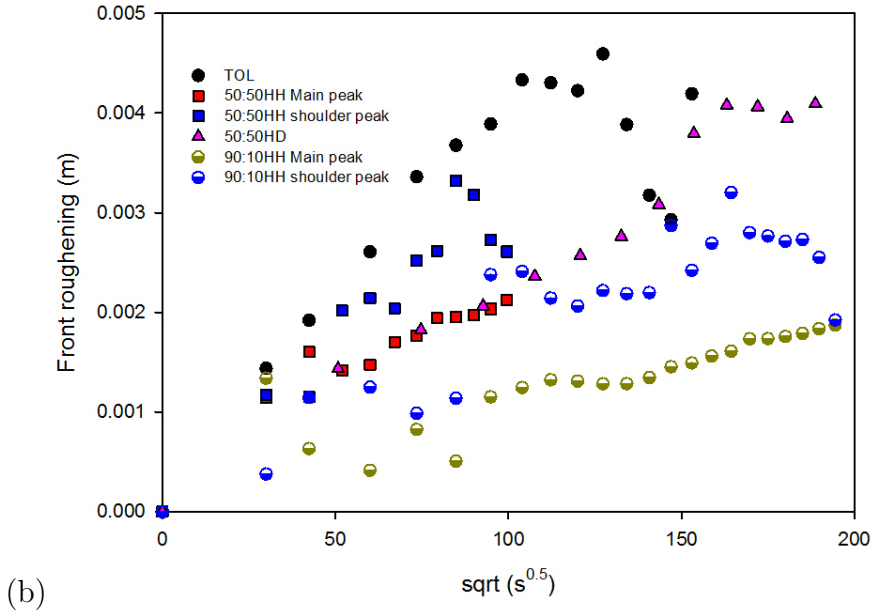

(b)

Figure 4.13: Transmission plot profiles of mixtures along with their respective derivatives with respect to distance (a) TBA-H:TOL-H 50:50 (b) TBA-H:TOL-D 50:50 (c) TBA-H:TOL-H 90:10

water adsorbed on the pore surface. We thus obtain

$$I = 1.073\,54 \times 10^{-5}\,\mathrm{m}^{1/2}$$

In a method similar to one followed in the gravimetric study, we calculate the C_H values for mixtures using their known bulk properties and the value of I obtained above and plot against them the values of C_H obtained from the slope of position of front versus

$\sqrt{t}$ from experiment (4.13(a)). This is represented in figure 4.14.

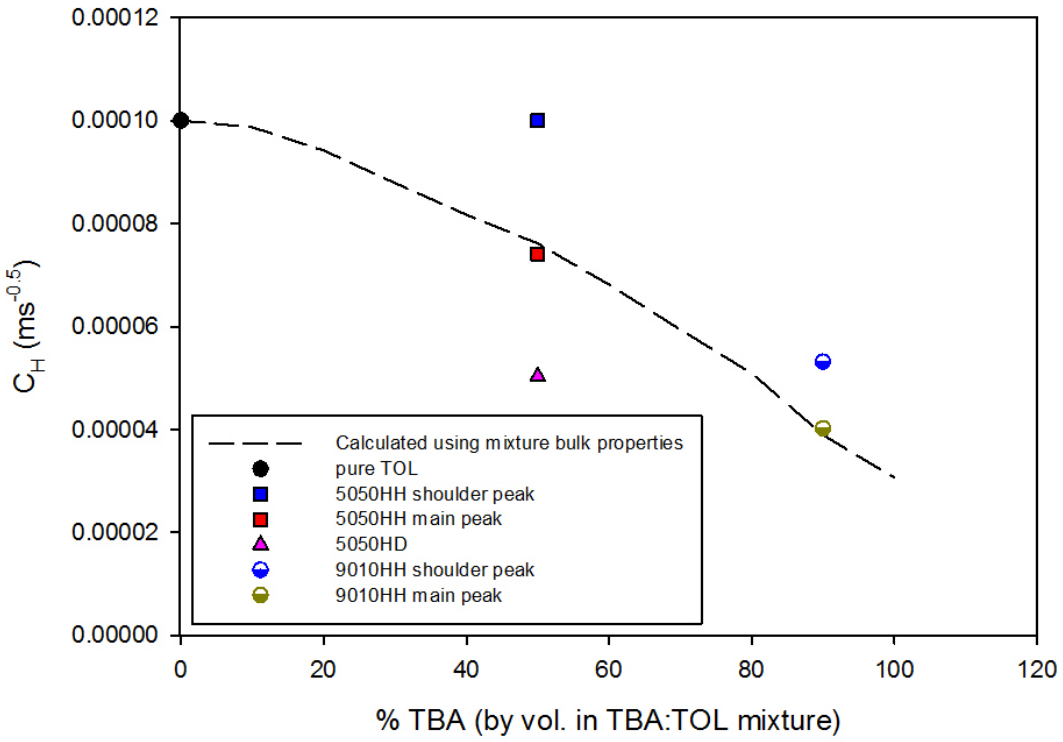

Figure 4.14: Comparison of the imbibition coefficient C_H^{calc} (dashed line), calculated from surface tension and viscosity of bulk mixtures with C_H^{exp} (different coloured points), obtained from slope of experimental curves in figure 4.13(a).

A clear observation here is that the main peak of both 50:50 (TBA-H:TOL-H) and the 90:10 (TBA-H:TOL-H) mixtures fall on the curve predicted by the Lucas-Washburn equation (eqn 4.2). However, their respective shoulder peaks appear to be travelling faster as we find $C_H^{shoulder}$ value equalling to $C_H^{mainpeak}$ of pure TOL and mixture composition $\%TBA = 77\%$ for the 50:50 and 90:10 (TBA-H:TOL-H) mixtures respectively.

We attempt to explain it by the phenomenon of menisci arrest[8] discussed earlier in this section. The occurrence of two fronts, the leading one being much smaller, indicates a certain level of phase-separation. If this true then at the junction of two capillaries of unequal radii, the component with greater surface tension (respectively richer in TOL) will have a greater capillary pressure according to Young-Laplace equation (equation (1.1)) which might enable it to rise ahead and occupy a given capillary, until its rise is arrested and eventually the capillaries start filling up with the TBA:TOL mixture making up the major imbibition front. Thus the component richer in TOL continues to separate out momentarily and fill up the porous network first, forming the leading imbibition front. However the average dynamics of imbibition are still governed by the rise of the main front following its reservoir mixture composition analogous to the findings by the gravimetric

technique.

We come finally to the 50:50 (TBA-H:TOL-D) mixture. The high transmittance of TOL-D and its effect on the final contrast compared to 50:50 (TBA-H:TOL-H) is observed qualitatively in figure 4.11 (b) and (c) with the transmission being higher for the latter one naturally. Upon comparing the transmission plot profiles and their derivatives of 50:50 HH and HD mixtures from figures 4.12(a) and (b), we observe that the second imbibition front characterised by a shoulder peak has disappeared completely for the 50:50 HD mixture. Since the objective of using TOL-D was to mask its contribution to the rising front in case of a phase separation, its disappearance in the 50:50 HD mixture further confirms the interpretation of a phase separation into two imbibition fronts, one of them being pure TOL.

The derivative of transmission of the 50:50 HH and 50:50 HD mixture are plotted together for comparison in figure 4.15. We find the main liquid front of the 50:50 HD to be rising quite slowly, having a value of $C_H = 5.03 \times 10^{-5}\,\mathrm{m/s^{1/2}}$ which is equivalent to dynamics of an 80% TBA mixture. Considering that the surface tension and viscosity of TOL-D and TOL-H are approximately the same, one would expect the 50:50 HD mixture to follow the same dynamics as HH mixture. One possible explanation of this apparent slowed down dynamics could be attributed to the high transmittance of TOL-D, as a result of which the rising front observed is mostly contributed by TBA-H and thus imbibition dynamics of the liquid appears closer to pure TBA.

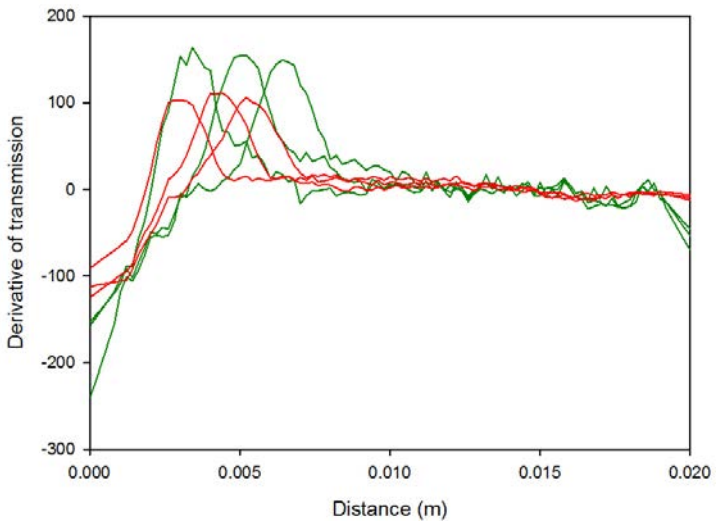

Figure 4.15: Comparison of the derivative of transmission plot profile for the 50:50 (TBA-H:TOL-H) (green) and 50:50 (TBA-H:TOL-D) (red) from images corresponding to same duration of the imbibition process.

IV Conclusion

The role of specific hydrogen-bonding interactions between hydroxyl group of TBA and silica surface on the dynamics of TBA:TOL imbibition into Vycor, a monolithic nanoporous silica was investigated. We observe that the rate of imbibition, better known as its imbibition coefficient $C_M(\mathrm{kg}/\sqrt{\mathrm{m}})$ found experimentally for TBA:TOL mixtures from their mass uptake versus $\sqrt{t}$ plots could be predicted theoretically by the well-known Lucas-Washburn law for simple liquids by assuming the liquid mixtures to behave like homogeneous simple liquids with mass density, surface tension and viscosity values equal to that of the mixtures at different compositions. This good agreement with the Lucas-Washburn law suggested that the specific hydrogen-bonding interactions between TBA and silica surface known to exist under equilibrium conditions are not exhibited in out-of-equilibrium condition and thus do not play any role in governing capillary rise dynamics of TBA:TOL mixtures.

Quantitative analysis of the rise level by neutron radiography revealed separation of the imbibition front into two phases. The value of imbibition coefficients revealed that the leading front showed dynamics characteristic of a mixture with higher TOL composition than in the bulk reservoir, while the trailing front had dynamics corresponding to a mixture composition same as that of bulk reservoir. Especially in the case of 50:50 (TBA-H:TOL-H) mixture, the leading front appeared to have dynamics equal to pure TOL. We attribute the occurrence of this phase separation to TOL's higher surface tension which at a capillary junction of unequal radii might cause a phase separation into one with higher surface tension (respectively more TOL) to momentarily rise ahead due to a greater Laplace pressure. However we find the contribution of this second leading front to be minor and it is in fact the slower front following bulk reservoir composition which drives overall imbibition dynamics analogous to the results of gravimetric study.

Bibliography

[1] Bell, J. M., and Cameron, F. The flow of liquids through capillary spaces. *The Journal of Physical Chemistry 10*, 8 (1906), 658–674.

[2] Darcy, H. *Les fontaines publiques de la ville de Dijon: exposition et application...* Victor Dalmont, 1856.

[3] Debye, P., and Daen, J. Stability considerations on nonviscous jets exhibiting surface or body tension. *Physics of Fluids (1958-1988) 2*, 4 (1959), 416–421.

[4] Dimitrov, D., Milchev, A., and Binder, K. Capillary rise in nanopores: molecular dynamics evidence for the lucas-washburn equation. *Physical review letters 99*, 5 (2007), 054501.

[5] Dumitrescu, V., and Pântea, O. Viscosities of binary mixtures of toluene with butan-1-ol and 2-methylpropan-2-ol. *Journal of the Serbian Chemical Society 70*, 11 (2005), 1313–1323.

[6] Gruener, S., and Huber, P. Spontaneous Imbibition Dynamics of an n -Alkane in Nanopores: Evidence of Meniscus Freezing and Monolayer Sticking. *Physical Review Letters 103*, 17 (oct 2009), 174501.

[7] Gruener, S., and Huber, P. Imbibition in mesoporous silica: rheological concepts and experiments on water and a liquid crystal. *Journal of physics. Condensed matter : an Institute of Physics journal 23*, 18 (may 2011), 184109.

[8] Gruener, S., Sadjadi, Z., Hermes, H. E., Kityk, A. V., Knorr, K., Egelhaaf, S. U., Rieger, H., and Huber, P. Anomalous front broadening during spontaneous imbibition in a matrix with elongated pores. *Proceedings of the National Academy of Sciences of the United States of America 109*, 26 (jun 2012), 10245–50.

[9] Grüner, S. A. Rheology and Dynamics of Simple and Complex Liquids in Mesoporous Matrices.

[10] Huber, P., Grüner, S., Schäfer, C., Knorr, K., and Kityk, a. V. Rheology of liquids in nanopores: A study on the capillary rise of water, n-Hexadecane and n-Tetracosane in mesoporous silica. *The European Physical Journal Special Topics 141*, 1 (feb 2007), 101–105.

[11] Kiepsch, S., and Pelster, R. Interplay of vapor adsorption and liquid imbibition in nanoporous vycor glass. *Physical Review E 93*, 4 (2016), 043128.

[12] Liu, H., and Cao, G. Effectiveness of the young-laplace equation at nanoscale. *Scientific reports 6* (2016).

[13] Lucas, R. Ueber das zeitgesetz des kapillaren aufstiegs von flüssigkeiten. *Colloid & Polymer Science 23*, 1 (1918), 15–22.

[14] Nikam, P. S., Jagdale, B. S., Sawant, A. B., Hasan, M., Chemistry, P., College, M. S. G., and Camp, M. Densities and Viscosities of Binary Mixtures of Toluene with Methanol , Ethanol , Propan-1-ol , Butan-1-ol , Pentan-1-ol , and. 559–563.

[15] Sears, V. F. Neutron scattering lengths and cross sections. *Neutron news 3*, 3 (1992), 26–37.

[16] Speight, J. G., et al. *Lange's handbook of chemistry*, vol. 1. McGraw-Hill New York, 2005.

[17] Washburn, E. W. The dynamics of capillary flow. *Physical review 17*, 3 (1921), 273.

[18] Xue, Y., Markmann, J., Duan, H., Weissmüller, J., and Huber, P. Switchable imbibition in nanoporous gold. *Nature communications 5*, May (jan 2014), 4237.

5

General Conclusion and future perspectives

The study of structural and dynamic phenomena in a model binary liquid system under nano-confinement was approached in a unique way by using a combination of thermdynamic equilibrium and out-of-equilibrium conditions. The use of TBA and TOL, two molecules with distinct ways of molecular interaction, i.e. H-bonding versus Van der Waals, provided a system which appears to be ideal from a macroscopic scale, but shows non-ideal behaviour at the nanoscale, owing to the ability of TBA to form H-bonded networks. This non-ideal nature existent in bulk state itself proved to be very useful for understanding the effect of nanometric spatial confinement and tunable surface chemistry on the molecular organization of the confined binary liquids and the driving forces behind it.

Chemical shift study from ^{1}H MAS NMR experiments unveiled the existence of H-bonding networks in mixtures under confinement in MCM-41 pores at such low concentrations of TBA, where in the bulk liquid mixtures TBA molecules completely lose their H-bonded network and are present as free monomers. The persistence of H-bonded networks at high TBA dilution in confinement thus raised the possibility of a new type of H-bonding interaction not seen in bulk, i.e. between hydroxyl group of TBA and free surface silanol groups on MCM-41 pore wall. If this is true then at higher TBA concentrations, more number of TBA molecules must be interacting with the pore-surface leading to a nano-segregation. This finding justifies the previously reported core-shell model of phase separation of TBA:TOL mixtures confined in MCM-41 and SBA-15 nanopores (Chapter 1, section E) where TBA separates out to form a monolayer-thick shell attached to silica pore wall while TOL forms the core.

The small diameter of MCM-41 pore (3.4 nm), only a few molecular layers wide could accommodate only one monolayer of TBA shell and a core which is 2-3 molecular layers thick. In bigger pores like those of SBA-15 (8 nm) there might be possibility of a concentration gradient from pore wall to centre of pore or presence of interfaces of TBA:TOL mixtures instead of a sharp core-shell boundary. Thus a chemical shift study on TBA:TOL mixtures confined in SBA-15 might prove useful to investigate the nature of H-bonding interactions as a consequence of these interfaces. The influence of changing the chemical nature of pore walls from hydrophilic to hydrophobic by changing the host matrix to CMK-3 which has small pore diameter (4 nm) similar to MCM-41 has the potential to change the nature of H-bonded network, as TBA could no longer make H-bonding interactions with the pore wall. This makes it interesting to investigate whether the -OH chemical shift will exhibit a behaviour reminiscent of bulk TBA:TOL mixtures or unveil some characteristics unique to confinement in CMK-3.

An attempt to characterize the self-diffusion dynamics of TBA:TOL mixtures in confinement using PFG NMR method was met with certain challenges. The mean square displacement of TOL molecules confined in MCM-41 greatly exceeded the pore length itself. The molecular motions as a result were fast enough even for the minimum possible value of time-resolution Δ, such that the molecules could travel several times along the pore-length and make the self-diffusion dynamics appear Δ-independent. However a precise measurement of MCM-41 pore length was achieved (0.65 µm) which was not possible to obtain via electron microscopy.

The diffusion of TOL in TBA:TOL mixtures confined in SBA-15 revealed the existence of two populations of different dynamics, one which was two orders of magnitude faster

than diffusion of TOL in bulk mixture of same composition and a second population with slower dynamics comparable to that of bulk which was found to be Δ-dependent. Interestingly, the magnetization attenuation was found to be Δ-dependent, an observation characteristic of isotropic bulk-like diffusion, but at the same time no strict mixture composition dependence was seen, unlike TBA:TOL bulk mixtures which show strong concentration dependence in the diffusion dynamics of TBA and TOL. However, the strong decay of magnetization in the case of SBA-15 at much lower q values, perhaps owing to the very short transverse relaxation time ($T_2 \approx 2\,\mathrm{ms}$) of the confined species causes a fast loss of correlation between nuclear spins even for the smallest possible Δ values, which makes it difficult to confirm whether the observed magnetization decay curves represent the whole information on the self-diffusion dynamics.

Gravimetric vapour sorption experiments of TBA and TOL binary gas mixture in MCM-41 pores showed that the influence of H-bonding interactions between TBA and silica surface extends even to gas-solid interface, leading to preferential adsorption of TBA. With the help of a multi-component BET model, we expressed semi-quantitatively the sheer difference of interaction of the two molecules with the silica surface in terms of a thermodynamic parameter giving the energetic affinity of each molecule for the silica surface. We find the energy of interaction of TBA with the silica surface to be two orders of magnitude greater than TOL which leads to a 100% TBA monolayer coverage of the pore surface with as little as 10% TBA in the binary gas. Thus MCM-41 acts as a surface selective material for TBA. Very interestingly, after coverage of pore-surface by first monolayer of TBA, the surface loses its selectivity completely and the subsequent layer follows the binary gas composition. The difference in nature of interactions between the first and second adsorbed layers, i.e. H-bonding interactions between TBA and silica surface and Van der Waals interaction in the second layer, is strong enough to cause the two layers to lose correlation between each other. At complete pore-filling post capillary condensation, we find that the concentration of TBA inside pore increases rapidly compared to its binary gas concentration until $x_{TBA}^{pore} \approx 44\%$, beyond which the rise in TBA concentration is much more gentle. Considering that the volume fraction of pore occupied by a monolayer of TBA is approximately 44%, the situation could be rationalized very well once again by the core-shell model such that, as long as there is sufficient amount of TBA to have complete monolayer coverage of the pore surface, a phase separation would take place giving rise to a shell of TBA and a TOL-rich core whose concentration could be determined. The application of this multi-component BET to adsorption in CMK-3, which is hydrophobic in nature, revealed reversal in the nature of molecular interactions such that the monolayer had higher concentration of TOL than its corresponding concentration in the binary gas, even though the effect was not as strong as seen for TBA/silica-surface affinity. This was reflected in the lesser difference between the thermodynamic parameters TBA and TOL respectively with the carbon surface when compared to silica surface. Most importantly we were able to demonstrate here that by tuning the chemical nature of pore surface we are able to switch the molecular level organization at the nanoscale by simply playing with the specific interactions that confined liquids make with the pore-walls and amongst themselves.

The model of core-shell under equilibrium conditions justified by a structural and thermodynamic point of view raised interest in investigating whether these surface-specific

effects are also exhibited in out-of-equilibrium conditions, which may lead to a deviation in spontaneous imbibition dynamics of these binary liquids from the Lucas-Washburn dynamics, which has in the past, successfully described flow of simple liquids even in nanopores.

Gravimetric study of spontaneous imbibition of TBA:TOL mixtures in Vycor, made up of interconnected networks of nanoporous silica revealed that the dynamics of our binary liquids could be predicted well by Lucas-Washburn equation, assuming the binary liquids to be homogeneous in nature having density, surface tension and viscosity equal to the corresponding bulk-state mixtures. This makes us conclude that under flow, the phase separation effects are not exhibited.

However, neutron radiography study of the same process showed TBA:TOL mixtures to rise with two fronts, indicating a phase separation. The front rising above, showed dynamics characteristic of higher amount of TOL than in the original mixture composition, while the trailing front was found to have dynamics as predicted from Lucas-Washburn law for the given mixture composition. Replacing TOL by its deuterated version TOL-d caused disappearance of the TOL-rich front for the 50% TBA by vol. mixture. As TOL-d is a strong scatterer, disappearance of the TOL-rich front strengthens the interpretation of phase separation. However the TOL-rich phase is found to be much smaller in width than the one obeying reservoir mixture composition. Very interestingly though, we find the leading front for 50% TBA mixture to show dynamics similar to that of pure TOL, while the leading front for 90% TBA mixture showed dynamics similar to a mixture which has higher TOL concentration than in bulk reservoir ($\approx 77\%$). Such concentration dependence that starts from pure TOL and goes to high TBA concentration raises an important question, does the phase separation starts occurring only after a certain minimum threshold concentration of TBA is crossed, which could then be directly associated with specific interactions of TBA with the silica surface. To answer this, a systematic study over a wide concentration range is required in order to analyze dynamics of the phase-separated front and also to use different isotopic combinations to play with the contrast of the rising liquid, which could make a beneficial undertaking for the future.

At present the phase separation phenomenon has been interpreted as an interplay between the different surface tensions of TBA and TOL, such that at capillary junctions, a TOL-rich phase due to its greater surface tension momentarily separates out and occupies a capillary ahead of the main mixture because of its greater Young-Laplace pressure. Since this front rises as a square root of time as well, we might conclude that this effect is continuous throughout the imbibition process but still small as the dynamics of imbibition is still governed by the slower front which overwhelmingly constitutes the rising liquid front.

Neutron radiography technique was utilised to investigate if the H-bonding interactions between TBA and silica surface was dominant enough to replace TOL from a Vycor sample completely filled with TOL. A block of Vycor was filled completely by TOL-D via imbibition process. After complete filling, the liquid reservoir was replaced by a 90:10 TBA-H:TOL-H mixture such that only the bottom of block was in contact with the liquid surface. In a course of about 21 hours, we notice the gradual decrease of transmission of the sample up to a certain extent, beyond which the final contrast stayed stable. The image of Vycor block completely filled with TOL-D as well as the successive images of

the block in contact with the 90:10 HH (TBA-H:TOL-H) mixture were normalized by the image of empty Vycor block. The transmission profile of the experiment is shown in figure 5.1(a), while in figure 5.1 (b), neutron radiography images of the changes occurring in the contrast of liquid filled inside the Vycor block, TOL-D at $t = 0$ (extreme left) after ≈ 21 hours (1230 minutes)(extreme right) are shown along with intervening steps.

We find a decrease in transmission of the block at the end of experiment. This indicates that TOL-D has been replaced inside the block by TBA-H since it has a lower transmittance. For a diffusive motion of TBA one would expect a front of lower transmittance moving ahead with time. However what we do observe is a homogeneous decrease in transmission of the entire block with time even though the rate of decrease in transmission is faster closer to the bottom of block or in other words beginning of the transmission profile. One possible explanation could be leakage in the sealant material covering sides of the Vycor block leading to diffusion of TBA from all sides. However if that were to be true, the dynamics of this process should have been much faster which is obviously not the case. The replacement of TOL-D by TBA-H is a complex situation involving simultaneous entry of TBA molecules while exit of TOL and the entire process driven by stronger affinity between silica surface and TBA molecules compared to TOL. An appropriate model which could explain such diffusion phenomenon driven by competition between liquid-liquid and liquid-wall interactions could be yet another interesting undertaking for future.

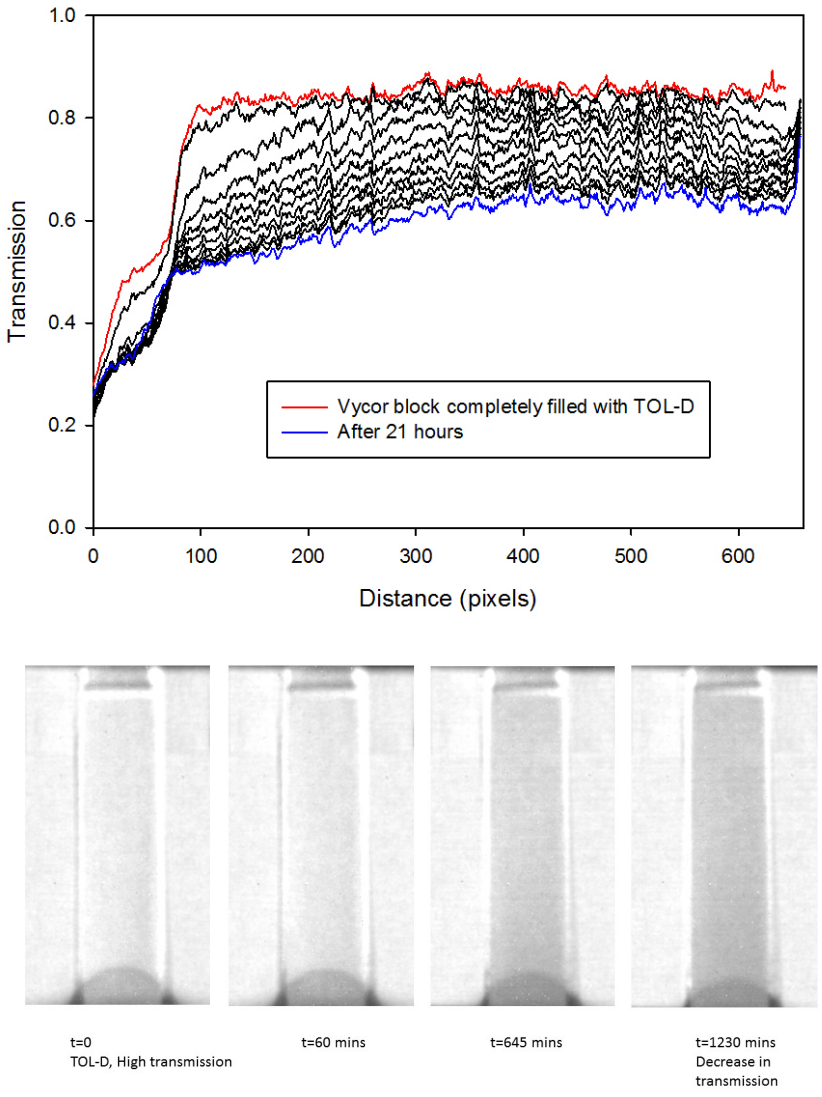

Figure 5.1: (a) Transmission profile of the Vycor block normalized by its empty state. Red curve is for block filled with TOL-D, while the blue curve is obtained after 21 hours of contact with TBA-H:TOL-H 90:10 mixture. The black curves display the gradual decrease in transmission over time. (b) Neutron radiography images of the changes occurring in the contrast of liquid filled inside the Vycor block, TOL-D at $t = 0$ (extreme left) and possible inclusion of TBA-H after $\approx$ 21 hours (1230 minutes)(extreme right), along with intervening steps.

Résumé

Les mélanges de toluène et de *tert*-butanol sont complètement miscibles dans toutes les compositions à l'échelle macroscopique. Toutefois *tert*-butanol forme un réseau de liaisons hydrogène à l'échelle nanométrique qui persistent même dans les mélanges liquides binaires *tert*-butanol/toluène. Des expériences de diffusion de neutrons ont révélé la séparation des phases du mélange dans une structure coeur-gaine sous confinement dans des solides nanoporeux hydrophiles. Le travail effectué dans cette thèse vise à comprendre le rôle joué par la concurrence des interactions intermoléculaires (liaisons hydrogène, Van der Waals) lors de la séparation de phase sous nanoconfinement. Des expériences de RMN révèlent la persistance d'un réseau de liaisons hydrogène dans ces liquides binaires confinés dans des nanopores de silice à des concentrations faibles de *tert* -butanol, fournissant la preuves d'un autre type de réseau de liaisons hydrogène sous confinement. Des expériences d'adsorption du mélange gazeux dans des nanopores de silice ont aidé à expliquer l'affinité plus élevée des parois de silice polaires pour *tert*-butanol par une modèle thermodynamique. Le remplacement de la matrice hôte par un analogue hydrophobe est associé à une inversion de la sélectivité, montrant cette fois une plus grande affinité du toluène pour la surface des pores. L'effet des interactions spécifiques avec la surface sur la dynamique d'imbibition spontanée de ces liquides binaires à travers le réseau de silice nanoporeux a également été étudié. Des expériences de radiographie de neutrons ont révélé la séparation des flux à deux composants, au sein d'une dynamique toujours gouvernée par une loi de Lucas-Washburn.

.

Abstract

Toluene and *tert*-butanol mixtures are completely miscible for all compositions at the macroscopic scale. However *tert*-butanol forms a network of hydrogen-bonded clusters at the nanoscale which persist even in the *tert*-butanol-toluene binary liquid mixtures. Interpretation of neutron scattering experiments revealed phase separation of the mixture into a core-shell structure inside hydrophilic nanoporous solids, with a *tert*-butanol shell and a toluene core. The work carried out in this thesis is aimed at understanding the role played by competing intermolecular interactions (hydrogen-bonding, van der Waals) in driving phase separation in confinement. NMR experiments reveal the persistence of a hydrogen-bonding network in these binary liquids confined in silica nanopores even at very low concentrations of *tert*-butanol, providing evidence of a new kind of hydrogen bonded network under confinement. Vapour sorption isotherms of *tert*-butanol-toluene binary gas mixtures in silica nanopores helped explain higher affinity of polar silica walls for *tert*-butanol by a thermodynamic model. Replacing the host matrix by a hydrophobic analogue was found to reverse the selectivity, with toluene showing greater affinity for the pore surface. Effect of surface specific interactions was studied on spontaneous imbibition dynamics of these binary liquids through nanoporous silica network. Neutron radiography experiments revealed the separation of fluxes into a two-component flow, generally obeying the Lucas-Washburn law.

Synthèse de thèse: Adsorption and imbibition of binary liquids in nanoporous solids

Auteur: Sujeet Dutta

Institut de Physique de Rennes

Date de soutenance: 2/12/2016

Mention: Physique

Les systèmes hétérogènes composés d'interfaces liquide-gaz, solide-gaz, solide-liquide été longtemps étudié et appliqué à une vaste gamme d'utilisations technologiques dans des domaines tels que le pétrole le raffinage, la catalyse, le dessalement de l'eau, les produits pharmaceutiques et ainsi de suite. Peu à peu, la complexité de ces systèmes a continué de croître avec l'avènement de matériaux conçus pour une plus grande surface d'activité et de fonctionnalité. Dans la classe des systèmes hétérogènes les matériaux poreux sont les plus connus. Zéolites et des MOFs (Metal-Organic Frameworks), qui sont souvent fonctionnalisés pour atteindre des objectifs spécifiques sont largement utilisés dans les produits chimiques l'industrie, et de nos jours avec un croissant d'importance sur les questions environnementales trouvant application dans le stockage et la filtration de les composé organiques volatils qui sont exemples de croissance dans la portée des matériaux poreux avec ultra-haute surface spécifique.

Matériaux nanoporeux avec des diamètres de pores allant de 2 - 50nm, comparable à un peu de couches moléculaires sont bien connus et largement étudiées. Il a été démontré précédemment que les molécules de liquide ou de gaz de confinement dans de tels nanopores avec des géométries spécifiques à l'échelle nanométrique pourrait conduire à une grande modification des propriétés physiques des molécules par rapport à leur état de volume libre. L'architecture poreuse et la concurrence entre les interactions moléculaires liquide-mur et liquide-liquide (Van der Waals, hydrogénation,π-π empilage, etc.) pourrait induire la séparation de phases et la séparation des phases désordre. Il a été démontré que la structuration induite par confinement se modifier la cristallisation et les températures de transition vitreuse des espèces confinées. Ainsi, la notion des propriétés physiques moyennes telles que la densité, la viscosité ou la tension superficielle des liquides en volume doit être appliquée avec caution tout en traitant des systèmes nanoconfinés.

Il a été démontré que la structuration induite par le confinement entraîne une modification de la dynamique propriétés de l'échelle de longueur sous-nanométrique (changements conformationnels groupes) à l'échelle micrométrique (auto-diffusion de translation). Avec la disponibilité de méthodes avancées de caractérisation de la matière molle, phénomènes induits par le confinement ont fait l'objet d'une étude approfondie pour les systèmes mono-composants. L'actualité scientifique l'intérêt porté à l'étude des systèmes à composantes multiples avec plus en plus complexité. Bien que beaucoup de questions aient été bien traitées pour les systèmes montrant une miscibilité beaucoup reste à désirer pour comprendre le rôle joué par la concurrence liquide-liquide et les interactions liquide-paroi dans la structure et la dynamique des systèmes multi-composants montrant un écart de miscibilité négligeable.

Ces questions s'étendent à deux types de systèmes, l'un à l'équilibre thermodynamique, dynamiques caractérisées par des vibrations moléculaires, des rotations et des autodiffusion et autres qui sont hors d'équilibre caractérisés par des propriétés d'écoulement des matériaux confinés à travers les nano-capillaires, où l'architecture des pores et l'environnement chimique pourraient jouer un rôle dans la modification des caractéristiques d'écoulement en à l'état contre en volume. Dans le présent chapitre, nous discutons des divers phénomènes induits par le confinement découverte jusqu'à présent et le cas scientifique de cette thèse qui tente de répondre à certaines des questions non résolues dans ce domaine.

L'étude des phénomènes structuraux et dynamiques dans un système liquide binaire modèle sous nano-confinement a été approché d'une manière unique en utilisant une combinaison de thermodynamique l'équilibre et les conditions hors d'équilibre. L'utilisation de TBA (*tert*-butanol) et TOL (toluène), deux molécules avec des modes distincts d'interaction moléculaire, c'est-à-dire la liaison hydrogène par rapport à Van der Waals, a fourni un système qui semble être idéal à partir d'une échelle macroscopique, mais montre comportement non idéal à l'échelle nanométrique, en raison de la capacité de TBA à former des réseaux. Cette nature non idéale existant en volume lui-même s'est révélée très utile pour comprendre l'effet du confinement spatial nanométrique et de la chimie superficielle réglable sur l'organisation moléculaire des liquides binaires confinés et les forces motrices derrière-il.

L'étude du déplacement chimique à partir des expériences ^{1}H MAS NMR a dévoilé l'existence réseaux dans des mélanges en confinement dans des pores MCM-41 à des concentrations aussi faibles de TBA, où dans les mélanges liquides en volume les molécules TBA perdent complètement leur réseaux à liaison hydrogène et sont présents sous forme de monomères libres. La persistance des réseaux à liaison H à une dilution TBA élevée en confinement a donc soulevé la possibilité d'un nouveau type de liaison hydrogène interaction non observée en volume, c'est-à-dire entre le groupe hydroxyle de TBA et la surface libre silanol sur la paroi de pores MCM-41. Si cela est vrai alors à des concentrations plus élevées de TBA, plus de molécules de TBA doivent interagir avec la surface des pores conduisant à un nano-ségrégation. Cette constatation justifie le modèle cœur-gaine précédemment rapporté de phase séparation des mélanges TBA: TOL confinés dans des nanopores de MCM-41 et SBA-15 (Chapitre 1, section E) où TBA se sépare pour former une gaine épaisse monocouche attachée à la silice tandis que TOL forme le cœur.

Le petit diamètre du pore MCM-41 (3,4 nm), seulement quelques couches moléculaires de large pourrait n'accueillent qu'une seule monocouche de gaine TBA et un cœur qui est de 2 à 3 couches moléculaires épais. Dans les pores plus grands comme ceux de SBA-15 (8 nm) il pourrait y avoir possibilité d'une gradient de concentration de la paroi de pore au centre du pore ou présence d'interfaces de TBA: TOL mélanges au lieu d'une limite cœur-gaine tranchante. L'influence du changement de nature chimique des parois des pores, de hydrophile à hydrophobe en changeant la matrice hôte à CMK-3 qui a un petit diamètre de pore (4nm) semblable à MCM-41 a le potentiel pour modifier la nature du réseau à liaison en H, car TBA ne pouvait plus faire de liaison H interactions avec la paroi des pores. Cela rend intéressant d'étudier si le déplacement chimique de –OH montrent un comportement qui rappelle les mélanges volumique de TBA: TOL ou dévoilent certaines caractéristiques propres au confinement dans le CMK-3.

Une tentative de caractérisation de la dynamique d'auto-diffusion de TBA: TOL en confinement utilisant la méthode de RMN PFG a rencontré certains défis. Le carré moyen le déplacement des molécules de TOL confinées dans MCM-41 a largement dépassé la longueur de pore même. Les mouvements moléculaires en résultant étaient assez rapides même pour le minimum possible valeur de résolution temporelle Δ, telle que les molécules puissent voyager plusieurs fois sur le longueur de pore et faire apparaître la dynamique d'auto-diffusion Δ-independent. Toutefois, une mesure de la longueur des pores MCM-41 a été obtenue (0,65 μm) ce qui n'était pas possible à obtenir par microscopie électronique.

La diffusion de TOL dans les mélanges TBA: TOL confinés dans la SBA-15 a révélé l'existence de deux populations de dynamique différente, celle qui était deux ordres de grandeur plus rapide que la diffusion de TOL dans un mélange en volume de même composition et une seconde population avec une dynamique plus lente comparable à celle du volume qui s'est avéré être Δ - dépendant. Il est intéressant de noter que l'atténuation de l'aimantation a été jugée dépendante, une observation

caractéristique de la diffusion isotrope en volume, mais en même temps, aucun mélange strictment dépendent de la composition, contrairement de les mélanges volumique. Cependant, le forte de la magnétisation dans le cas de SBA-15 à des valeurs *q* beaucoup plus faibles, peut-être en raison du temps de relaxation transverse très court (T_2 ≈2 ms) des espèces confinées provoque une perte rapide de corrélation entre les spins nucléaires, même pour le plus petit possible valeurs de Δ, ce qui rend difficile de confirmer si la décroissance de l'aimantation observée de les courbes représentent l'ensemble de l'information sur la dynamique d'autodiffusion.

Expériences gravimétriques de sorption de vapeur de mélange gazeux binaires de TBA et TOL dans les pores MCM-41 ont montré que l'influence des interactions de liaison-H entre TBA et silice s'étend même à l'interface gaz-solide, conduisant à une adsorption préférentielle de TBA. Avec l'aide d'un modèle BET-multi-composante , nous avons exprimé de manière semi-quantitative la simple différence d'interaction des deux molécules avec la surface de la silice en termes d'un paramètre thermodynamique donnant l'affinité énergétique de chaque molécule pour la surface de silice. Nous trouvons l'énergie d'interaction de TBA avec la surface de silice à deux ordres d'amplitude supérieure à TOL, ce qui conduit à une couverture monocouche TBA à 100% surface de pores avec aussi peu que 10% de TBA dans le gaz binaire. Ainsi MCM-41 agit comme une matériel surface sélectif pour TBA. Très intéressant, après la couverture de la surface des pores par une première monocouche de TBA, la surface perd complètement sa sélectivité et la couche suivante suit la composition de gaz binaire. La différence de nature des interactions entre les deuxièmes couches adsorbées, c'est-à-dire des interactions de liaison H entre TBA et surface de silice et l'interaction de Van der Waals dans la deuxième couche est suffisamment forte pour que les deux couches perdent corrélation les uns avec les autres. Lors de la condensation post-capillaire de remplissage complet des pores, nous constatons que la concentration de TBA intérieur pore augmente rapidement par rapport à son concentration dans le gaz binaire de jusqu'à x_{pore} TBA≈ 44%, au-delà de laquelle l'augmentation de la concentration TBA est plus doux. Considérant que la fraction volumique des pores occupés par une monocouche de TBA est d'environ 44%, la situation pourrait être rationalisée très bien une fois de plus par la cœur-gaine de sorte que, tant qu'il y ait une quantité suffisante de TBA pour avoir une monocouche de la surface des pores, une séparation de phase dans une gaine de TBA et un cœur riche en TOL dont la concentration pourrait être déterminée. L'application de cette modèle BET-multi-composante à l'adsorption dans CMK-3, qui est hydrophobe en nature, révélée une inversion dans la nature des interactions moléculaires telles que la monocouche avait une concentration plus élevée de TOL que sa concentration correspondante dans le gaz binaire, même si l'effet n'était pas aussi fort que celui observé pour l'affinité TBA / surface de silice. C'était reflétée dans la moindre différence entre les paramètres thermodynamiques de TBA et TOL respectivement avec la surface de carbone par rapport à la surface de la silice. Plus important nous avons pu démontrer ici qu'en ajustant la nature chimique de la surface des pores nous sommes capables de changer l'organisation du niveau moléculaire à l'échelle nanométrique en jouant simplement avec les interactions spécifiques que les liquides confinés font avec les pores-murs et entre eux.

Le modèle de cœur-gaine dans des conditions d'équilibre justifiées par le modèle thermodynamique ont suscité un intérêt pour l'étude de la question de savoir si ces effets sont également exposés dans des conditions hors d'équilibre, ce qui peut conduire à un écart dans la dynamique d'imbibition spontanée de ces liquides binaires du Lucas-Washburn dynamique, qui a, dans le passé, décrit avec succès l'écoulement de liquides simples dans des nanopores.

Etude gravimétrique de l'imbibition spontanée des mélanges TBA: TOL à Vycor, la mise en place de réseaux interconnectés de silice nano-poreuse a révélé que la dynamique de les liquides binaires pourraient être prédits bien par l'équation de Lucas-Washburn, en supposant que les liquides binaires

d'être homogène dans la nature ayant la densité, la tension de surface et la viscosité égale aux mélanges d'état en volume correspondants. Cela nous amène à conclure qu'en les effets de séparation de phase ne sont pas présentés.

Cependant, l'étude de la radiographie neutronique du même procédé a montré TBA: TOL mélanges à monter avec deux fronts, indiquant une séparation de phase. Le front montant au-dessus, a montré la dynamique caractéristique d'une quantité plus élevée de TOL que dans la composition de mélange d'origine, tandis que le front de fuite a été trouvé pour avoir la dynamique comme prédit de Lucas-Washburn pour la composition de mélange donnée. Remplacement de TOL par sa version deutérée TOL-d a provoqué la disparition du front riche en TOL pour la TBA de 50% en vol. mélange. Comme TOL-d est un diffuseur fort, la disparition du front riche en TOL renforce l'interprétation de séparation des phases. Cependant, la phase riche en TOL se révèle être beaucoup plus petite en largeur que celle qui obéit à la composition du mélange réservoir. Très intéressant cependant, nous trouvons le front de tête pour 50% mélange TBA pour montrer une dynamique similaire à celle de TOL pure, tandis que le front avant pour un mélange de TBA à 90% présentait une dynamique similaire à un mélange qui a une concentration en TOL plus élevée que dans le réservoir en volume (≈ 77%). Une telle dépendance à la concentration qui commence à partir de TOL pure et va à haute concentration de TBA soulève une question important, la séparation des phases ne commence-t-elle à se produire qu'après un certain seuil minimal concentration de TBA est croisée, ce qui pourrait alors être directement associé à des interactions de TBA avec la surface de silice. Pour y répondre, une étude systématique d'une large gamme de concentration est nécessaire pour analyser la dynamique des phases séparées avant et aussi d'utiliser différentes combinaisons isotopiques pour jouer avec le contraste de la hausse liquide, ce qui pourrait constituer une entreprise bénéfique pour l'avenir.

Actuellement, le phénomène de séparation des phases a été interprété comme un entre les différentes tensions de surface de TBA et de TOL, de sorte qu'au niveau des jonctions capillaires, un TOL-riche front en raison de sa plus grande tension superficielle momentanément se sépare et occupe un capillaire devant le mélange principal en raison de sa plus grande pression Young-Laplace. Puisque ce front s'élève aussi à la racine carrée du temps, nous pourrions conclure que cet effet est tout au long du processus d'imbibition, mais encore faible, car la dynamique de l'imbibition est encore régie par le front plus lent qui constitue de façon écrasante le liquide montant avant.

La technique de radiographie neutronique a été utilisée pour étudier si les interactions liaison-H entre la TBA et la surface de la silice était suffisamment dominante pour remplacer la TOL d'un Vycor échantillon complètement rempli de TOL. Un bloc de Vycor a été complètement rempli par TOL-D via le processus d'imbibition. Après remplissage complet, le réservoir de liquide a été remplacé par un réservoir de mélange 90:10 TBA-H: TOL-H tel que seul le fond du bloc était en contact avec le liquide surface. Dans un trajet d'environ 21 heures, on constate une diminution progressive de la transmission de l'échantillon dans une certaine mesure, au-delà de laquelle le contraste final est resté stable. L'image du bloc Vycor complètement rempli de TOL-D ainsi que les images successives du bloc en contact avec le mélange HH (TBA-H: TOL-H) 90:10 a été normalisé par l'image du bloc vide de Vycor. Le profil de transmission de radiographie neutronique des changements dans le contraste du liquide rempli à l'intérieur du bloc Vycor après 21 heures indique que TOL-D a été remplacé à l'intérieur du bloc par TBA-H. Pour un mouvement diffusif de TBA on peut s'attendre à un front de plus faible transmittance progresser avec le temps. Cependant, nous observons une diminution homogène transmission de l'ensemble du bloc avec le temps même si le taux de diminution de la transmission est plus proche du bas du bloc ou en d'autres termes le début de la transmission profil. Une explication possible pourrait être la fuite dans le matériau couvrant les côtés du bloc de Vycor conduisant à la diffusion de TBA de tous les côtés. Cependant, si cela devait être vrai, la dynamique de ce processus aurait dû être beaucoup

plus rapide, ce qui n'est évidemment pas le cas. Le remplacement de la TOL-D par la TBA-H est une situation complexe impliquant une l'entrée de molécules TBA pendant la sortie de TOL et l'ensemble du processus affinité entre la surface de la silice et les molécules de TBA par rapport à la TOL. Un modèle qui pourrait expliquer ce phénomène de diffusion provoqué par la concurrence les interactions liquide-liquide et liquide-paroi pourrait constituer un autre avenir.